



This is to certify that the
dissertation entitled

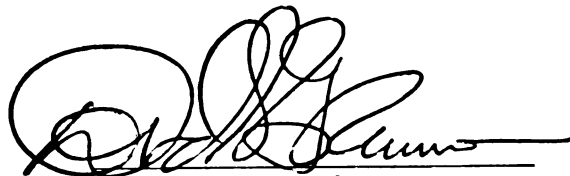
**Modification of Mechanical Properties of Sapphire
Fibers by Energetic Ion Implantation**

presented by

Heyun Yin

has been accepted towards fulfillment
of the requirements for

Ph.D. degree in Materials Science


Major professor

Date 7/15/97

**MODIFICATION OF MECHANICAL PROPERTIES OF SAPPHIRE FIBERS BY
ENERGETIC ION IMPLANTATION**

By

HEYUN YIN

A DISSERTATION

**Submitted to
Michigan State University
in partial fulfillment of the requirements
for the degree of**

DOCTOR OF PHILOSOPHY

Department of Materials Science and Mechanics

1997

ABSTRACT

MODIFICATION OF MECHANICAL PROPERTIES OF SAPPHIRE FIBERS BY ENERGETIC ION IMPLANTATION

By

Heyun Yin

Effects of 175 keV ion implantation into single crystal sapphire fibers have been studied, which include bend strength variation, modification of abrasion resistance, indentation fracture toughness, and sub-surface microstructure alteration. Behavior of implanted sapphire fibers in NiAl composite matrices was also investigated.

By means of three point bend tests, Weibull characteristic bend strength measurements showed that implantation of Mg^+ and Ar^+ has modest effects on the bend strength of unabraded fibers for doses ranging from 1×10^{16} to 2×10^{17} ions cm^{-2} . However, the abrasion resistance of implanted sapphire fibers can be increased significantly such that over 90 percent of bend strength can be retained after abrasion, whereas the same abrasion process causes 50 percent strength loss for unimplanted fibers. The measured surface compressive stress on implanted fibers using microindentation technique was approximately 2 GPa. The existence of the compressive stress is found to be closely related to the observed abrasion resistance increase. TEM observation indicates that the sub-surface microstructure resulting from ion irradiation was heavily damaged but still crystalline, and no amorphization was observed. The fabrication process for production of NiAl/ Al_2O_3 composites leads to severe strength deterioration in both unimplanted and implanted fibers.

The relationships between bend strength, surface flaws, abrasion processes, surface stress distributions, and indentation fracture mechanics are discussed.

Copyright by
Heyun Yin
1997

ACKNOWLEDGMENTS

This project was supported by the U. S. Department of Energy under grant #DE-FG0285ER45205, by the Composite Materials and Structure Center, Michigan State University, and by Ford Motor Company.

I would like to express my sincerest appreciation and gratitude to Professor D. S. Grummon, my major advisor, for his encouragement, guidance and immeasurable support throughout my study at Michigan State University.

I would like to extend my appreciation to the Ford Motor for provision of the Varian 350-D ion implantation machine, to Dr. R. Noebe at NASA Lewis Research Center, Cleveland, OH, for provision of NiAl alloy, and to Dr. J. Lucas for his assistance with nano-indentation experiments at Sandia National Laboratory.

I want to extend grateful acknowledgment to my advisory committee Dr. T. Bieler, Dr. M. Crimp, Dr. D. Grummon, Dr. W. McHarris and Dr. H. Schock for their guidance.

Also, I want to give my thanks to my colleagues and friends for their great help.

A special tribute is owed to my wife, Rong, for being so understanding and supportive throughout my study.

TABLE OF CONTENTS

Table of Contents	v
List of Tables.....	vii
List of Figures.....	viii
I. Introduction.....	1
II. Review of Literature	5
2.1 Physical and Mechanical Properties of α -Alumina.....	5
2.1.1 Crystal Structure.....	6
2.1.2 Intrinsic Disorder Mechanisms and Diffusion	9
2.1.3 Mechanical Properties.....	10
2.2 Continuous Sapphire Fiber Reinforced NiAl Composites.....	14
2.3 Strength Degradation of Sapphire Fibers due to Surface Damage.....	17
2.4 Ion Implantation Process	18
2.4.1 The Cascade Model	19
2.4.2 Radiation Damage in Solids.....	24
2.4.3 Radiation Effects	30
2.4.3.1 Rapid Quenching Effects	31
2.4.3.2 Radiation Enhanced Diffusion	31
2.4.3.3 Precipitation Effects.....	32
2.4.3.4 Residual Stress Induced by Ion Implantation	33
2.4.3.4.1 Ion Implantation-Induced Stress State	34
2.4.3.4.2 Surface Stress Model	35
2.4.3.4.3 Experimental Determination of Surface Stress....	38
2.4.3.5 Radiation Hardening and Softening Effects.....	39
2.5 Modification of Hardness, Toughness and Wear Resistance of Sapphire by Ion Implantation	42
2.6 Post-Implantation Heat Treatment.....	44
2.7 Summary of Literature Review	45
III. Experimental Procedures.....	47
3.1 Materials.....	47
3.2 Ion Implantation Process	48
3.2.1 Ion Beam generation	48
3.2.2 Target Set Up and Affecting Factors	54
3.3 Abrasion Procedure	59
3.4 Three Point Bend Tests.....	61
3.5 Indentation Fracture Toughness Tests	64
3.6 Post-implantation Annealing	67
3.7 Fabrication of NiAl/ Al_2O_3 Composite diffusion Bonding	67
3.8 Preparation of TEM Samples	72
3.9 Electron Channeling Pattern (ECP) and Atomic Force Microscopy (AFM)	73

3.10 Transport Calculation of The Range and Damage Profile	74
IV. Experimental Results and Analysis	78
4.1 Three Point Bend Strength without Abrasion.....	78
4.2 Effect of Abrasion on Bend Strength	85
4.3 Surface Residual Stress Determined by Micro-Indentation Fracture	93
4.4 Nano-Indentation Hardness.....	100
4.5 Annealing Effects.....	102
4.6 Sapphire Fiber Strength Degradation During NiAl Fabrication.....	110
4.7 Fiber Surface Morphology	117
4.8 Fracture Surface Morphology.....	125
4.9 TEM Investigation of Microstructure	131
4.9.1 TEM Observation	131
4.9.2 Channeling Effects	142
V. Discussion	143
5.1 Chemical versus Ballistic Effects.....	143
5.2 Residual Surface Stress and Bend Strength.....	147
5.3 Residual Surface Stress and Fracture Behavior.....	158
VI. Summary of Results and Conclusions.....	173
VII. Bibliography.....	177

List of Tables

	Page
Table 2.1 Comparison of Physical Properties of Several Materials Relevant to High Temperature Intermetallic Composites.....	15
Table 3.1 Properties of Sapphire Fiber.....	48
Table 3.2 Median Ranks	63
Table 4.1 Three Point Bend Strength of Sapphire Fiber with Different Doses..	80
Table 4.2 Effect of Abrasion on Bend Strength of Sapphire Fibers	88
Table 4.3 Micro-Indentation Crack Length at Different Dose	93
Table 4.4 Characteristic Bend Strength of Sapphire Fibers at Different Annealing Temperature.....	104
Table 4.5 Chemical Composition of β -NiAl.....	123
Table 5.1 Comparison of Tensile Stress in Near-Surface Zone.....	153

List of Figures

Figure 2.1	(a) Schematic of Stacking Sequence of Anion and Cation in Al_2O_3 Structure 7 (b) Crystal Structure of Al_2O_3 8
Figure 2.2	Schematic of Cascade Trajectories in Planar BeO Caused by 5-keV I^{127} Bombardment..... 21
Figure 2.3	The Number of Displaced Atoms in the Cascade as a Function of PKA Energy according to the Model of Kinchin and Pease 23
Figure 2.4	A Schematic Representation of The Variation in Size and Position of Implantation Induced Amorphous 27
Figure 2.5	Schematic Representation of The Principles of Implantation Induced Stress Model..... 36
Figure 2.6	The Variation of 25g Knoop Microhardness with Dose for Ti Implanted into Sapphire..... 40
Figure 2.7	Annealing Process of an Amorphous Material 46
Figure 3.1	Schematic Description of Varian 350 - D Ion Implanter..... 49
Figure 3.2	Schematic of Freeman Ion Source Structure..... 51
Figure 3.3	Mg and Ar Mass Spectrum Generated in 350D Implanter 53
Figure 3.4	Schematic of Rotating Fixture for Ion Implantation 55
Figure 3.5	Oscilloscope Display of Beam Current..... 56
Figure 3.6	Schematic of Abrasion Apparatus..... 60
Figure 3.7	Schematic Representation of the Crack geometry around a Vickers Indentation..... 65
Figure 3.8	Schematic of Cutting Tool for NiAl Diffusion Bond Assembly..... 69
Figure 3.9	Schematic of EDMed NiAl Diffusion Bond Plate..... 70
Figure 3.10	Schematic of NiAl/Sapphire Fiber Diffusion Bond Assembly 71
Figure 3.11	The Distribution of Mg^+ and Ar^+ Implanted into Sapphire Fiber At Different Energy, Calculated by TRIM (90.05)..... 70
Figure 4.1	Weibull Plot of Bend Strength for Mg^+ Implanted Sapphire without Abrasion 81
Figure 4.2	Weibull Plot of Bend Strength for Ar^+ Implanted Sapphire without

	Abrasion	82
Figure 4.3	Comparison of Bend Strength of Mg ⁺ and Ar ⁺ Implanted Sapphire Fibers without Abrasion	83
Figure 4.4	Effect of Cleaning Methods and Testing Environments on Bend Strength of Unimplanted Sapphire Fibers	84
Figure 4.5	SEM Observation on the Fracture Surface for Both Unimplanted and Implanted Sapphire Fiber.	86
Figure 4.6	Effect of Abrasion on Bend Strength of Sapphire Fibers	89
Figure 4.7	Weibull Plot of Bend Strength for Mg ⁺ Implanted Sapphire Fiber Abraded 20 and 60 minutes.....	90
Figure 4.8	Weibull Plot of Bend Strength for Ar ⁺ Implanted Sapphire Fiber Abraded 20 and 60 minutes.....	91
Figure 4.9	ESEM Images on the Surface Topography of Sapphire Fibers for Different Implantation and Abrasion Conditions.....	92
Figure 4.10	SEM Images of The Indentation Traces on Sapphire Fibers at Different Doses (load 100 grams).....	95
Figure 4.11	Variation of Integrated Surface with Doses of Mg ⁺ Implantation into Sapphire Fibers	96
Figure 4.12	Variation of Indentation Fracture Toughness with Doses.....	97
Figure 4.13	SEM Observation on the Trace of Lateral Crack Propagation	99
Figure 4.14	Comparison of Nano-indentation Hardness and Bend Strength of Sapphire Fibers	101
Figure 4.15	Effects of Annealing Temperature on the Bend Strength of Implanted Fibers.....	105
Figure 4.16	Weibull Plot of Bend Strength for Ar ⁺ Implanted Sapphire Fiber at Annealing Temperature of 1200 °C for 2 hours.....	106
Figure 4.17	Weibull Plot of Bend Strength for Mg ⁺ Implanted Sapphire Fiber at Annealing Temperature of 1200 °C for 2 hours.....	107
Figure 4.18	Weibull Plot of Comparison of Bend Strength for Mg ⁺ Implanted Sapphire Fiber Annealing 2 hours in Air Environment.....	108
Figure 4.19	Comparison of Bend Strength Weibull Plot for Unimplanted Sapphire Fibers and As-received Sapphire Fibers Etched From NiAl/Al ₂ O ₃ Composite	112
Figure 4.20	Comparison of Bend Strength Weibull Plot for Implanted Sapphire Fibers Etched from NiAl/Sapphire Fibers Composite.....	113

Figure 4.21	Fragmentation of Sapphire Fibers Etched From NiAl/Al ₂ O ₃ Composite	114
Figure 4.22	Effects of Different Processes on the Bend Strength Weibull Plots for Both Unimplanted and Mg Implanted Sapphire Fibers	115
Figure 4.23	SEM Observation on a Clean As-received Sapphire Fiber Surface ...	118
Figure 4.24	SEM Observation on the Surface of Sapphire Fiber Subjected to Chemical Etch Solution	119
Figure 4.25	SEM Observation on the Surface of Extracted Fibers from NiAl/Al ₂ O ₃ Composite	120
Figure 4.26	High Magnification SEM Observation on the Surface of Extracted Fibers From NiAl/Al ₂ O ₃ Composite.....	121
Figure 4.27	EDS Composition Analysis on the Residues in Extracted Fibers	122
Figure 4.28	SEM Observation of Ridge on the Surface of Etched Sapphire Fibers from NiAl/Al ₂ O ₃	124
Figure 4.29	SEM Observation on Fracture Surface Variation with Three Point Bend Strength.....	126
Figure 4.30	SEM Observation on Fracture Surface Feature of Sapphire Fiber Which Are Subjected to Three Point Bend Strength.....	127
Figure 4.31	SEM Observation on Fracture Surface Feature of Sapphire Fiber Which Fractured During Consolidation Process of NiAl/Al ₂ O ₃ Composite	129
Figure 4.32	SEM Observation on Internal Pores in Sapphire Fibers Which Fracture During Consolidation Process of NiAl/Al ₂ O ₃ Composite.....	130
Figure 4.33	SEM Observation on Internal Pore of Sapphire Fiber Which Fractured during Consolidation (Pore on Edge)	132
Figure 4.34	TEM Observation on 7 x 10 ¹⁶ Mg ⁺ cm ⁻² Implanted Sapphire Fiber at Room Temperature	135
Figure 4.35	TEM Observation on 2 x 10 ¹⁷ Mg ⁺ cm ⁻² Implanted Sapphire Fiber at Room Temperature	136
Figure 4.36	High Magnification TEM Observation on 2 x 10 ¹⁷ Mg ⁺ cm ⁻² Implanted Zone	137
Figure 4.37	TEM Observation on 1 x 10 ¹⁶ Ar ⁺ cm ⁻² Implanted Sapphire Fiber at Room Temperature	138
Figure 4.38	High Magnification TEM Observation on 1 x 10 ¹⁶ Ar ⁺ cm ⁻² Implanted Zone	139
Figure 4.39	Electron Channeling Pattern of Sapphire Fibers	141

Figure 5.1	The System of $\text{MgAl}_2\text{O}_4\text{-Al}_2\text{O}_3$	144
Figure 5.2	Schematic of V-notch Circular Surface Flaw on Sapphire Fiber and Theoretical Calculation of Strength Changes with Crack Length	148
Figure 5.3	Schematic of Implanted Zone and Stress Distribution.....	154
Figure 5.4	AFM Topography on Sapphire Fiber Surface.....	159
Figure 5.5	SEM Observation on the Interface between Sapphire Fiber and Abrasive Particles.....	160
Figure 5.6	AFM Image on Surface Profile and Surface Roughness Analysis on Abrasive Paper	161
Figure 5.7	Schematic of Radial and Lateral Cracks Evolution Under Point Indentation.....	162
Figure 5.8	Curvilinear Coordinate System for Boussinesq Axially Symmetric Point Load P.....	165
Figure 5.9	Principal Stress Contour at Head of Point Load	166
Figure 5.10	Stress Distribution Beneath Sharp Point Indentation	167
Figure 5.11	Stress Distribution during Indentation Process.....	169

CHAPTER I

INTRODUCTION

Alpha-aluminum oxide ($\alpha\text{-Al}_2\text{O}_3$), commonly called *alumina* in its polycrystalline form, or *sapphire* in its single crystal form, is an extremely stable metal oxide with a melting point of 2323 K. Desirable characteristics of single crystal sapphire fibers for reinforcing composite materials include high room temperature strength and high modulus. Sapphire fibers exhibit high strength and excellent creep resistance at temperatures as high as 1500°C [Tressler, 1992] and are thus an excellent candidate for use in metallic-, intermetallic-, or ceramic-matrix composites intended for use in the hot and corrosive environments found in projected aerospace, energy conversion and advanced transportation applications. The most comprehensive application of sapphire fibers, and where much work has been undertaken, is the use of sapphire fibers as reinforcement for $\beta\text{-NiAl}$ intermetallic matrices [Darolia, 1991; Shah, 1993; Bowman, 1995].

The main deficiency of sapphire fiber is its high sensitivity to surface flaws, or any surface damage caused by abrasion during fiber-fiber contact, hard particle impact, or cleaning procedures. Surface damage causes a dramatic reduction in strength, and thus may limit the potential of sapphire fibers as a reinforcement phase in advanced composite materials. In previous studies, sapphire fibers have been found to lose 30 percent of their ambient temperature tensile strength during handling and cleaning [Trumbauer, 1992], and 33 to 50 percent after fabrication by the power cloth technique [Draper, 1992].

Realistic fabrication protocols for composite components also place stringent demands on the bend strength of the fibers [Morscher, 1992], which is sensitive to pre-existing or process-induced surface flaws. In addition to abrasion during handling and lay-up, surface damage during processing also comes from surface chemical reactions with matrices and impurities, chemical reactions with binders, residual stresses resulting from

fiber-matrix coefficient expansion mismatch, and hot processing stress states [Draper, 1994; Bowman, 1995]. It is therefore of interest to develop methods to provide sapphire fibers with improved resistance to process-induced surface damage during high-temperature consolidation and service.

The realization that the surface plays a critical role in the mechanical properties of sapphire fibers has resulted in applications of several techniques by which sapphire fiber surfaces are treated. These include surface sizing [Trumbauer, 1992], surface glazing and quenching [Kirchner *et al.*, 1969], and impurity doping [Sayir, 1992].

Sizing involves organic coating on the fiber surface with materials such as E15-LV hydroxypropyl methylcellulose (Dow Methocel™). However, impurities (such as NaCl, Fe and sulfated ash) found in the sizing have the potential to degrade fiber strength during composite processing [Trumbauer, 1992].

Glazing and quenching by packing sapphire rods in chromium or calcium compounds, followed by firing at high temperature [Kirchner *et al.*, 1969] introduce compressive surface layers. The compressive stress results from a chemical reaction taking place at the surface and yielding products with greater volume. For instance, the volume increases 31% after the reaction: $\text{CaO} + 2 \text{Al}_2\text{O}_3 \Rightarrow \text{CaAl}_4\text{O}_7$. It is apparent that the sapphire surface is damaged by such reactions.

Impurity doping has been employed to improve the mechanical properties of alumina by a combination of solution and precipitate strengthening. Studies by Sayir *et al* [1992] showed that the bend strength of undoped laser heated float zone sapphire (LHFZ) fibers degraded with an increase in temperature at low and intermediate levels ($25 < T < 900^\circ\text{C}$), while Mg^{2+} , Ti^{4+} doped and $\text{Mg}^{2+} + \text{Ti}^{4+}$ co-doped sapphire did not show a strength degradation in the same temperature range. However, solubility of the aliovalent species is limited by the necessity to form charge-compensating point defects in the bulk, which may in turn adversely affect creep properties.

Ion implantation has been used to improve the surface properties of solid materials without altering their bulk properties. During the ion implantation process there is a physical modification of a shallow surface region, normally 0.3 to 0.4 μm thick. This area exists either as a metastable and strained crystalline system, as an amorphous phase, or as a surface layer in which fine precipitates exist as a result of implantation and/or subsequent heat treatment of the implanted material. Further, these highly defected structures may produce large residual stress states in the near-surface and sub-surface regions, as deep as $\sim 0.4 \mu\text{m}$. As will be shown, these stresses have interesting effects on strength and abrasion resistance of sapphire fibers. The possible effects of implantation-induced stresses in modifying surface behavior are potentially important and can involve changes in crack nucleation and crack growth behavior, as well as in plasticity mechanisms [Burnett, 1985; Hioki, 1986; Tressler, 1992]. The technique may thus be suited to the task of producing a useful near-surface modification of sapphire fibers without adversely changing their bulk properties.

In this study, Mg^+ and Ar^+ ion implantation was used to improve the surface properties of sapphire fibers. Modification of surface properties by ion implantation was characterized by measurement of the retention of three-point bend strength of fibers subjected to a controlled abrasion process, and by measurement of surface compressive stress, which is believed to effectively retard propagation of surface flaws during abrasion. Both implanted and unimplanted fibers were also consolidated in $\beta\text{-NiAl}$ matrices by a standard hot pressing process. Sapphire fibers extracted from the consolidated composites were then studied by measurement of residual bend strength, fiber fragmentation, and observation of surface and fracture surface morphology. Weibull statistical methods were used to establish the relationship between failure probability and characteristic strength. In addition, a theoretical calculation of the distribution and cascade damage accumulation from energetic ions implanted into sapphire was carried out using the well-known TRIM¹ ion

¹ TRIM stands for TRansport of Ions in Matter [Ziegler, 1985], detailed information about TRIM is given in Section 3.10, page 74.

transport code. The effects of compressive stress on the stress intensity factor at surface crack tips were also evaluated. Transmission electron microscopy microstructural studies of implanted sapphire fibers transverse sections were used to correlate the existence of a buried compressive stress zone with fracture behavior.

The following chapter presents a review of recent work on the basic properties of sapphire fibers, strength degradation of fibers caused by surface damage, and the use of ion implantation for modification of surface properties. Chapter III describes the experimental details and procedures. The results and discussion are presented in Chapter IV. Further discussion on the relationship between fracture mechanics and the abrasion process, and the relationship between fracture behavior and compressive stress induced by implantation is given in Chapter V. Finally, a summary of results and conclusions from the work are presented in Chapter VI.

CHAPTER II

REVIEW OF THE LITERATURE

As has been stated in Chapter I, sapphire fibers suffer from a pronounced dependency of strength on surface damage, which may occur during handling and composite processing. The issue of surface damage has attracted extensive research [Trumbauer, 1992; Draper, 1992; Sorensen, 1993; Shah, 1993; Asthana, 1995; Tewari, 1993; Bowman, 1995]. These investigations attempted to uncover possible mechanisms for surface damage and strength degradation, and proposed protective methods to shield sapphire fibers from surface damage. In this chapter, the literature on properties and behavior of single crystal sapphire fiber is reviewed, beginning with physical and mechanical properties of sapphire, followed by a discussion of the properties of continuous sapphire fiber reinforced NiAl intermetallic composites. Surface property modification by ion irradiation, as well as effects of irradiation, is reviewed in a subsequent section. Basic principles of ion implantation are also reviewed, and the principles of some measurements of mechanical properties are presented.

2.1 *Physical and Mechanical Properties of α -Alumina*

α -Alumina has useful properties including thermal expansion well matched to metal matrices, high heat capacity, good thermal shock resistance, desirable sintering behavior, and excellent mechanical properties. Therefore, it has widespread practical applications for structural components, insulating materials and other specialized systems in the optical, nuclear and electronic industries. In this section, a detailed review will be focused on its crystalline structure, disorder mechanisms and mechanical properties.

2.1.1 *Crystal Structure*

α -Alumina has a rhombohedral-hexagonal crystal structure with the space group $R\bar{3}C$, which can be described as having oxygen ions in a hexagonal closest packed arrangement with the aluminum ions occupying two thirds of the octahedral interstitial sites. As is conventional with rhombohedral solids, sapphire is usually described in terms of a hexagonal unit cell with Miller-Bravis indices. The lattice parameters of the structure are as follows: $a_0 = 5.12 \text{ \AA}$, $\alpha = 55^\circ 17'$, $n = 2$ (rhombohedral); or equivalently, $a_0 = 4.75 \text{ \AA}$, $c_0 = 12.97 \text{ \AA}$, $n = 6$ (hexagonal). Figure 2.1 schematically shows a schematic of the stacking sequence of anions and cations in the Al_2O_3 structure [Kronberg, 1957].

In the structure of α -alumina, large oxygen ions are stacked in the sequence A-B-A-B, thus forming a hexagonal closest packed array of anions. The cations are placed in the octahedral sites of this basic array and form another type of close packed planes which are inserted between the oxygen layers. To maintain charge neutrality, only two thirds of the octahedral sites available are filled with cations. Since the vacant octahedral sites also form a regular hexagonal array, three different types of cation layers can be detailed, depending on the position of the vacant cation site within the layer, namely a, b, and c, stacking in the sequence a-b-c-a-b-c. Therefore, the complete stacking sequence of anion and cation layer is A-a-B-b-A-c-B-a-A-b-B-c-A, repeating only after the sixth oxygen layer, or after the sequence a-b-c is repeated twice.

The structure of α -alumina results in coordination of 6 and 4 for the cation and the anion, respectively. The ionic radii for this coordination are 0.053 nm for Al^{3+} and 0.138 nm for O^{2-} [Dörre and Hübner, 1984].

In addition to α - Al_2O_3 , there are many other forms of alumina. One of them is γ - Al_2O_3 , which has a simple cubic crystalline structure.

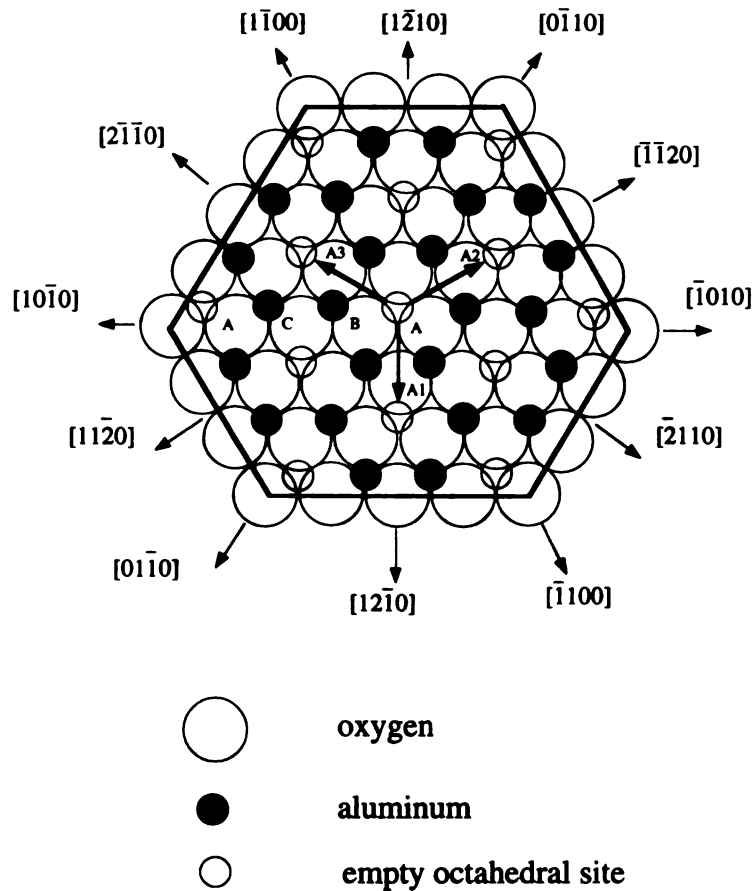


Figure 2.1 (a) Schematic of stacking sequence of anion and cation in Al_2O_3 structure. The large open circles are the oxygen ions, which form an hcp array; the small filled circles are the aluminum cations, which stack in an ABC sequence; and the small open circles are normally empty octahedral interstices. A_1 , A_2 , and A_3 are the smallest lattice vectors lying in the basal plane. (After Kronberg: 1957)

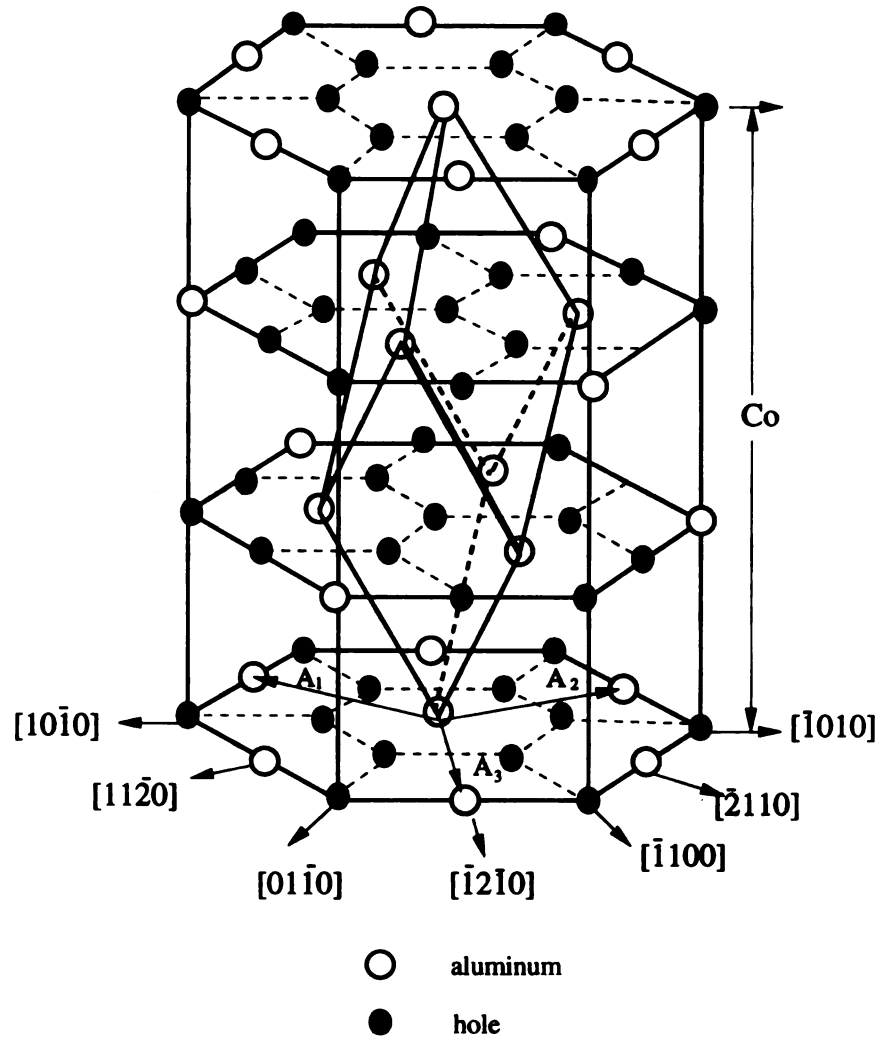
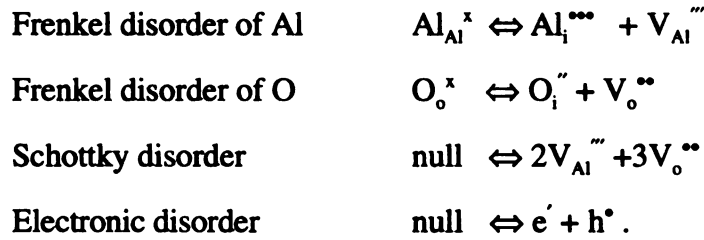


Figure 2.1 (b) Distribution of aluminum ions and holes on the hexagonal unitcell. The smallest rhombohedral cell describes the position of the cations in $\alpha\text{-Al}_2\text{O}_3$.

2.1.2 Intrinsic Disorder Mechanisms and Diffusion

Before reviewing the defects in Al_2O_3 , let us introduce Kröger-Vink notation. In this notation, positive and negative effective charges are marked by the superscript “ \bullet ” and “ $'$ ”, respectively. For the indication of effective charge neutrality the symbol “ \times ” is used. The position of the ion is given by subscript which denotes the regular lattice sites of the anion or cation by their respective symbols, or an interstitial site by the symbol “ i ”. Thus $\text{Al}_i^{\times\times\times}$ is an interstitial Al ion, O_o^{\times} represents an oxygen ion in its regular lattice site.

Dörre and Hübner [1984] summarized the possible disorder mechanisms in Al_2O_3 , namely:



Where e stands for an electron, h for a hole, and null means electronic neutrality.

These types of defects in the ionic α -alumina crystal are important because they are related to intrinsic or extrinsic diffusion mechanisms in α -alumina, where diffusion controls the properties of the material at elevated temperature.

Intrinsic diffusion means that the point defects through which the atomic mobility is accomplished are created exclusively by temperature. Atomic disorder of the crystal is caused only by thermal entropy. The equilibrium constants of defect formation and the formation energies indicate that intrinsic defect concentrations are very small [Kingery, 1976]. Typical high-temperature intrinsic defect concentrations in α -alumina are in the range 10^{-9} or lower, and the concentration of Schottky defects in α -alumina near the melting point is of the order 10^{-12} . That means that in α -alumina, intrinsic defects should not be important, even close to the melting point, because the defect number is smaller by several orders of magnitude than the number of native defects formed to compensate for aliovalent impurities [Dörre and Hübner, 1984]. Many investigations have been done on

the relation of intrinsic diffusion and electrical conductivity, optical absorption, sintering and creep [Yee and Kroger, 1973; Dutt and Kroger, 1975].

In contrast to sluggish intrinsic diffusion where intrinsic point defect concentrations are very small in Al_2O_3 , extrinsic diffusion arising from aliovalent impurities or dopants strongly affect the diffusion-controlled properties in Al_2O_3 because they greatly increase the defect concentration. For instance, Mg is thought to occur in Al_2O_3 as Mg_{Al}' . The neutrality condition is given by $[\text{Mg}_{\text{Al}}'] = 3 [\text{Al}_i^{\bullet\bullet\bullet}]$ for Frenkel disorder of Al to be dominant, and $[\text{Mg}_{\text{Al}}'] = 2 [\text{V}_o^{\bullet\bullet}]$ for Schottky disorder to be dominant. Therefore, for even a very small dopant content, in the ppm range, the concentration of native defects that results from the requirement of charge balance is much greater than the number of defects formed by the intrinsic disorder mechanism. If Frenkel disorder dominates, the coefficient of Al self-diffusion can be written as:

$$D_{\text{Al}} \propto [\text{Al}_i^{\bullet\bullet\bullet}] \exp(-\Delta H/RT)$$

where $[\text{Al}_i^{\bullet\bullet\bullet}] = 1/3[\text{Mg}_{\text{Al}}']$ which is the order of 10^{-6} , greater than the intrinsic disorder concentration of 10^{-9} .

In summary, defect formation and mobility are important to $\alpha\text{-Al}_2\text{O}_3$. Small amounts of impurities may control the concentration of the diffusing defects and lead to dissolution or precipitation process, which is directly related to the properties of $\alpha\text{-Al}_2\text{O}_3$.

2.1.3 Mechanical Properties

α -Alumina stands out as a useful engineering structural ceramic due to high hardness, high wear resistance, low friction coefficient, high resistance to corrosion by practically all chemical reagents, a very high resistance to hot corrosion in air, and high thermal stability. Meanwhile, it has well known drawbacks, i.e., its low strength as compared with the theoretical strength, the large statistical spread of its strength values, its great brittleness, its low toughness, and large susceptibility to thermal and mechanical shock loading.

Single crystal α -alumina (or sapphire) has very high elastic properties. For instance, Young's modulus is 461 GPa parallel to the c-axis, and 335 GPa perpendicular to the c-axis [Watchman, 1960]. Its tensile strength is 2.1 to 3.4 GPa at room temperature (parallel to c-axis), and its flexural strength is 1035 MPa parallel to the c-axis and 760 MPa perpendicular to the c-axis. Knoop hardness values of 1900 parallel to the c-axis, and 2200 perpendicular to the c-axis are reported by the manufacturer [Saphikon, 1992].

The fracture energy of single crystal α -alumina also shows anisotropy. Wiederhorn [1969] found preferential cleavage on the $\{10\bar{1}0\}$ and $\{\bar{1}012\}$ planes, where the fracture energy values are 7.3 J/m^2 and 6.0 J/m^2 at room temperature, respectively. The fracture toughness is $2.47 \text{ MPa}\sqrt{\text{m}}$.

The crystallographic anisotropy of sapphire is also illustrated by its plastic deformation at elevated temperature. There are three known slip systems in sapphire: $(0001)1/3\langle 11\bar{2}0 \rangle$ basal slip, $\{1\bar{1}00\}\langle 1\bar{1}01 \rangle$ prism slip, and $\{01\bar{1}1\}1/3\langle 0\bar{1}12 \rangle$ (or possibly $\{0\bar{1}12\}1/3\langle 01\bar{1}1 \rangle$ or $\{1\bar{1}23\}1/3\langle 01\bar{1}1 \rangle$) pyramidal slip [Lagerlöf, 1984]. For c-axis sapphire in tension, four different fracture mechanisms dominate at different temperature ranges [Jones, 1990]: 25-900°C, 900-1600°C and 1600-2000°C. The tensile strength of c-axis sapphire decreases from 3.8 GPa at room temperature to 1.4 GPa at 600°C in the lowest temperature region. It is believed that the mechanisms of brittle failure and stress corrosion failure are responsible for the strength degradation [Wiederhorn, 1978]. The second temperature region starts around 900°C and extends to the onset of macroscopic plastic deformation at 1600°C. In this range, tensile strength rises back to 2 GPa at 900°C, then decreases with further temperature increase. At 2000°C, tensile strength is only 0.5 GPa. Slow crack growth and plastic deformation are major mechanisms for the tensile deformation in these two temperature regions.

Sapphire is brittle at low temperatures and therefore the strength of sapphire at room temperature is highly flaw dependent. According to Griffith theory, a brittle material contains small flaws which act as stress concentrators when an external stress is applied.

Due to the absence of plastic deformation, stresses cannot be relaxed by local plasticity, and the local stress in the vicinity of the most severe flaw may reach the theoretical strength of the material, causing failure. The relation between strength and crack length can be described by $\sigma = 1/Y(2\gamma E/C)^{1/2}$, where σ is the strength, γ is the fracture energy, E is Young's modulus, C is the flaw size, and Y is a geometrical factor.

Dörre and Hübner [1984] summarized the types of flaws which have been observed in single crystal α -alumina. They are (1) intrinsic flaws, including pores, impurity particles, dislocation-nucleated flaws, and twin-nucleated flaws; and (2) extrinsic flaws, including edge flaws due to large pores, stepped flaws due to pore groups, and regular machining-induced flaws.

Residual pores come from shrinkage voids inherent in the single crystal α -alumina fiber growth process where voids form by entrapment of liquids behind the solid surface, or from incomplete sintering in polycrystalline alumina. Fracture-initiating pores are usually located underneath the surface and must have a sufficient size to act as fracture origins because they must compete with other strength-controlling defects such as surface defects induced by machining. Pore groups beneath the surface can act as fracture origins. Upon application of a load, individual pores of the group can link together to produce a large flaw [Evans and Toppin, 1972].

Dislocation-nucleated flaws are associated with dislocation slip systems. At high temperature, basal slip systems, prism slip systems, or pyramid slip systems can be activated during loading. The pile-up or interaction of generated dislocations can serve as a stress concentrator, assisting crack extension. Pollack and Hurley [1973] observed the strain rate dependence of the strength of sapphire whiskers and attributed the failure to the Orowan mechanism of crack extension.

Mechanical twinning can also cause failure of α -alumina. Twins on both basal and rhombohedral planes have been found. For instance, the basal twinning system, i.e., $(0001)\langle 1\bar{1}00 \rangle$ has been described by Kronberg [1957], whereas the rhombohedral

twinning system is $\{10\bar{1}1\}<10\bar{1}\bar{2}>$ [Heuer, 1966]. Preferential cracking along a twin-crystal band was observed by Stoel and Conrad [1963]. In the bending fracture of single crystal α -alumina, Heuer [1966] found the presence of deformation twinning. As compared to plastic deformation by dislocation glide, twinning is favored by low temperature and high strain rate. Twinning is a very important feature in the mechanical behavior of alumina because it occurs during most types of mechanical loading.

The possibility of plastic deformation during room temperature indentation and abrasion of sapphire has been verified by several researchers [Hockey, 1971; Stijn, 1961; Becher, 1975; Duwell, 1962]. The occurrence of plastic deformation in this normally brittle material is considered to be a consequence of the nature and magnitude of the local stresses developed under a pointed indenter or an irregularly shaped abrasive particle. It has also been observed that high dislocation densities can be produced in the near-surface region by mechanical polishing with a fine diamond abrasive compound, and that plastic deformation by both slip and twinning occurs during microhardness indentation at room temperature. Thus, deformation during abrasive surface finishing can influence the subsequent mechanical behavior by introducing a variety of surface damage artifacts.

Plastic deformation properties also control the abrasive wear behavior of sapphire. Abrasive wear is the result of a mechanical machining operation such as sawing, grinding, lapping, and polishing. It may also occur during solid particle indentation. Abrasive particles are small and irregular in shape so that a sharp corner of the particle is usually in contact with the substrate. This small area produces a high localized stress concentration, and the particles penetrate the surface. Moving the particle along the surface generates a long plastic groove and a complex crack pattern. During the abrasion process, the material removal involves plastic flow and cracking. The lateral cracking mechanism accounts for the occurrence of plastic deformation and fracture [Lawn, 1975, 1980, 1984].

It can be concluded that mechanical properties of α -alumina vary with crystalline orientation, surface flaws, temperatures and environments.

2.2 *Continuous Sapphire Fiber Reinforced NiAl Composites*

The intermetallic NiAl compound offers new opportunities for developing low-density, high strength structural alloys which might be used at temperatures higher than currently possible with conventional titanium and nickel-base alloys. β -phase NiAl (50 at% Ni, 50 at% Al) has four key advantages [Darolia, 1991]: its density of 5.95 g/cm³ is approximately two-thirds the density of nickel-base superalloys; its thermal conductivity is four to eight times that of nickel-base superalloys; it has excellent oxidation resistance; and its simple ordered bcc (B2-CsCl) crystal structure makes plastic deformation potentially easier compared to other intermetallic compounds.

However, the widespread use of NiAl as a high temperature structural material has been limited because of its poor room temperature ductility and toughness, and its poor high temperature strength. The ductility is highly dependent on aluminum content, grain size, impurity content and texture, and the ductility increases with temperature. It has been found [Darolia, 1991] that the tensile ductility of polycrystalline NiAl at room temperature is about 0 ~ 2%, but rises to about 6% for $\langle 110 \rangle$ single crystal NiAl containing 0.1% Hf. For single crystal NiAl, the plastic deformation behavior is highly anisotropic.

The fracture toughness of binary NiAl is also highly anisotropic. For example, a typical value of about $8 \text{ MPa}\sqrt{\text{m}}$ at ambient temperature is obtained from a sample oriented in the $\langle 100 \rangle$ direction while $4 \text{ MPa}\sqrt{\text{m}}$ was found for the $\langle 110 \rangle$ direction [Darolia, 1991]. Like ductility, the fracture toughness increases with temperature due to increased plasticity at the tips of the growing cracks.

The yield strength of NiAl drops rapidly with increasing temperature. The tensile strength of single crystal NiAl oriented in $\langle 100 \rangle$, for example, decreases from 880 MPa at room temperature to 200 MPa at 1600°C [Darolia, 1991]. It is obvious that the high temperature strength of unalloyed NiAl requires improvement to be competitive with the superalloys. There are six ways by which the strength of NiAl can be improved: elimination of grain boundaries, solid-solution strengthening, metallic precipitate

strengthening, intermetallic-precipitate strengthening, dispersion strengthening, and composite strengthening.

The use of sapphire fibers as a reinforcement in the NiAl is well known to improve its high-temperature strength [Shah, 1993; Bowman, 1995]. While a relatively weak fiber-matrix bond is desirable in brittle matrix composites from the fracture toughness perspective, a strong bond is a prerequisite for high-temperature strengthening, where the fibers are the load-bearing constituents. In the case of NiAl, rather than improving the room temperature bond, the use of sapphire fiber as a reinforcement material has been recommended to improve its high-temperature strength with a strong fiber-matrix bond [Asthana, 1995].

The reason that sapphire fiber was chosen as one of the most compatible reinforcement candidates in NiAl composite is that it is chemically stable in almost all the intermetallic compounds, with well matched coefficients of thermal expansion, and also because of its commercial availability. For example, the coefficient of thermal expansion of sapphire fiber is $9.1 \times 10^{-6}/\text{C}$ at 1400°C , much closer to $16 \times 10^{-6}/\text{C}$ of NiAl than either SiC ($5.5 \times 10^{-6}/\text{C}$) or Si_3N_4 ($3.7 \times 10^{-6}/\text{C}$). Table 2.1 lists a comparison of the physical properties of several reinforcement candidate materials [Shah, 1993].

Table 2.1. Comparison of Physical Properties of Several Reinforcement Candidates Materials in NiAl Intermetallic Composites

Materials	Density (g/cm ³)	T _m (°C)	Modulus (GPa)	CTE (10 ⁻⁶ /C)	Temperature °C
NiAl	5.96	1638	177	16.0	1000
Al ₂ O ₃	4.0	2050	524	9.1	1400
SiC	3.2	2600	690	5.5	1500
Si ₃ N ₄	3.18	1899	379	3.7	1500

Bowman [1993, 1995] has shown that the fracture strength of NiAl/sapphire fiber composite (30 volume percent) is 288 MPa at 300K, compared with 120 MPa for monolithic NiAl at room temperature; the fracture strength of NiAl/sapphire fiber composite still remains at 102 MPa at 1200 K, compared with 70 MPa for monolithic NiAl. Kumar [1992] reported that the fracture toughness increases to $9 \text{ MPa}\sqrt{\text{m}}$ for NiAl containing 15 vol% sapphire whiskers from $6 \text{ MPa}\sqrt{\text{m}}$ for monolithic NiAl, based on studies using chevron-notched short rod specimens. Kumar further found that a volume ratio of sapphire whiskers below 7.5% has no effect on fracture toughness.

Recently, Shah [1993] used DuPont's FP[®] alumina fibers (which are polycrystalline) as reinforcement in NiAl composite (approximately 35 volume percent). The results showed that the yield strength of aligned FP[®] alumina fiber reinforcement NiAl composite increased from 3.44 MPa for monolithic NiAl to 56.63 MPa at 1473 K. In contrast to NiAl/aligned FP[®] alumina fiber composite, the chopped FP[®] alumina fiber reinforcement NiAl behavior showed very poor consolidation, and the yield strength at 1473 K was only 3.90 MPa. Also, NiAl/aligned FP[®] alumina fiber composite has better creep resistance than monolithic NiAl or NiAl/chopped FP[®] alumina fiber composite. These results indicate that aligned fibers improved the high temperature strength and creep resistance significantly, and that aligned fiber composites are more easily fabricated.

However, several issues concerning the use of sapphire fiber as reinforcement in NiAl are still under study. The first concerns the interfacial reactions with the matrix. Recent research [Bowman, 1994; Draper, 1990, 1994] has shown that interfacial reactions degrade fiber strength, thus limiting the potential of the composite in load-bearing applications. The properties of NiAl/sapphire fiber composites fall below expectation by the rule-of-mixtures. One current approach to this problem is to employ coatings which are thermochemically stable to prevent reaction between fiber and the matrix; this preserves the physical properties and control the debonding and sliding stress, ensuring composite strength [Schalek, 1995]. The second issue concerns bend curvature that the fibers can

withstand as a function of time and temperature. Fragmentation of extracted fibers from NiAl/Al₂O₃ composites [Draper, 1992; Bowman, 1993] indicated that the fiber fracture must occur either during hot pressing fabrication process of NiAl/Al₂O₃ composite or during cooling from consolidation temperatures, in which thermal stress due to mismatched CTE might cause damage to the fibers. This requires fibers to tolerate small bend radii so that they will fracture at relatively high bend strain with respect to the room temperature failure bend strain [Morscher, 1992].

The main drawback of sapphire fibers as a reinforcement is due to its inherently brittle nature. Sapphire fibers thus exhibit very high sensitivity to surface flaws, which limits the fiber strength. The following section will summarize current knowledge regarding sapphire fiber strength degradation due to surface damage.

2.3 *Strength Degradation of Sapphire Fibers due to Surface Damage*

It has been well documented that sapphire fibers are highly susceptible to damage by abrasion during fiber-fiber contact, hard particle impact, and cleaning procedures. Draper [1992] observed the presence of particles adhered to sapphire fibers etched from a Fe-Al matrix. These fibers failed predominately at locations near the attached particles during tensile tests. Trumbauer [1992, 1994] identified four types of flaw population which significantly affect sapphire fiber strength: type A are the surface flaws attributed to handling and abrasion damage; type B are volume or internal flaws attributed to shrinkage voids which form during the manufacturing process; type C are localized fiber surface reaction flaws introduced during the flame-cleaning procedure, and type D are self-abrasion surface flaws introduced on unsized fibers. Furthermore, he found that flame-cleaning to remove the sizing applied by the manufacturer of Saphikon fiber produced a significant loss in strength, though it was apparent that other cleaning methods, such as the RCA¹ process, were much less destructive. He also found that self-abrasion treatments performed on

¹ RCA process is based on a two-step oxidizing and complexing treatment with hydrogen peroxide solution which act to remove organic surface films, alkali ions, and some other metallic ions.

unsized fibers produced a significant (30%) strength degradation, and further concluded that procuring unsized fibers increased the probability that self-abrasion damage would occur during shipping and handling. In addition to abrasion during handling and lay-up, mechanisms of fiber damage during processing include chemical reaction with matrices and impurities, chemical reaction with binders, and residual stresses resulting from fiber-matrix coefficient expansion mismatch, as well as hot processing stress states. Trumbauer [1992] reported that the tensile strength of sapphire fibers could easily be reduced to less than 69 MPa by implementation of a coating process followed by a simulated MMC fabrication cycle, and Tressler [1992] further pointed out that the defects which caused failure of sapphire fibers embedded in composites would most likely be defects generated during the handling and manufacturing processes.

Bend tests on small diameter (40-85 μm) sapphire fibers [Morscher, 1992] revealed localized kinking associated with failure sites. This kinking was not present in the large diameter (150 μm) fibers, presumably because the high volume allows more subgrain formation and stress relaxation. However, high temperature three-point bend tests on individual fibers have shown the fiber surface to be the origin of failure for sapphire fibers of all sizes. Thus, surface flaws are probably the limiting factor on sapphire fiber bend strength.

So far, it has been stated that sapphire fibers have important applications in high temperature NiAl composites. Meanwhile, they also have a significant drawback, namely, high sensitivity to surface damages which cause severe strength degradation. The following section will document how ion implantation can overcome the disadvantage and improve mechanical properties of sapphire.

2.4 *Ion Implantation Process*

Ion implantation is a low-temperature vacuum surface treatment process involving ion-energies typically in the range of 50 to 500 keV. Energetic ions penetrate the surface of

the target (host) material and come to rest in an approximate Gaussian distribution. During the implantation process, the energetic ions collide with the substrate or target's atoms, transfer energy to the host atoms and then cause further cascades. The cascade effect finally results in a great physical or chemical change near the substrate surface (usually 0.3 to 0.4 μm deep) without altering the bulk material properties. In this section, ion implantation processes and applications are reviewed, beginning with general description of ion bombardment cascade model, followed by discussion of radiation damage and other related effects. Finally, a summary of the literature on modification of mechanical properties of sapphire by ion irradiation is presented.

2.4.1 *The Cascade Model*

When a bombarding particle strikes a solid target, the energy of the bombarding particle will be transferred to a stationary lattice atom by both nuclear collisions and by interaction with host atom electrons. Inelastic nuclear collisions result in the displacement of host atoms from their structure-sites. These displaced atoms may then proceed to displace other host atoms until the energies of both the incident ions and the recoiling host atoms are insufficient to produce further displacements. For most materials the energy needed to displace an atom from its structure is about 25 eV (which is so called displacement threshold energy). Thus for ions with a few hundred kilo electron volts energy, the number of host atom displacements per incident ion is expected to be large.

Electronic collision in which the incident ion interacts with electrons of host atoms can result in the weakening of the host-atom-bond by ionization and by the formation of charged defects such as color centers. Such processes are more efficient at higher ion energies, whereas displacements prevail at lower energies, with the competition between these processes producing the typically Gaussian damage and implant species concentration profiles. Theoretical models have been developed for predicting both the energy partitioning between the collisional and electronic energy loss processes, and the spatial

distribution of the resultant damage patterns. One of these models, known as TRIM-90 due to Ziegler [1985], has been used in this study. This Monte Carlo simulation calculates the penetration of ions into solids, the final distribution of the ions, and the kinetic phenomena associated with the ion's energy loss, target damage, ionization and phonon production.

The lattice atom first struck and displaced is called the primary knock-on atom or PKA. Because a PKA possesses kinetic energy transferred by incident ion, it becomes an energetic particle and is capable of creating additional lattice displacements. Subsequently displaced lattice atoms are known as higher-order knock-on, or recoil atoms. An atom is considered to have been displaced if it comes to rest sufficiently far from its original lattice site so that it cannot return spontaneously. It must also be outside the recombination region of other vacancies created in the process. The displaced atom ultimately appears in the lattice as a substitutional or an interstitial atom. The ensemble of point defects created by a single primary knock-on atom is known as a 'displacement cascade'. Figure 2.2 is the schematic of a cascade process due to impact by a single ion.

The simplest theory of the displacement cascade is that of Kinchin and Pease [1955]. Their analysis is based on the following definitions and assumptions:

1) Definition of parameters:

E is an energy possessed by the PKA, E_d is displacement threshold energy (25 eV for most materials); E_c is so-called cutoff energy (below which the moving atom cannot transfer enough energy to an electron of the medium to remove the electron from whatever bound state it may be in), and is related to interatomic potential; T is the transferred energy; P_d is displacement probability; and $\nu(E)$ is the number of displaced atoms produced by a single energetic incident ion.

2) The cascade is created by a sequence of two-body elastic collisions between atoms;

3) The displacement probability is given by

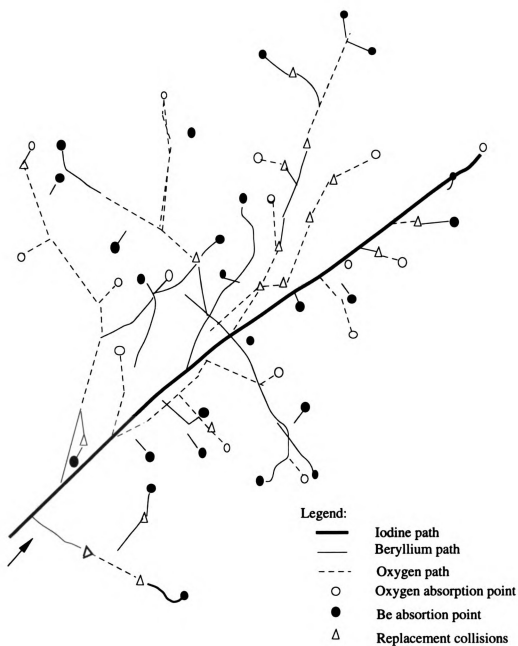


Figure 2.2 Schematic of cascade trajectories in planar BeO caused by 5-KeV I^{127} bombardment (after Carter, G., and Colligon, J. S., *Ion Bombardment of Solid*, 1968).

$$P_d = \begin{cases} 0 & (\text{for } T < E_d) \\ 1 & (\text{for } T > E_d) \end{cases} \quad (2.1)$$

- 4) The energy E_d consumed in displacing an atom is neglected in the energy balance of the binary collision that transfers kinetic energy to struck atoms;
- 5) For all energies less than E_c , electronic stopping is neglected, and only atomic collisions are considered;
- 6) The energy transfer cross section is given by a hard-sphere model;
- 7) The arrangement of the atoms in the solid is random, effects due to the crystal structure are neglected.

Under these assumptions, the number of displaced atoms $\nu(E)$ produced by incident ions can be deduced:

$$\nu(E) = \begin{cases} 0 & (\text{for } 0 < E < E_d) \\ 1 & (\text{for } E_d < E < 2E_d) \\ E / 2E_d & (\text{for } 2E_d < E < E_c) \\ E_c / 2E_d & (\text{for } E > E_c) \end{cases} \quad (2.2)$$

The following plot (Figure 2.3) illustrates the four regions predicted by the model, i.e. when the energy of an incident ion is less than the displacement energy E_d , the number of displaced atoms is zero; when the energy is between E_d and $2E_d$, the number is 1; when the energy is greater than $2E_d$, but lower than cut-off energy E_c , the number increases linearly with incident ion energy; Finally, if the energy exceeds the cut-off energy E_c , the number of displaced atoms reaches maximum value of $E_c / 2E_d$.

In summary of the cascade process, primary atom makes multiple collisions, either elastic or inelastic, with the lattice atoms before coming to a final resting position. Energy loss is transferred to the lattice in form of electronic excitation when there are inelastic contributions to the loss mechanism, or in kinetic energy of motion of the lattice atoms

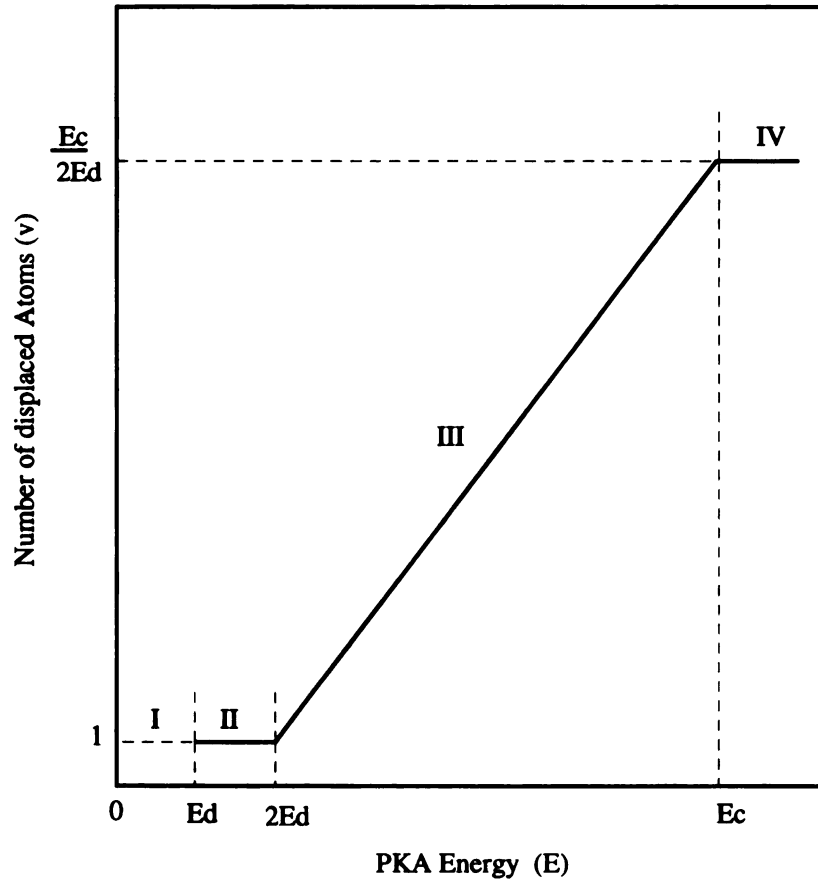


Figure 2.3 The number of displaced atoms in the cascade as a function of PKA energy according to the model of Kinchin and Pease (after Kinchin and Pease: *Rep. Prog. Phys.*, vol. 18, 1955).

when the collision is elastic. In former case, secondary electron emission and emission of electromagnetic waves is observed. In the latter case, the struck atoms are displaced from their equilibrium position in the lattice. If the received energy is sufficient and properly directed, the struck atoms influence the surrounding atoms immediately. A vacancy is created at the original atom position whilst the displaced atoms become foreign atoms elsewhere in the lattice.

2.4.2 Radiation Damage in Solids

As ion bombardment proceeds, it is anticipated that radiation causes atomic displacements and the production of defects in the target (or host material), which influence the material's properties. This is so-called radiation damage. Radiation damage is directly associated with ion energy, incident ion species, target material, and target temperature.

Ion energy determines the stopping power or specific energy loss, (dE/dx) . Here, E is the ion energy and x is the distance which is usually measured along the direction of incidence of the ions. The total specific energy loss is taken to be the sum of three separable components: nuclear, electronic and charge exchange

$$dE/dx = (dE/dx)_e + (dE/dx)_n + (dE/dx)_{ch} \quad (2.3)$$

At lower energy, nuclear stopping dominates and is responsible for most of the angular dispersion of an ion beam. At higher energy, electronic collisions are the more important and in slowing down to rest from these energies the bulk of the particles energy is dissipated in the form of electronic, rather than nuclear, motion. Provided a recoiling lattice atom receives an energy in excess of the displacement energy, E_d , it can leave its lattice site to become permanently displaced within the solid. In most cases of interest, lattice atoms recoil from primary collisions with kinetic energies far in excess of the displacement energy, and are capable of penetrating many atomic distances into the surrounding lattice.

The intensity of incident ions, irradiation time and irradiated area can be related together by so-called 'ion dose', as defined:

$$D = \frac{It}{Aqe} \quad (2.4)$$

where t is the implant time in seconds, I is the integrated beam current in Amperes, A is the effective scanned area in cm^2 , D is the dose level in ions/ cm^2 , e is electron charge (1.602×10^{-19} coulombs) and q is the ion charge state.

The choice of ion species affects the extent of radiation damage because of ion mass and chemical nature. It is understandable that heavy ions can transfer more energy to lattice atoms than lighter ones, and thus cause more collisions and more displaced lattice atoms. Chemical interaction between incident ions and lattice atoms affect the production of defects and microstructure. For instance, implantation of gaseous ions such as N or Ar into sapphire causes blistering within the implanted region [Hioki: 1989; McHargue: 1987].

For different classes of materials, their chemical bonding might range from ionic to covalent to metallic. The type of bond affects production of defects and atomic displacements during ion irradiation, and further influences the extent of irradiation damage. Generally, ion irradiation produces amorphous microstructures in ionic or covalent bond-type materials more easily than in metallic materials. Naguib and Kelly [1975] proposed a bond-type criterion to predict the amorphization for materials. They suggested that materials with Pauling ionicities less than 0.6 are more easily made amorphous by ion irradiation. At 300 K, the amorphization dose for α -SiC, for which the Pauling ionicity is 0.12 (covalent), is 10^{-3} of that required for α -Al₂O₃, whose Pauling ionicity is 0.63 (ionic bonding) [McHargue *et al*, 1986].

In order to estimate the magnitude of radiation damage, two characteristics of the damage must be specified, i.e., the nature and the number of defects. The following

paragraph will review the radiation damage induced during ion implantation process. First, defects produced by ion implantation include:

- (i) point defects (vacancies and interstitial);
- (ii) impurity atoms (atomically dispersed transmutation products);
- (iii) small vacancy clusters (depleted zone);
- (iv) dislocation loops;
- (v) dislocation lines; and
- (vi) cavities.

The formation of voids, dislocation loops and networks, for example, originates from point-defect aggregation. In their subsequent evolution, those extended defects serve as additional sinks for continuously generated point defects. Pedraza and Mansur [1986] pointed out that it is the generation of point defects and their evolution during irradiation which perturbs long-range order in crystalline host target. Take a Frenkel pair for example, which contains a vacancy and an interstitial. If an interstitial of the appropriate species is generated at or it attains by diffusional migration such a site, it will have a higher tendency of remaining in it if there is a nearby vacancy. The role of the vacancy in the trapping process is that of allowing for partial volume relaxation. The formation of the complex thus creates a center of short-range order. In this way, damage accumulation eventually may lead to the host material becoming amorphous.

The relationship between microstructure and irradiation damage accumulation was studied by Burnett and Page [1985]. According to their proposed model, three microstructural regions may arise from room temperature ion-implantation into crystalline materials (Figure 2.4). In region I, at low doses, a damaged but still crystalline solid solution is formed. In region II, at intermediate doses, amorphous material is initially formed at the peak of the displacement damage profile, resulting in a subsurface amorphous layer which thickens with increasing doses. In region III, at sufficiently high doses, a true surface amorphous layer is formed which also thickens with increasing dose.

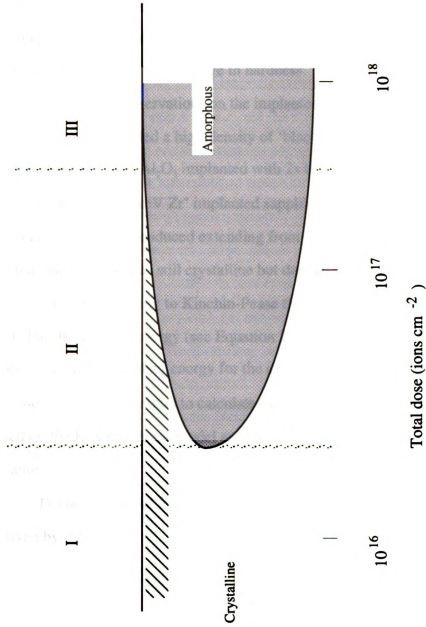


Figure 2.4 A schematic representation of the variation in size and position of implantation induced amorphous zone showing: I, a damaged crystalline region; II, a sub-surface amorphous zone; III, a surface amorphous layer. (After P. J. Burnett and T.F. Page, in *Deformation of Ceramic Materials*, ed R.B. Tressler and R.C. Bradt, 1984)

Microstructure alternation due to ion implantation can be characterized by mechanical property changes. Through the implantation of 300 keV Ti⁺, Cr⁺, Y⁺ and Zr⁺ into planar sapphire [Burnett and Page, 1985], it was found that while doses below that which are required for the onset of amorphization, implantation resulted in surface hardening; however, the Ti⁺ and Cr⁺ implanted specimens showed a less rapid decrease in hardness with increasing dose compared to the Y⁺ and Zr⁺ implanted sapphire. Compared to unimplanted sapphire, the results for the Ti⁺ and Cr⁺ which created a region II microstructure showed little change in hardness.

Direct TEM observations on the implanted region of sapphire [McHargue: 1986, 1987, 1991] also revealed a high density of 'black spots', which are typical of point-defect clusters that exist in α -Al₂O₃ implanted with 2×10^{16} Cr⁺/cm² (280 keV) at room temperature. For 300 keV Zr⁺ implanted sapphire at dose of 4×10^{16} ions/cm², a subsurface amorphous layer was produced extending from 40 nm to 100 nm from the free surface, whereas the material was still crystalline but damaged outside the implanted region.

Second, according to Kinchin-Pease theory, the number of atoms displaced is related to the incident energy (see Equation 2.2); i.e., the number of atoms displaced is proportional to the incident energy for the energy between E_d and E_e . Norgett *et al* [1975] proposed a modified method to calculate the number of displacements. This new method is based on the Kinchin-Pease model and the half-Nelson model, and is outlined by following equation:

1) The number of Frenkel pairs N_d generated by a PKA of initial kinetic energy E is given by:

$$N_d = k \hat{E} / 2E_d \quad (2.5)$$

where \hat{E} is the energy available to generate atomic displacement by elastic collisions.

2) The displacement efficiency k is given the value 0.8, independent of PKA energy, the target material, or its temperature.

3) The inelastic energy loss is calculated by the method of Lindhard, i.e.:

$$\begin{aligned}
 \hat{E} &= E/[1 + kg(\epsilon)] \\
 g(\epsilon) &= 3.4008\epsilon^{1/6} + 0.40244\epsilon^{3/4} + \epsilon \\
 k &= 0.1337Z_1^{1/6}(Z_1/A_1)^{1/2} \\
 \epsilon &= [A_2 E / (A_1 + A_2)] [a / Z_1 Z_2 e^2] \\
 a &= (9\pi^2 / 128)^{1/3} a_0 [Z_1^{2/3} + Z_2^{2/3}]^{-1/2}
 \end{aligned} \tag{2.6}$$

where a_0 is the Bohr radius, e the electronic charge, Z_1 and Z_2 are the atomic numbers of the projectile and target and A_1 and A_2 are the mass numbers of the two atoms.

It should be pointed out that at higher energies (a few keV), especially for low temperature implantation into covalent materials (such as semiconductors or insulators), the linear Kinchin-Pease theory cannot accurately predict the damage level. This inability has been attributed to the effects of energy spikes. Basically, when the nuclear energy loss per atomic plane is high, it is possible to conceive of a volume surrounding the ion track as either (a) a thermal spike, in which the average energy supplied to lattice atoms substantially exceeds the heat of melting, or (b) a displacement spike, in which an almost continuous network of displaced atoms is created. Thermal spikes can give rise to excess damage by a process in which the local hot spot surrounding the ion track extends out considerably beyond the original collision cascade dimensions. This superheated region may ultimately be quenched into an amorphous state in times of the order of 10^{-12} s to give considerably more damage than expected from collision theory. Alternatively, displacement spikes can give rise to excess damage by spontaneous collapse to an amorphous state, when the defect (or displacement) density attains a critical level.

Temperature affects the degree of damage and alters the nature of the observed damage structure. Two types of annealing that can take place during implantation; namely, (a) dynamic annealing of damage produced by single ions, and (b) thermal annealing of damaged material due to a general rise in target temperature during implantation. In type (a)

annealing, where damage increases with dose rate, it is believed that cascades can overlap before a single cascade damage has completely annealed. Type (b) annealing of the damaged layer can result from very high dose and high dose-rate implantation conditions, which produce a bulk temperature rise during implantation or it may occur if the target is deliberately heated. In such cases, an increase in dose rate (beam current density) can produce a reduction in apparent damage because of the high target temperature attained. The latter (bulk heating) effect can have several consequences for the generation of a disorder structure during the initial stages of implantation. It will be detailed in section 2.4.3.7.

When an incident ion enters a crystalline target surface, two additional phenomena which affect the extent of radiation damage may appear: focusing and channeling. Focusing refers to the transfer of energy and atoms by nearly head-on collision along a row of atoms. Channeling is the complementary process whereby atoms move over longer distance than normal in the solid, along open directions in the crystal structure, being kept in the channel by glancing collisions with the atomic wall. Focusing and channeling affect both the number and configuration of displaced atoms in a cascade. First, atoms moving along the crystallographic direction favorable to focusing or channeling lose energy only by glancing collisions with atoms ringing the axis of motion. The energy transfer in those collision is well below E_d . Second, the focused or channeled atoms are able to move much larger distances than ordinary knock-ons before coming to rest. As such, displaced atoms that have been created by focusing or channeling mechanisms contribute disproportionately to radiation effects, such as diffusion-enhanced creep and void growth, and can significantly extend the depth of the damage zone.

2.4.3 *Radiation Effects*

As has been stated, radiation damage originates from production of point defects. Interaction between atomic mobility and aggregation of point defects and dissipation of

ions' high energy along a cascade result in so-called radiation effects, including quenching effects, diffusion effects, stress effects, precipitate effects, as reviewed in following section.

2.4.3.1 *Rapid Quenching Effects*

The energy deposited in a collision cascade is dissipated through atomic motion in times of order of 10^{-12} s, presumably by lattice thermal conductivity. Typically a cascade volume can be expected to contain ≥ 1000 atoms [Appleton, 1984]. Some research reported from theoretical calculations that spike temperature in copper dropped from 2000°C to 500°C in 3×10^{-11} s [Dienes, 1957]. The high local "temperature" should cause some homogenization around the thermal spike, but the ultimate material interactions induced locally and at long range depend strongly on the particular material system. The quenching rate of a spike cascade can be estimated to be about 10^{13} K/s. Thus, a variety of new material properties can be expected from this extremely rapid quenching. The ultimate result, however, will depend on the defect interaction and annealing properties of the solid, as well as on the details of the cascade.

2.4.3.2 *Radiation Enhanced Diffusion*

In contrast to thermal diffusion, radiation enhanced diffusion is a diffusion effect which is activated by bombardment with high energy particles. This effect can be produced during self-implantation, or by irradiation with non-doping particles (α -particles, neutrons, protons). Under energetic ion bombardment, diffusion can be greatly enhanced because huge numbers of point defects, which mediate normal thermally activated diffusion, are produced. Ion bombardment not only creates large numbers of defects, which can accelerate substitutional, interstitial or vacancy diffusion mechanisms, but also establishes solute atom and point defect concentration gradients, which can act as strong driving forces in the mixing process. The effect of radiation-enhanced diffusion can be calculated

approximately by assuming that the diffusion coefficient is proportional to the vacancy concentration [Tsuchimoto, 1970]:

$$\frac{\partial N_v(x,t)}{\partial t} = D_v \frac{\partial^2 N_v(x,t)}{\partial x^2} - \frac{N_v(x,t)}{\tau_v} + g(x) \quad (2.7)$$

where $N_v(x,t)$ is the vacancy concentration, D_v is their diffusion coefficient, τ_v is the recombination lifetime of vacancy, and $g(x)$ is the generation rate. $g(x)$ may be estimated from the ion range, the straggling, the amount of energy released in the form of nuclear recoils and the displaced energy, i.e.:

$$g_o = \frac{j \left(\frac{dE}{dx} \right)_{n, mx}}{qE_d} \quad (2.8)$$

where g_o is the maximum generation rate, j is the current density, E_d the vacancy-formation energy, and $(dE/dx)_{n, max}$ the maximum energy deposited into atomic processes. The vacancy concentration $N_v(x)$ and diffusion coefficient could then be calculated as a function of depth. Some researchers have confirmed the phenomena of radiation-enhanced diffusion. According to Dearnaley [1973, for heavy ions having energies in the vicinity of 50 keV during typical implantation conditions, the irradiation enhanced diffusion coefficient has been estimated at $10^{-15} \text{ cm}^2 \text{ sec}^{-1}$. Such a diffusion coefficient is typically equivalent to a temperature of about 450°C in copper, 600°C in iron, 200°C in aluminum and about 1000°C in silicon with respect to vacancy controlled diffusion.

2.4.3.3 Precipitation Effects

Generally, as ion dose is increased, more and more atoms are introduced into the lattice and it is of considerable interest to determine whether or not the material so formed remains a solid solution indefinitely. In conventional alloying methods, when the

concentration of impurity exceeds the maximum solubility limit in the target material and the diffusion conditions are suitable, then precipitation of a second phase results. In a conventional system, precipitation effects can only be observed in a limited number of material systems because supersaturation occurs when there is a reduction in temperature of a solid solution. In case of ion implantation, there is, in principle, no such limitation since ions of any element can be injected into any solid irrespective of solubility considerations.

There are basically four processes that govern precipitation: (a) nucleation, which means that the small region of the second phase must overcome interface energies in order to form; (b) diffusion of atoms to the nuclei to supply additional material so that the second phase can grow; (c) a reaction occurs where the atoms at the interface rearrange themselves into the structure of the new phase; and (d) diffusion of excess atoms from the reaction away from the interface.

At low temperature where thermally activated diffusion of the implanted atoms is virtually absent, it might be concluded that the system so formed would in fact remain as a supersaturated solid solution. But, on the other hand, if the implantation temperature was sufficiently high that impurity diffusion became significant, agglomeration and precipitation might be expected. Therefore, post-implantation annealing usually is undertaken when it is desired to make precipitation take place.

Previous studies have shown the occurrence of epitaxial recrystallization of Cr, Mn, Ni and Xe implanted into sapphire during post-implantation thermal annealing since there is little or no solid solubility of such ion species in sapphire [Ohkubo, 1986]. For Mg-implanted sapphire, Mg has been found to segregate to the $(10\bar{1}1)$ prismatic free surface [Mukhopadhyay, 1988].

2.4.3.4 Residual Stress Induced by Ion Implantation

After ion implantation, the implanted solid surface is generally in a stressed state, either compressive or tensile, depending upon the depth. The existence of stress on the

solid surface greatly influences measured surface properties. The following section will deal with ion implantation induced stress states, proposed surface stress models, and experimental measurement of surface stress.

2.4.3.4.1 *Ion Implantation-Induced Stress States*

Generation of defects by displacement processes results in a volume change within the implanted layer. However, if this change is constrained by either underlying or surrounding material, large stresses may be generated in this relatively thin implanted layer. Both compressive and tensile stresses have been observed, depending upon the nature of the host material and ion species [EerNisse, 1971; Burnett, 1985].

Sapphire is known to undergo volume expansion when exposed to ion bombardment [Krefft, 1978]. Because the defect density varies with depth as a result of the ion stopping power of the target atoms, the generated stress is not uniform. Krefft, however, assumed that the stress was distributed uniformly along the expansion direction, and used the concept of integrated stress, S , to represent the stress generated by ion implantation, which is the integral over the entire ion damage range. Their results have shown that the integrated stress increased with doses up to 1×10^3 (N/m) for the sapphire plate which was implanted with Ar^+ at 500 keV. They also have shown that light ion implantation into sapphire which had been previously implanted with heavy ions may relieve the compressive stress resulting from Ar^+ implantation. Furthermore, they found higher absolute stress values to result from implantation along $[11\bar{2}0]$ and $[01\bar{1}0]$ which were caused by higher lattice expansion along $[0001]$. In other words, defect formation and corresponding lattice expansion occurred more rapidly during irradiation perpendicular to the c-axis.

Specht [1994] found that the density of Al_2O_3 in midrange decreases by 4% after Cr^+ implantation while the volume expansion in the midrange was only $\sim 0.2\%$. He attributed the density reduction of Al_2O_3 to high energy transfer collisions that knock Al

and O atoms deep into the crystal and give rise to excess vacancies and deep interstitial. Therefore, it is expected that the stress state in the midrange about 40 nm from free surface is tensile.

Using both cantilever bending and indentation fracture techniques, Burnett and Page [1985] found that the generation of near-surface compressive stresses in sapphire implanted with Y^+ and Ti^+ initially increased with ion dose until a critical dose (8×10^{16} ions cm^{-2}) was reached. Beyond this dose, stress relaxation was observed. The stress, averaging over $4\langle X_D \rangle^1$, can reach 6.4 GPa for 5.6×10^{16} Ti^+ cm^{-2} and 7.6 GPa for 1.7×10^{16} Y^+ cm^{-2} at 300 keV.

Hioki *et al* [1986] studied the effects of implantation temperature on the compressive stress. They showed that for implantation at 300 K, the integrated stress increases monotonically with doses up to 1×10^{16} Ni^+ (300 keV). At 100 K integrated stress increases rapidly with an increase in dose and reaches a maximum value at just below D_a (the amorphization dose is 5×10^{15} Ni/cm^2), followed by a marked decrease at higher dose. They also determined that the average compressive stress reaches a value of 9 GPa at 100 K and 2 GPa at 300 K. Therefore, ion implantation at a lower temperature is much more effective in generating a large surface compressive stress.

2.4.3.4.2 *Surface Stress Model*

As discussed in section 2.4.2, accumulation of irradiation damage leads to amorphization of crystalline target material when implantation exceeds a certain dose. Amorphization results in stress relief. After amorphization, the integrated stress is considered to be the sum of those contributions from the portions of the damage and range profiles lying in the still-crystalline material, together with that from the stress supported within the amorphous layers. Burnett and Page [1985] proposed a surface stress model

¹ $\langle X_D \rangle$ is the standard deviation in the depth of the damage peak position in the EDEP-1 computer code which predicts the ion distribution. If the distribution is assumed to be Gaussian, then 96% of all damage will lie in a layer $4\langle X_D \rangle$ thick.

which deals with the role of amorphization in stress relief based on the following assumptions:

- (i) the variation of surface stress (S) with dose is linear prior to amorphization;
- (ii) thermal effects, dose rates, electronic effects, etc., are negligible;
- (iii) the amorphous material is mechanically homogeneous; and
- (iv) after amorphization, the compressive stress in the surface is taken to consist of two components: the stress supported within the still-crystalline but damaged material (S_c) and the stress supported within the amorphous material (S_a). The former stress, S_c , includes two sources: S_{ca} due to the presence of the implanted atoms and S_{cd} due to the formation of other defects, e.g., Frenkel pairs.

Figure 2.5 is a schematic representation of the principles of the implantation-induced stress model. Initially, at doses below that for amorphization (region I), the integrated stress S is the sum of the implanted depth of the expected stress profile arising from implantation. Upon amorphization (region II) the integrated stress is the sum of the portion of the Gaussian implant profile remaining within the crystalline material, S_c , and the stress level supported within the now amorphous material, S_a . At higher doses a surface amorphous layer is formed (region III), and the stress contribution from the crystalline material is further reduced.

Once the range and damage profiles have been obtained, the model is controlled by four parameters, namely:

- (i) a constant of proportionality, α , which may be determined experimentally;
- (ii) the stress supported within the amorphous layer, σ_a ;
- (iii) the partitioning of the stress contributions from the still-crystalline materials into components due to the damage (S_{cd}) and due to the implanted atoms (S_{ca}), which may be represented as $\beta = S_{ca} / (S_{ca} + S_{cd})$; and
- (iv) the critical energy density at which amorphization occurs, $\Theta_{E \text{ crit}}$, which may also be determined experimentally.

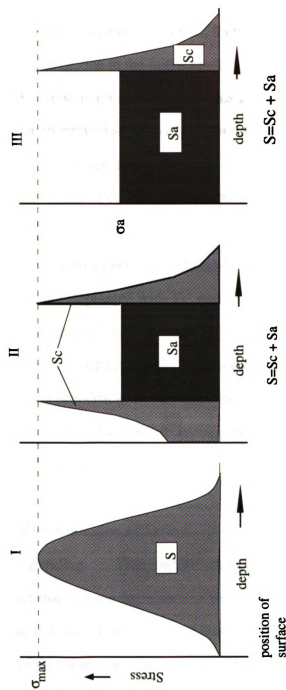


Figure 2.5 Schematic representation of the principles of implantation-induced stress model (after Burnett, P.J., and Page, T.F., 1985).

If β is small, i.e., the stress in the crystalline material is damage controlled, several features of integrated stress might be obtained in terms of comparison of σ_a and σ_{max} , where σ_{max} is the stress in the crystalline phase at the onset of amorphization (i. e., the maximum stress level obtained):

(i) if the amorphous layer supports no stress, then the integrated stress falls off dramatically after amorphization due to the initial rapid thickening of the amorphous layer, though at higher doses the stress maintains a nearly constant value;

(ii) if $\sigma_a = \sigma_{max}$ the integrated stress will continue to rise after amorphization, again gradually leveling off at higher doses; and

(iii) at intermediate values of σ_a , an initial decrease in integrated stress will be observed; however, by the time region III is reached, S may start to increase slowly.

Burnett and Page obtained a good correlation of the stress model parameters with experimental data for sapphire implanted with Ti^+ and Y^+ [Page, 1985]. Although this model described the role of amorphization in stress relief, the accuracy of this model is limited by the assumption of a sharp crystalline to amorphous transition, with an associated abrupt change in mechanical properties. In any case, this model has enabled an estimate of integrated stress values in terms of the stress relieving effects associated with the production of amorphous materials.

2.4.3.4.3 *Experimental Determination of Surface Stress*

Cantilever Beam Bending This method was first introduced by EerNisses [1971]. Based on the fact that volume expansion of targets will occur after ion implantation, the volume changes of the implanted surface layer are monitored by measuring the bending of the cantilever beam-shaped samples irradiated on one side. This bending occurs as a result of stress induced by lattice damage which causes the lattice to expand. In the direction normal to the implanted surface, the crystal lattice is free to expand, but in the lateral direction it is restricted by the much thicker underlying

undamaged lattice; and this will result in a lateral stress T . The integral, S , of this stress over the depth of the damaged layer can be expressed by:

$$S = \frac{E\delta\tau^2}{3l^2}(1-\nu) \quad (2.7)$$

where δ is the deflection of the beam, τ is the thickness, l is the length, and E and ν are Young's modulus and Poisson's ratio, respectively.

It should be pointed out that E and σ must be chosen to correspond to the crystallographic orientation of each particular sample orientation if the lateral stresses are to be compared for elastically anisotropic materials. This technique is only applied to low dose implantation where the elastic properties of the slightly damaged lattice in the bombardment layer could be assumed to be the same as for the undamaged material.

Indentation Fracture Techniques The model, proposed by Lawn and Fuller [1984], was developed for evaluating stresses in the surface of brittle materials from changes in indentation-induced crack dimensions. The basis of the model is a stress intensity formulation incorporating the solution for a penny-like crack system subjected to a constant stress over a relatively thin surface layer [Lawn, 1975; 1980]. Since the model is focused on the measurement of thin layer surface stresses, which corresponds reasonably well to the implanted layer produced by ion implantation, it may be applied in the present work. Full description on the technique will be addressed in section of experimental procedures.

2.4.3.5 Radiation Hardening and Softening Effects

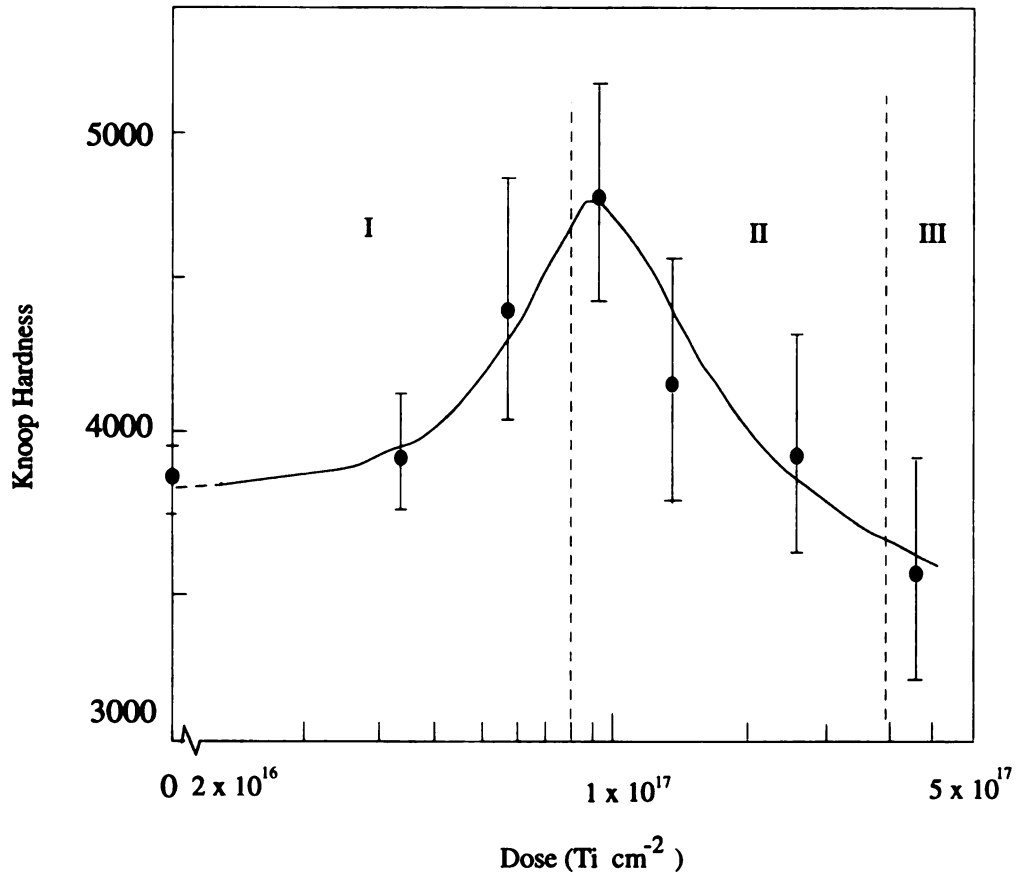
As reviewed above, an implantation process is expected to create radiation damage below the surface of a solid. As a large number of foreign atoms are forced into a host lattice, they can exist either as solutes in a metastable and strained crystalline system, as an

amorphous phase, or as a surface layer in which fine precipitates exist as a result of implantation induced heating or subsequent heat treatment of the implanted material.

Both hardening and softening by radiation in metallic and ceramic materials have been observed [Burnett: 1985; Hioki: 1986], leading to changes in microhardness, wear and friction rates, and stress-strain behavior. Hardening induced by radiation is associated with solid solution strengthening, precipitate hardening, defect hardening and the existence of compressive stress in the surface; softening has often been correlated with the presence of an amorphous layer. One hardening and softening observation by Burnett and Page [1985] is shown in Figure 2.6. The result shows that Knoop microhardness of Ti-implanted sapphire at 300 K increases from 3800 at dose of 2×10^{16} ions/cm² to 4750 at a dose of 9×10^{16} ions/cm². Beyond this dose, Knoop microhardness decreases with dose until maximum dose of 5×10^{17} ions/cm².

Ion implantation can produce substitutional or interstitial solid solutions, depending on the composition and the basic characteristics of the system and the respective equilibrium relationships. The modification of mechanical properties can be produced at the surface of the host material through one or a combination of the following: (a) formation of substitutional solid solution plus residual strain effects; (b) formation of interstitial solid solution plus residual strain; or (c) the production of high compressive stress due to second phases or volume expansion, which is associated with production of defects. Point defects and impurity atoms are believed to contribute negligibly to hardening compared to the effect of the larger defect clusters.

Precipitate hardening is associated with the formation of fine precipitates which can impede dislocation movement and thus produce a marked increase in mechanical strength. There is usually a misfit between the precipitate particle and the matrix in which the particle is lodged. If the precipitate volume is larger than the matrix it replaces, the particle acts as a point center of compression and creates a stress field in the surrounding solid. On the other



Figur 2.6 The variation of 25 g Knoop microhardness with dose for Ti implanted into sapphire (After P. J. Burnett and T. F. Page, *J. Mater. Sci.*, **20** (1985)).

hand, if the precipitate occupies a smaller volume than the material that has been replaced, there will be internal tensile stresses in the solid around the foreign particle.

The stress state induced by implantation within the implanted layer obviously affects the surface properties. In most cases, compressive stress occurs due to volume expansion. External applied load is needed to overcome the compressive stress. The existence of compressive stress can effectively retard surface crack propagation, and thus enhance surface properties such as hardness and wear resistance.

Surface softening has been clearly correlated with the formation of an amorphous layer, and the degree of softening has been shown to be dependent upon the depth of the amorphous layer [Page, 1985].

2.5 *Modification of Hardness, Toughness and Wear Resistance of Sapphire by Ion Implantation*

The surface structural change leads to surface property change. McHargue [1982] reported that a room-temperature Cr^+ and Zr^+ implanted¹ single crystal Al_2O_3 lattice was significantly damaged but remained crystalline. In this case, most of both Cr^+ and Zr^+ moved into a substitutional lattice sites, as indicated by Rutherford Back Scattering (RBS) results, increasing hardness by solution strengthening. Regarding indentation hardness, McHargue [1982] and O'Hern [1990] reported that the relative hardness of Cr^+ implanted sapphire (150 keV and 180 keV at room temperature) is 1.31 on the c-axis, and 1.23 on the a-axis. Furthermore, from the results of RBS analysis, McHargue pointed out that a major portion of the hardness increase in the Cr^+ -implanted material is due to the nearly random distribution of the ion species, perhaps interacting with the damaged Al sublattice [McHargue, 1982].

Substrate temperature modifies the hardening effect of ion implantation by influencing transient annealing and diffusion. Hioki *et al* [1986,1989] showed that at low

¹ Ion implantation conditions are 10^{16} to 10^{17} Cr^+ cm^{-2} at 280 to 300 keV and 2×10^{16} Zr^+ cm^{-2} at 150 keV at ambient temperature.

temperature (100 K), the relative hardness of the planar sapphire implanted with 300 keV Ni^+ could be increased by a factor of 1.5 at dose of 2×10^{15} ions cm^{-2} . However, above this dose, the relative hardness decreased rapidly with increased doses, reaching 0.6 at 1×10^{17} ions cm^{-2} . For the same material implanted at 300 K and 523 K, the hardness increases monotonically with the dose (up to 1×10^{17}) [Hioki, 1986, 1989]. They concluded that for 100 K implantation the increase in hardness before the dose of 2×10^{15} ions cm^{-2} was due to radiation-defect-hardening, and the following rapid decrease in relative hardness apparently resulted from the formation of an amorphous layer. The hardness increase at higher substrate temperature (300 K to 523 K) may involve contribution from solid solution hardening or precipitate hardening because of the increased concentration of implanted Ni^+ [Hioki, 1985]. Bull [1991] concluded that the increased annealing expected in damaged but crystalline samples as the substrate temperature is increased has little effect on the total radiation hardening. Some change in hardness was attributed to thermally-induced migration of implanted ions into substitutional lattice sites.

The fracture toughness, K_{IC} , evaluated by the Vickers indentation method, was found to increase with increasing doses in sapphire samples which were implanted with 300 keV Ni^+ at 100 K, 300 K and 523 K, dose up to 1×10^{17} ions cm^{-2} [Hioki, 1986]. The relative fracture toughness of planar sapphire ranged from 1.12 to 1.18 for specimens implanted either at 4×10^{15} , 4×10^{16} Cr^+ cm^{-2} at 150 keV or 1×10^{17} Cr^+ cm^{-2} at 180 keV at room temperature [O'Hern, 1990]. It is believed that compressive stress induced by ion implantation or softening and increased plasticity due to amorphization may contribute to the fracture toughness increase. Also, substrate temperature plays a very important role in the increase of fracture toughness. The results from Hioki [1989] have shown that at a given dose the implantation at 100 K is more effective in increasing K_{IC} than implantation at 300 K or 523 K. This is consistent with the observation that the compressive stress induced by implantation at 100 K is 3 to 9 times larger than that produced at 300 K.

Ion implantation can substantially modify surface and near-surface tribological properties (such as wear and friction coefficients) of sapphire plates. By performing lubricated pin-on disc tests on sapphire plates which were implanted with Ti^+ (to dose of 3.2×10^{16} and 7.7×10^{16} ions cm^{-2}) and Zr^+ (to dose of 1.7×10^{16} ions cm^{-2}) at 300 keV, it was found that ion implantation resulted in an increase in the coefficient of friction above that of the control by as much as a factor of three [Burnett, 1987]. Studies on the wear properties of sapphire [Ramos, 1992] reported that, compared with unimplanted sapphire plates, the wear scar of a disk which was implanted with 150 keV 10^{17} Ti^+ cm^{-2} was very low (less than 20 nm compared to 130 μm of unimplanted sapphire). No transfer film was formed in the disk wear track, and only a few wear particles were present on either side of the track.

2.6 Post-Implantation Heat Treatment

In section 2.4, it was stated that ion implantation produces a variety of structures, ranging from crystalline, to metastable solid solutions with a large concentrations of point defects and dislocations, to amorphous phases. These modification of surface structure are directly related to surface properties.

The response of materials to ion implantation damage varies markedly from one material to another, and thus post-implantation annealing behavior of surface structure also significantly differs. Generally, damage recovery during subsequent thermal annealing is expected to occur by epitaxial recrystallization of the amorphous layer. The final state will be dependent both on the annealing environment and on the extent of recrystallization.

The effects of post-implantation thermal annealing on structural and mechanical properties of sapphire specimen implanted with a variety of ions have been studied by a number of researchers [Naramoto, 1983; McHargue, 1987; McCallun, 1990; White, 1987; Ohkubo, 1986; Potter, 1992]. White [1987] demonstrated an annealing process for an amorphous material in which $\alpha\text{-Al}_2\text{O}_3$ was implanted stoichiometrically with Al (4×10^{16} /

cm², 90 keV) and O (6×10^{16} / cm², 55 keV) at liquid nitrogen temperature. The crystallization of the resultant amorphous Al₂O₃ during thermal annealing can be schematically illustrated as shown in Figure 2.7. Two stages are involved in the crystallization process. The first step in the annealing process is the conversion of the amorphous film to the crystalline γ -phase of Al₂O₃ . The second step is the conversion of γ -Al₂O₃ into α -Al₂O₃. This transformation takes place at a well defined interface which moves from the original amorphous/crystal interfacial region toward the free surface.

Rutherford Backscattering Spectroscopy (RBS) is often used to track the crystallization of an amorphous material during thermal annealing. By means of RBS, McHargue *et al* [1982] reported that upon annealing, the recovery of the Al sublattice in Al₂O₃ implanted with Cr at high dose began at 800°C and the O sublattice at 1000°C, and most of the Cr moved into substitutional lattice sites. In contrast to this, the results of RBS showed that the Al₂O₃ implanted with Zr was more resistant to recovery and no tendency for Zr to move into preferred sites was found. McHargue *et al* [1982] reported that the relative hardness showed an increase of about 28% for Al₂O₃ implanted with Cr, and about only 19% after the implanted Al₂O₃ was annealed at 1200°C.

2.7 *Summary of The Literature Review*

Summarizing this review on ion implantation into sapphire, it can be stated that ion implantation changes implanted sapphire surface microstructure, and creates a compressive stress region within the surface. Mechanical properties of implanted sapphire such as flexure strength, hardness, wear resistance are greatly improved. Ion implantation provides a practical and feasible means to overcome sapphire fibers' drawback, i.e., their high sensitivity to surface flaws which greatly degrade mechanical properties. As will be seen, application of ion implantation to sapphire fibers has interesting implications for performance of sapphire fibers during handling and fabrication processes.

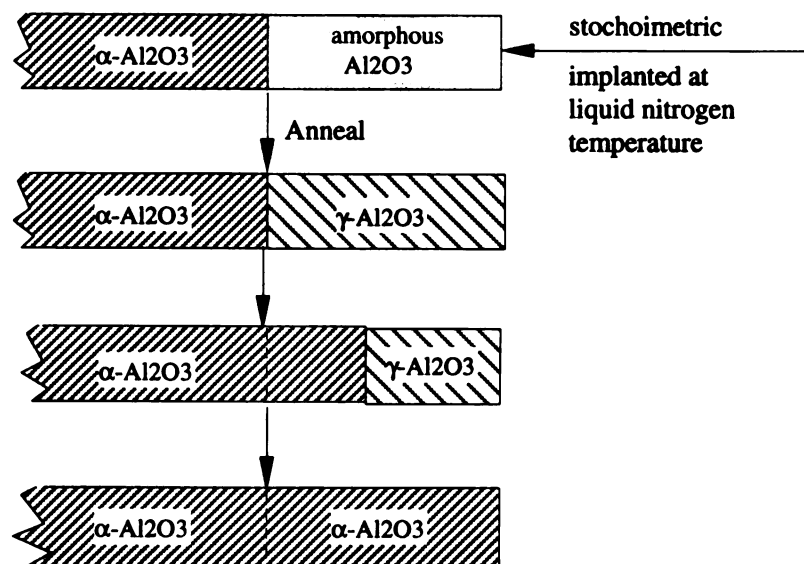


Figure 2.7 Annealing process of an amorphous layer in which $\alpha\text{-Al}_2\text{O}_3$ was implanted stoichiometrically with Al and O at liquid nitrogen temperature (after C. J. White: *Mat. Res. Sym.*, 1987)

CHAPTER III

EXPERIMENTAL PROCEDURES

In this chapter, a detailed description of experimental procedures will be given, beginning with the materials used in the work. In the section on the ion implantation process, the basic design of the Varian 350D implanter, its operation principles, and modifications made to the ion source and end station will be described. Temperature rise induced by ion irradiation will be briefly discussed. Following this, three point bend tests, abrasion protocols and microindentation test methods are described. Weibull statistical analysis was employed to analyze the characteristic bend strength. The fabrication process of NiAl/Al₂O₃ sapphire fiber composites will be detailed in section 3.7. Section 3.8 gives the full description how a transverse section TEM sample of a single crystal sapphire fiber is prepared. At the end of this chapter, transport codes which theoretically describe the distribution of energetic ions inside the target will be discussed.

3.1 *Materials*

Commercial single crystal α -Al₂O₃ fibers were obtained from Saphikon, Inc., Milford, NH. These fibers were grown by Edge-Defined, Film-fed Growth (EDFG) technique. The typical properties of sapphire fibers are summarized in Table 3.1. The total impurities in the pure Al₂O₃ were claimed to be less than 100 ppm. The orientation of the fibers is parallel to c-axis, i.e., the [0001] direction. The average diameter is about 140 μ m. According to technical data from Saphikon, Inc., these fibers were not provided with a sizing. The Young's modulus was given as 414 GPa.

Before ion implantation the fibers were soaked in ice water for 1 hour and rinsed with deionized water to remove possible contamination particles from the fiber surface, in accordance with the procedure described by Trumbauer [1992]. The fibers were

subsequently allowed to dry for a minimum of 24 hours. The cleaned and dried fibers were wrapped in acetone-washed aluminum foil and stored in a vacuum desiccator prior to further use.

Table 3.1 Properties of Sapphire Fiber.

Tensile Strength (GPa)	Young's Modulus (GPa)	Shear Modulus (GPa)	Poisson's Ratio	CTE ($\times 10^{-6} \text{ }^{\circ}\text{C}$)
2.1 ~ 3.4	414 (c-axis)	175	0.27 ~ 0.30 orientation dependent	8.8 (c-axis) 7.9 (a-axis)

The NiAl matrix material used in this study was donated by NASA-Lewis Research Center in Cleveland, OH. The binary NiAl powder was consolidated by hot isostatic pressing. The cast code was P-2306.

3.2 *Ion Implantation Process*

The ion implantation process used here involves the generation of an ion beam, mass analysis, acceleration of ion beam to high energy, rastering the beam, ion beam adjustment, target set up, and ion beam dose measurement and calculation. The following sections will detail this process.

3.2.1 *Ion Beam Generation*

A Varian 350-D medium-current ion implantation machine (on consignment from Ford Motor Co.) was used to carry out ion implantation. This implanter consists of the following major subsystems: a Freeman ion source, an ion analyzer section, the acceleration tube, a quadrupole lens, a beam mask, a target chamber, and the vacuum and coolant systems. The implanter has an energy range from 30 to 200 keV. Figure 3.1 is a schematic illustration of the 350D implanter.

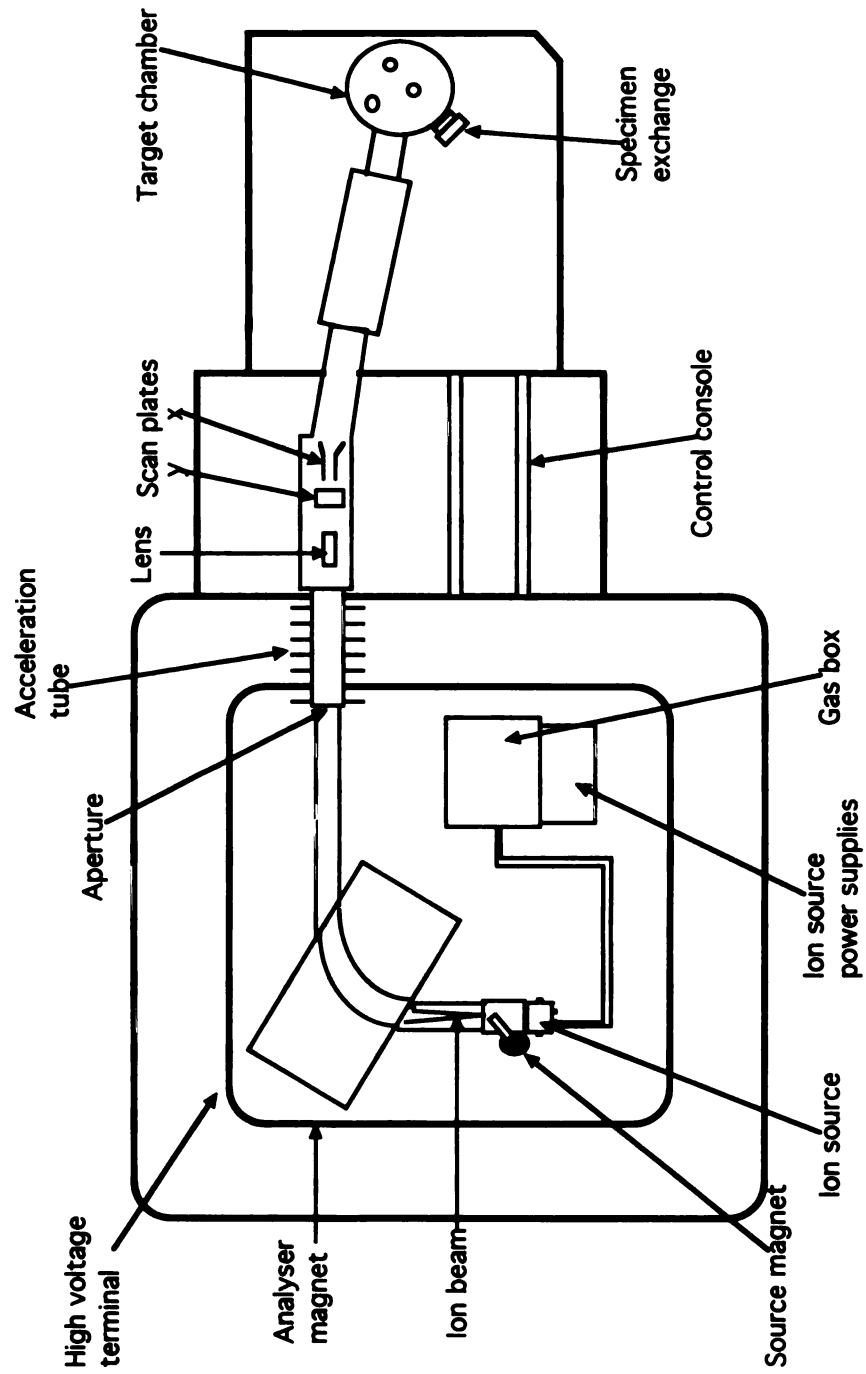


Figure 3.1 Schematic description of Varian 350-D ion implanter.

After gaseous or solid substances are ionized in the ion source, the resulting ion beam is magnetically separated according to ion mass directly after extraction from the source. The ions are then accelerated by an electrostatic field. Finally, the ion beam is directed towards the sample. In order to obtain homogenous implantation, raster scanning of the beam is generally used. The implanted dose is determined by time integration of the beam current divided by the area of coverage (see Equation 2.3).

The Freeman ion source is comprised of an oven heater, an arc chamber, a tungsten filament and an extraction slit. Figure 3.2 schematically shows the structure of the Freeman source. This segment was pumped by a diffusion pump to a vacuum of 1×10^{-6} Torr. Pure magnesium powder was placed inside the oven heater. When the oven was baked at 500°C (magnesium's melting point is 651°C , the vapor pressure is around 10^{-4} Torr at 500°C) for a period of time, vaporized species drifted into the arc chamber along with the Ar working gas. The generation of ions originates inside the arc chamber which is a cylindrical chamber of molybdenum. A tungsten filament is mounted horizontally through the arc chamber and slightly forward of the chamber axis, with its ends protruding out of the top and bottom of the chamber. Ionization begins with the application of power to the filament, causing it to heat up. When the filament reaches a certain temperature, it begins to emit electrons. Since the arc chamber is at a more positive potential than the filament, the electrons are attracted to the chamber walls, and accelerate toward them. A fraction of the electrons collide with the gas molecules inside the chamber, resulting in the formation of one or more species of positively charged ion. Several different species of ion are usually formed during the process.

Positively charged ions are extracted through a slit from the plasma by electrical attraction to an electrode which is maintained at 30 kV negative potential with respect to the arc chamber. The ion beam exits the source and enters the magnetic field of a 90-degree double focusing electromagnet. The magnet acts as a mass analyzer which separates the ions in the beam according to their charge and atomic mass. The ionized species travel

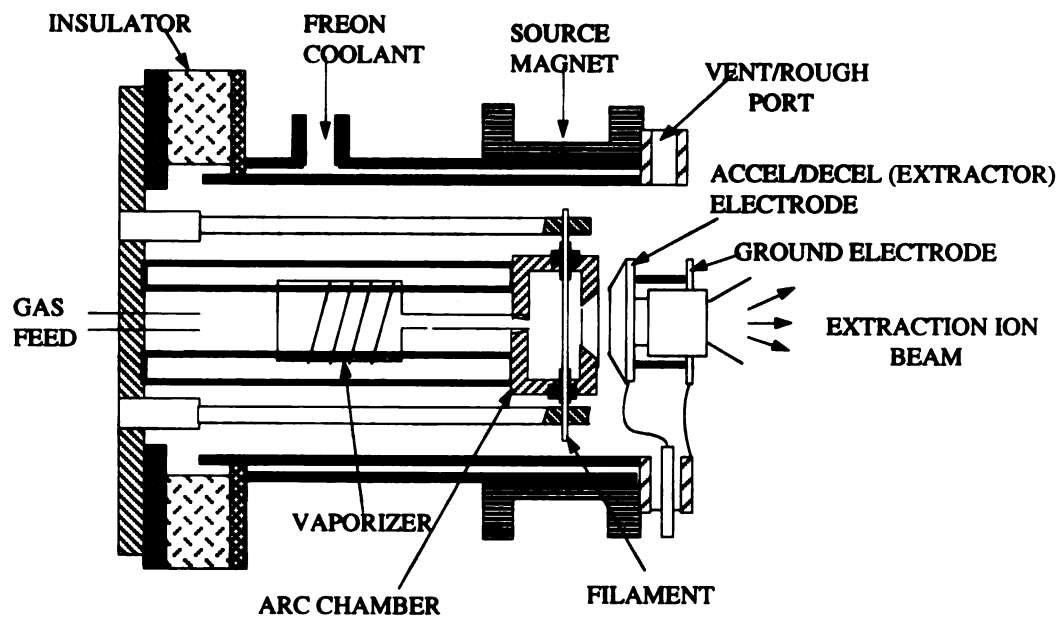


Figure 3.2 Schematic of Freeman ion source structure.

through a homogenous magnetic field and are constrained to a circular trajectory which was given by

$$R = \left(\frac{1.44}{B}\right) \left(\frac{MV}{n}\right)^{1/2} \quad (3.1)$$

where M is the ion mass in atomic mass units, V is the accelerating potential in volts, n the charge state of the ion, B the magnetic field in gauss. The particles of the same charge state and energy, but of differing mass, originating from a common source would follow paths of different radii, and thus can be separated. Through calibration, the desired ions (in present work single charge $^{24}\text{Mg}^+$ or $^{40}\text{Ar}^+$ was selected) were selected by determining corresponding magnetic field strength which aligned this beam with an aperture slit. Figure 3.3 is a mass spectrum of Mg and Ar generated in 350D implanter.

Upon completion of pre-analysis, the selected ion beam was extracted from the terminal and accelerated toward the target chamber. A high voltage acceleration tube, connecting the high voltage terminal to the beamline and the target chamber, is employed to provide the final beam energy. In the current study, the ion beam was accelerated to an energy of 175 keV in the acceleration tube.

The ion beam diverges as it gains energy through the acceleration tube. To control this, a quadrupole doublet lens is located just beyond the grounded end of the acceleration tube. The lens uses high voltage to focus the beam onto a small, symmetrical spot on the target.

After focusing, the beam is scanned vertically and horizontally by two pairs of electrostatic deflection plates. This enables a relatively large area to be covered uniformly with ions, using a small diameter, intense ion beam. The horizontal deflection plates and vertical deflection plates are driven by a specially controlled triangular wave output.

Neutral particles formed in the accelerator tube, and in the beamline beyond and in the analyzer region, are removed from the ion beam by superimposing a constant d-c offset

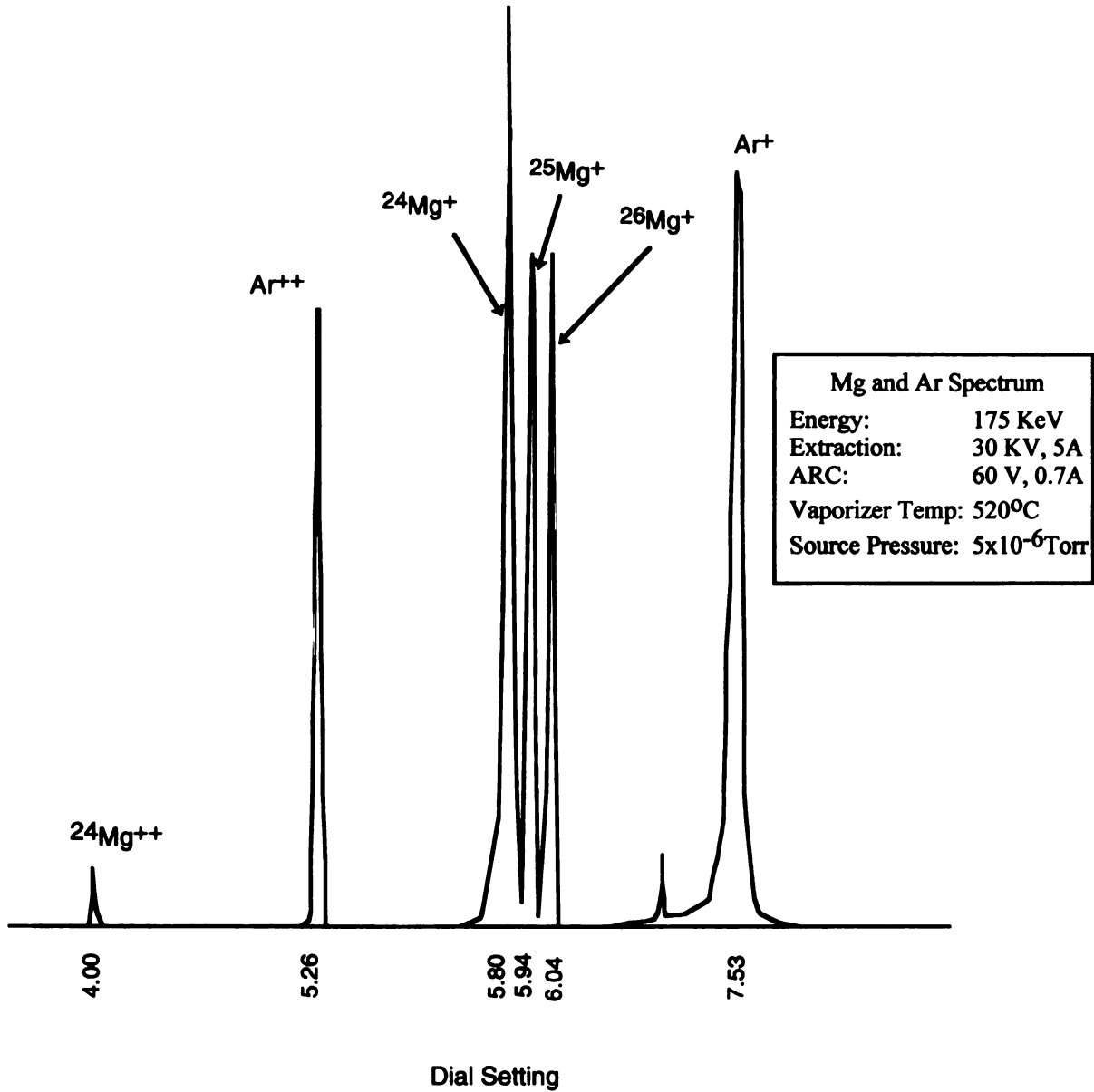


Figure 3.3 Mg and Ar mass spectrum generated in 350D implanter.

voltage to the horizontal plates, causing the beam to be deflected plus 7 degrees or minus 7 degrees off its central axis in the horizontal direction. The neutral particles in the beam are unaffected by the d-c offset voltages and continue on the original path, where they are trapped by a beam dump in the region beyond the scanner and centered between the beamline.

3.2.2 *Target Set up and Affecting Factors*

At the target end of the implanter, there is a specially designed working chamber. Inside the chamber, a specially designed rotating fixture (rotating speed 1 rpm) allows 60 fibers (150 mm length each) to be processed simultaneously with a nearly uniform irradiation of 360 degrees of fiber circumference without breaking the vacuum. On the back side of the fixture, there is a custom designed Faraday cup. This Faraday cup is placed at the central axis of the chamber, and perpendicular to incident ion beam direction. There is a 1 cm² circular hole at the center of the panel. This Faraday cup is connected to an Ampere meter so that it can monitor the ion beam current variation and also continuity of irradiation process. A schematic view of the fixture is shown in Figure 3.4 (a).

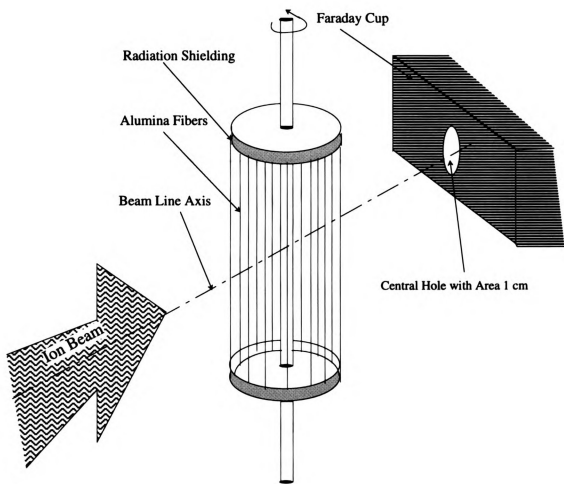
Dose calculation is based on following formula (referring to Equation 2.3)

$$D = \frac{It}{Aqe}$$

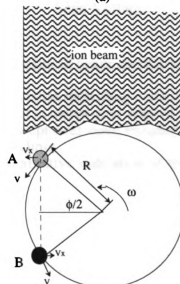
where D is the dose (ions/cm²), I is the beam current in Amperes, t is implantation time in seconds, A is beam scanning area in cm², q is the ion charge state, and e is the electron charge (1.602 x 10⁻¹⁹ coulombs).

In the measurement of ion beam current, beam current versus X or Y sweep was displayed on an oscilloscope, where beam current can be adjusted to maximum value. A typical display of beam current is illustrated in Figure 3.5. The four different regions are:

- a. flat and equal baseline section indicating total overscan of beam on mask;
- b. rise and fall as beam spot is swept over edge of mask;



(a)



(b)

Figure 3.4 Schematic of rotating fixture for ion implantation on sapphire fibers: (a) view of fixture set up; (b) estimation of dose error due to fibers shadow effects.

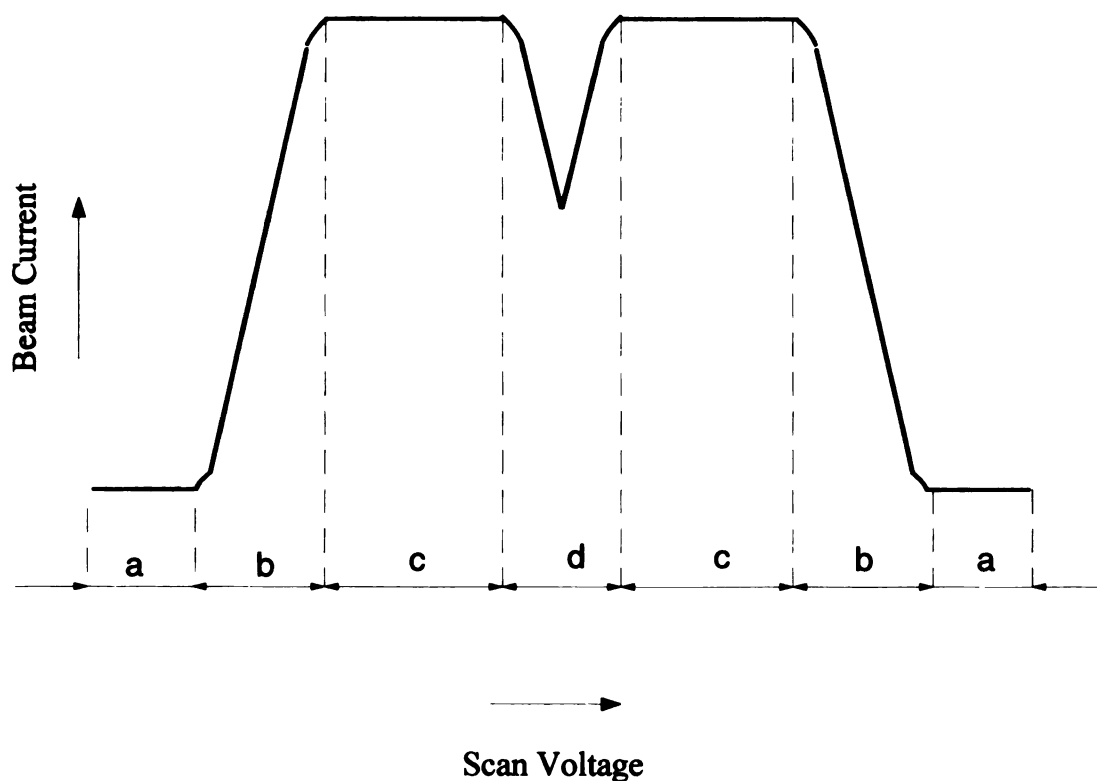


Figure 3.5 Oscilloscope display of beam current vs. X or Y scan Voltage. Four regions:
a. Flat and equal baseline section indicating correct total overscan of beam on mask;
b. Rise and fall as beam spot is swept over edge of mask;
c. Flat section as beam is swept over main Faraday indicating stable source condition and constant Faraday reading;
d. Central dip. This is a qualitative indication of the beam focus and alignment of the system.

c. flat section as beam is swept over main Faraday cup indicating stable source condition and constant Faraday reading;

d. central, only observed on the flag. This is a qualitative indication of the beam and alignment of the system.

The reading of beam current can be obtained from the main Faraday cup. After adjusting the beam current to maximum value and to full scanning area, i.e. 91 cm^2 , the dose can be calculated by equation 2.3 for the exposed time in which fibers were irradiated.

Two factors which cause ion dose error and beam heating on the sample should be considered. One was self-shadowing due to the 140μ diameter on fibers at the back side of the fixture. In the current study, a total of 60 fibers were mounted in the rotating fixture, separated by 6 degrees from each other. As shown in Figure 3.4 (b), the fiber in the position B is covered by the projection of a fiber in position A, which is separated by 6 degrees from fiber B. The tangential speed of a fiber is

$$V = \omega R \quad (3.2)$$

where ω is the rotating speed (1 rpm), R is the radius of the fixture (50 mm). Assume the projection of A moves over B (distance is $2r$) at a uniform speed $V_x = \omega R \sin(\phi/2)$, where $\phi = 6$ degree, r is the radius of a fiber (0.07 mm). Since the fixture is dynamically rotating, the relative speed is

$$V'_x = 2\omega R \sin(\phi/2) \quad (3.3)$$

Within one revolution, the covered time of fiber at position B by projection of fiber A can be obtained by:

$$\Delta t_1 = \frac{2r}{V_x} = \frac{r}{\omega R \sin(\phi/2)} \quad (3.4)$$

Similarly, the covered time by next fiber on the position of the fiber B is given by:

$$\Delta t_2 = \frac{r}{\omega R \sin\left(2 * \frac{\phi}{2}\right)} \quad (3.5)$$

Only half of the 60 pieces of fiber cause the shadowing effects on the fiber B, therefore, the total covered time within one revolution is given by:

$$T = \sum_1^{30} \frac{r}{\omega R} \left(\frac{1}{\sin\left(\frac{\phi}{2}\right)} + \frac{1}{\sin 2 * \left(\frac{\phi}{2}\right)} + \dots + \frac{1}{\sin n * \left(\frac{\phi}{2}\right)} \right) \quad (3.6)$$

The shadowing coefficient can be obtained by:

$$\begin{aligned} \eta &= \frac{T}{(1/\omega)} \\ &= \sum_1^{30} \frac{r}{R} \left(\frac{1}{\sin\left(\frac{\phi}{2}\right)} + \frac{1}{\sin 2 * \left(\frac{\phi}{2}\right)} + \dots + \frac{1}{\sin n * \left(\frac{\phi}{2}\right)} \right) \end{aligned} \quad (3.7)$$

The self-shadowing effect was thus estimated to be approximately 11 percent.

The other factor was the beam heating effect on the sample. Present implantation was carried out without target cooling at a nominal beam current of 80 μA to cover 91 cm^2 of scanning area, and some degree of heating effect was expected. The precise temperature rise depends upon a number of factors. These include the dimensions of the specimen and

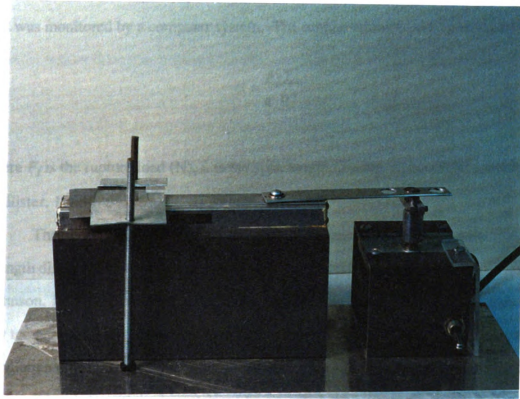
the ion beam, the emissivity of the surface and the losses by conduction to the target holder. By assuming that the sample is in poor thermal contact with the target support (the thermal conductivity of sapphire is 0.086 cal/sec - cm - °C, from Saphikon, Inc.) and that conduction losses are negligible, the Stephan-Boltzman law is used to estimate the temperature rise due to ion bombardment. By the Stephan-Boltzman law [Kern, 1950]:

$$E = \sigma (T^4 - T_0^4) \quad (3.8)$$

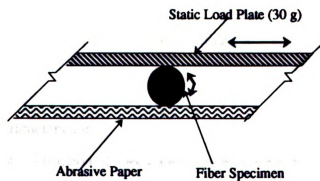
where E is the beam energy deposited on the sample, σ is the Stephan-Boltzmann constant (5.67×10^{-12} watts $\text{cm}^{-2} \text{K}^{-4}$), T is the temperature of the bombarded specimen at equilibrium and T_0 is the temperature of the surrounding. Thus a beam density of 0.879 $\mu\text{A}/\text{cm}^2$ at an ion energy of 175 keV corresponds to 0.154 watt of power for each square centimeter of the target, and the temperature rise is estimated to be less than 180°C.

3.3 *Abrasion Procedure*

Abrasion tests of the fibers were performed on a specially designed rolling-contact abrasion apparatus. Figure 3.6 shows the experimental arrangement. The sapphire fibers were placed between the load plate and the slider, which was covered by 1000 grit abrasive paper (average particle size is 5 μm). The fiber axis was kept perpendicular to the direction of the slide. The static load plate weighed 30 grams. The mobile slide, covered with abrasive paper, drove the fibers to roll back and forth between the load plate and the sandpaper by the force of friction. A 1 rpm motor was connected to the mobile slide. The speed of the mobile slide was thus given by $V = 25.4 \sin(t)$ (mm/sec). The abrasive paper was changed for each abrasion run. The abrasion protocol was carried out at room temperature without lubricant. Abrasion time ranged from 5 to 60 minutes. As will be shown later, this arrangement produced abrasion damage equivalent to that produced in tumble mill reported by Trumbauer [1992].



(a) Photograph of Abrasion Apparatus



(b) Enlarged View of Contact Area Between Fiber Specimen, Static Load Plate and Abrasive Paper

Figure 3.6 Schematic plane view of abrasion apparatus.

3.4 Three Point Bend Tests

Three point bend tests were carried out at room temperature individually on a screw-driven micro-tensile load frame. The span length was 3 mm. All samples were tested at a constant crosshead speed of 0.15 mm/min at room temperature. The rupture load was monitored by a computer system. The rupture strength was calculated by:

$$\sigma = \frac{F_f L}{\pi R^3} \quad (3.9)$$

where F_f is the rupture load (N), L is the span length (3 mm), and R is the specimen radius [Callister, 1985].

The number of test samples was at least 20 pieces for each condition. The bend strength distribution of each sample group was characterized using Weibull distribution [Johnson, 1964; Holland, 1989], since single crystal sapphire exhibits brittle fracture at low temperature. The Weibull distribution function makes it possible to estimate a population of infinite size from a small amount of data [Weibull: 1951]. In the current study, all bend strength is characterized by so-called Weibull characteristic strength, which will now be described.

The Weibull distribution function can be expressed as:

$$F(x) = 1 - \exp \left[- \left(\frac{x - x_u}{x_0} \right)^m \right] \quad (3.10)$$

where the parameters are:

$F(x)$ statistical fraction of specimen that failed at given stress or lower

x stress

x_u stress below which no specimens failed (called location parameter)

x_0 characteristic strength, stress at which 63.2 percent of specimen failed

m Weibull slope or modulus.

The three Weibull parameters, x_u , x_0 , m , are assumed to be constant of the material. When x_u is assumed to be zero, the three-parameter Weibull distribution function becomes known as a two-parameter Weibull distribution function. The Weibull slope or modulus m provides an indication of scatter or variation in the strength distribution; a small value of m indicates that a significant amount of scatter exists in the strength distribution.

Equation (3.4) can be rearranged to form an equation for a straight line as follows:

$$\ln(\ln(\frac{1}{1-F(x)})) = m(\ln(x - x_u) - \ln x_0) \quad (3.11)$$

In this form a plot of the distribution function should be linear in a coordinate system where the ordinate is $\ln(\ln(\frac{1}{1-F(x)}))$ and the abscissa is $\ln(x - x_u)$.

Johnson [1951, 1964] proposed the so-called median rank method to obtain the values of $F(x)$. In the method, the data set is arranged in order of increasing stress or rupture strength. Each value then has an order number according to its position in the list. $F(x)$ is obtained by the following formula:

$$F(x) = \left[\frac{n - (1 - \ln 2) - (2 \ln 2 - 1)(\frac{n-1}{N-1})}{N} \right] \quad (3.12)$$

where n is the position number in the ordered list and N is size of the data set. One of the median rank examples is shown in Table 3.2.

Table 3.2 Median Ranks

Sample Size = N

List	1	2	3	4	5	6	7	8	9	10
1	0.500	.2929	.2063	.1591	.1294	.1091	.0943	.0830	.0741	.0670
2		.7071	.5000	.3864	.3147	.2655	.2295	.2021	.1806	.1632
3			.7937	.6136	.5000	.4218	.3648	.3213	.2871	.2594
4				.8409	.6853	.5782.7	.5000	.4404	.3935	.3557
5					.8706	.7345	.6352	.5596	.5000	.4519
6						.8909	.7705	.6787	.6065	.5481
7							.9057	.7979	.7129	.6443
8								.9170	.8194	.7406
9									.9259	.8368
10										.9330

The value of $F(x)$ and $x - x_u$ can be plotted as $\ln \ln \left[\frac{1}{1 - F(x)} \right]$ as a function of the log of strength. The plot will be linear for the correct value of x_u , which is also called the location parameter.

If the original plot of the data is a straight line, then x_u is assumed to be zero (i.e., the minimum stress below which no specimen can fail is zero). If the original plot is concave downward, then there is some finite stress below which no specimen will fail. The true value of x_u can be found by substituting assumed values into the expression $x - x_u$ until the Weibull plot becomes linear. The bend strength data in this study have been characterized by Weibull's characteristic strength, σ_0 , i.e., the strength for failure probability of 0.632.

3.5 Indentation Fracture Tests

Figure 3.7 is a schematic diagram showing mutually orthogonal radial crack systems produced by Vickers indentation. Theoretically, the technique of indentation fracture test, proposed by Lawn and Fuller [1984], is based on two assumptions: (1) the depth of the layer (d) is small compared to that of the crack (c); and (2) the stress is uniform within this layer. Two main types of cracks exist: radial/median cracks on a symmetry plane normal to the surface and containing the load axis; and lateral cracks, on shallow subsurface planes approximately normal to the load axis. The radial crack traces on the specimen surface should constitute a sensitive indicator of the residual stress level.

Two components of the stress intensity factors are considered. First, there is the residual stress intensity factor which is produced after indentation. It can be expressed by :

$$K_r = \frac{\chi P}{c^{3/2}} \quad (3.13)$$

where P is the peak contact load, c is the characteristic crack size, and χ is a dimensionless factor which represents the intensity of the persistent field. Here, $\chi = 0.016 \frac{E}{H}$, where E is Young' modulus and H is the hardness [Hioki, 1986].

The second intensity factor arises from the surface stress. The stress, σ_s , is assumed to be uniform over the depth (d) of implanted layer, and $d \ll c$ (thin layer approximation). The stress system is considered as a surface line force, $\sigma_s d$. The appropriate stress intensity factor is:

$$K_s = 2 \Psi \sigma_s d^{1/2} \quad (3.14)$$

where Ψ is a dimensionless crack geometry term of value about unity.

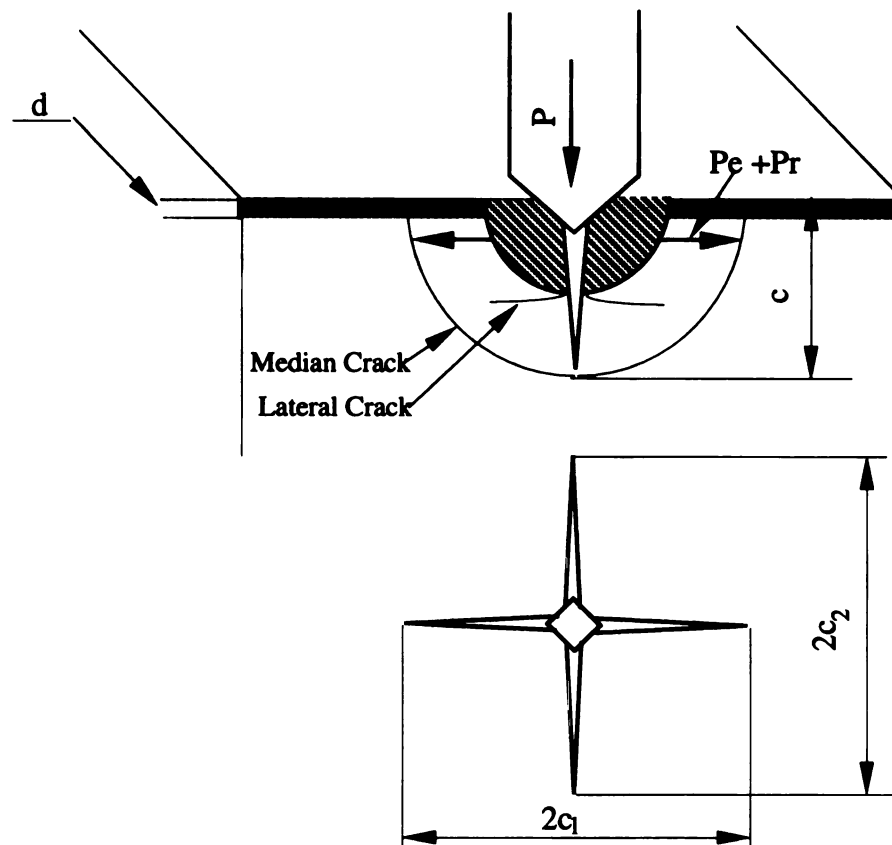


Figure 3.7 Schematic representation of the crack geometry around a Vickers indentation in a brittle material. Cracks have half penny-like geometry center about central deformation zone (shaded region). Dashed lines show lateral cracks and d is the thickness of the irradiated compressive stress layer.

Finally, provided that the surface stress layer does not alter the characteristic of the elastic-plastic properties embedded in the χ term, by the principle of superposition one can obtain the stress intensity factor for the radial crack system:

$$K = \frac{\chi P}{c^{\frac{3}{2}}} + 2\psi\sigma_s d^{\frac{1}{2}} \quad (3.15)$$

Considering the equilibrium fracture condition the crack extends when K reaches the level of the critical stress intensity, K_c (constant of bulk material), the expression can be rewritten:

$$\frac{\chi P}{c^{\frac{3}{2}}} = K_c - 2\psi\sigma_s d^{\frac{1}{2}} \quad (3.16)$$

Now, using the reference state of zero surface stress to eliminate χ , inserting $c = c_0$ at $\sigma_s = 0$, we finally have:

$$\frac{2\psi\sigma_s d^{\frac{1}{2}}}{K_c} = 1 - \left(\frac{c_0}{c}\right)^{\frac{3}{2}} \quad (3.17)$$

or

$$\sigma_s = K_c \frac{1 - \left(\frac{c_0}{c}\right)^{\frac{3}{2}}}{2\psi d^{\frac{1}{2}}} \quad (3.18)$$

Therefore, the stress evaluation is reduced to a measurement of relative crack dimension in the stressed and un-stressed states.

Vickers indentation tests were carried out on an interfacial debonding system located in the Composite Materials and Structure Center at Michigan State University. This

system was controlled by a computer in which loading and unloading rates and position of an indenter were precisely controlled. This system also provided an optical microscope in order to observe the surface topography at a maximum magnification of 100X. The Vickers indentation load was pre-set to be 100 grams throughout the tests. The indenter tip had pyramid shape and a 4 μm diagonal in length, and was made by Magwen Diamond Pro., MA. The test method was based on ASTM E384-89 (Standard Test Method for Microhardness of Materials). During the test, the sapphire fibers were cemented to a glass slide with cyanoacrylate adhesive so that the fibers were stable. The indenter contacted the sapphire fiber at a velocity of 20 $\mu\text{m}/\text{sec}$, and the time of the full load application was 15 seconds. After indentation, the leg length of the cross diagonal was measured by using optical microscopy, and the measured cross diagonal $2c_1$ and $2c_2$ were recorded as illustrated in Figure 3.7. For each implantation condition, at least 20 points of indentation were made, and the average of the diagonal length was then determined. The morphology of indentation traces was observed in SEM (Hitachi S-2500C) after light coating with Au.

3.6 *Post-Implantation Annealing*

Implanted sapphire fibers were annealed in both vacuum and air environments. Vacuum annealing was carried out in MTS 810 hydraulic servo system with a centorr vacuum furnace. The vacuum was around 1×10^{-5} Torr. Annealing temperature ranged from 1073 K to 1473 K for 1 hour. After annealing, the chamber was furnace cooled down to room temperature. The air environment annealing was only carried out at 1273 K for 1 hour. It was also furnace cooled down to room temperature.

3.7 *Fabrication of NiAl/Al₂O₃ Composite by Diffusion Bonding*

The bulk matrix material of cast NiAl was sectioned into approximately 2.5 x 0.5 x 0.3 cm plates by means of EDM. The plates were first mechanically polished on both sides with SiC paper ranging from 240 to 600 grit. Further polishing was continued using

polishing cloth and alumina powder of size ranging from 600 grit, 5 μm , 0.3 μm . When one side of the plate was polished to a surface finish of 0.5 μm , another side of the plate was superglued on a steel block, and then polished down. The final thickness was around 0.5 mm. The whole block with both sides polished was ultrasonically cleaned in acetone until the glue holding the plate is dissolved. As a result of the grinding, the bonding plates had parallel sides that helped ensure a uniform load distribution during hot pressing.

The grooves to place individual fiber on the polished NiAl plate were made by using a Material Science LTD, Model MK-II electro-discharge machine, with setting of $R = 3$, $C = 3$, and $V = 3$. A custom plunger tool, as shown in Figure 3.8, was used to machine about 250 μm diameter grooves with approximate 500 μm spacing. Figure 3.9 shows an EDMed bonding plate. After machining, the plates were degreased in a cleaning solution, then ultrasonically cleaned in warm water for 10 minutes, dried with a hot air gun, then ultrasonically cleaned again in hexane for another 15 minutes and finally naturally dried.

Sapphire fibers were placed into the groove with careful handling. After placement, both ends of the plate were taped together using a small amount of double-sided tape to ensure the that fibers remained in place. (The tape was finally burned off during vacuum hot pressing). The assembly of NiAl/sapphire fibers, schematically shown in Figure 3.10, is in a manner similar to the foil-fiber-foil technique [Mackey, 1991]. To prevent the NiAl plates from bonding to the TZM compression plates, boron nitride coated alumina plates were placed between the plates and the assembly.

The diffusion bonding process was carried out at a pressure of 2×10^{-5} Torr in a vacuum furnace of a MTS810 system. The heating rate was controlled at 36 K/min from room temperature to the maximum holding temperature 1523 K, and then a constant stress of 15 MPa was applied to the composite assembly for 3 hours with holding the temperature at 1523 K. The cooling rate was 34 K/min from the holding temperature to 723 K and then

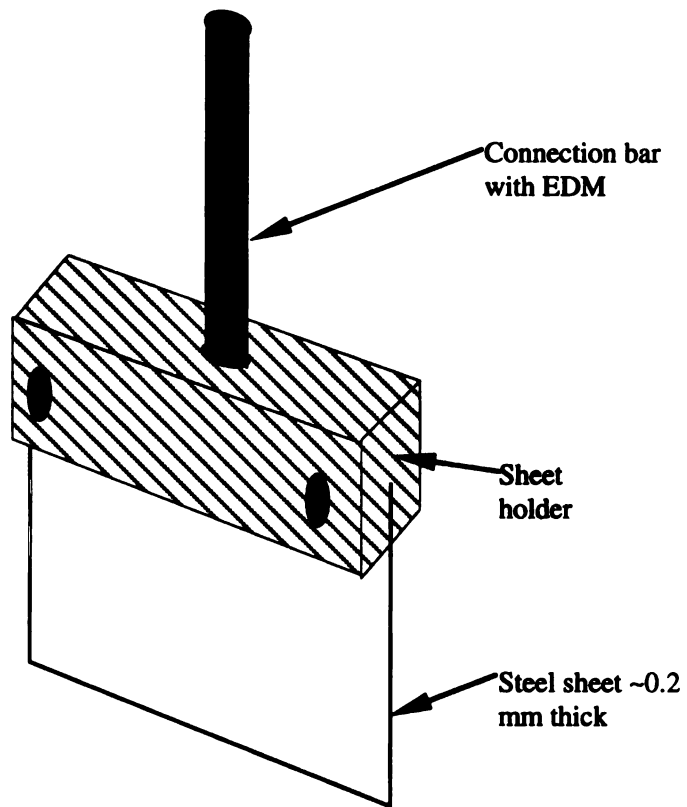
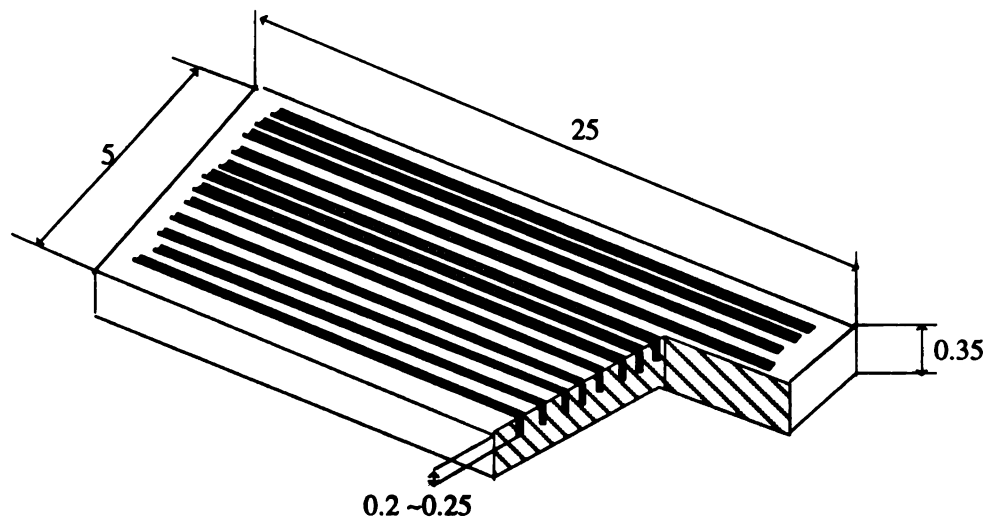


Figure 3.8 Schematic of cutting tool for NiAl diffusion bond assembly plates.



unit: mm

Figure 3.9 Schematic of EDMed NiAl diffusion bond plate.

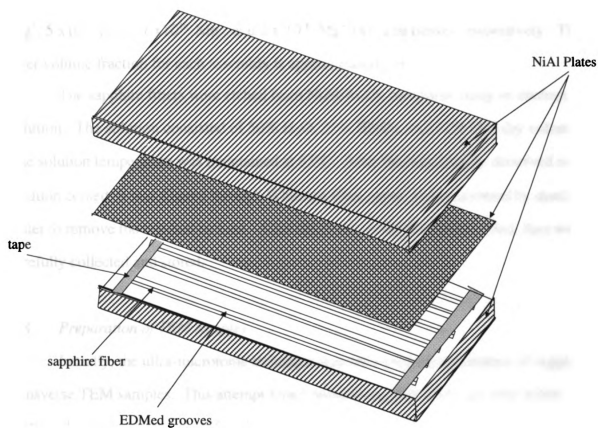


Figure 3.10 Schematic of NiAl/sapphire fiber diffusion bond assembly.

the furnace power was turned off and furnace cooled. According to previous experience [Schalek, 1995], assembly slipping could be minimized during the heating stage of the process by applying a preload of 0.5 MPa to the assembly. Once the hold temperature was attained and held for 5 minutes, the full stress was then slowly applied over a period of 5 minutes. When the furnace was cooling down, the stress was removed to minimize the composite fracture during cooldown.

The NiAl/Al₂O₃ composite in the current study includes NiAl with control sapphire fibers assembly, and NiAl with fibers implanted with 1×10^{16} Ar⁺, 4×10^{16} Ar⁺, 2×10^{16} Mg⁺, 5×10^{16} Mg⁺, 7×10^{16} Mg⁺ and 2×10^{16} Mg⁺/cm² assemblies, respectively. The fiber volume fraction for each assembly is approximately 7%.

The sapphire fibers were etched from NiAl/Al₂O₃ composite using an etchant solution. The solution consisted of 50% H₂O, 33% HNO₃, and 17% HCl (by volume). The solution temperature was maintained at 63°C. After the NiAl/Al₂O₃ dissolved and the solution cooled, it was filtered through Whitman filter paper, and then rinsed by distilled water to remove the residual etchant. After the fibers on the filter paper dried, they were carefully collected and stored.

3.8 *Preparation of TEM samples*

Initially, the ultra-microtome technique was attempted for preparation of sapphire transverse TEM samples. This attempt failed because sapphire fibers are very brittle. The sectioned samples were not uniformly electron transparent, and serious damage was caused by the diamond knife. Later, the preparation of transverse fiber TEM specimens was successfully accomplished by a technique similar to that reported by Nutt [1985]. A single layer of parallel sapphire fibers (50 pieces of sapphire fibers, 40 mm length each) was placed between two foils of 99.9% pure aluminum. The assembly was then diffusion-bonded in an argon atmosphere in an MTS 810 system by hot-pressing with 15 MPa stress at 500°C for 45 minutes, producing a composite monotape. The samples of 3 mm disc

were obtained by an ultrasonic core drill on the 6 mm by 40 mm monotape. After this, the disc was placed on an SPI Pyrex specimen mount using crystal-bond adhesive. One side of the disc was polished on 600 grit sandpaper until two thirds of the sample thickness was removed. The stub was then soaked in acetone to remove the crystal-bond. Since the sapphire fibers were very brittle, a molybdenum ring was attached to support the polished side by using a high temperature epoxy compound from Gatan which can withstand high temperatures arising from the ion mill. The sapphire fiber disc with Mo-ring was again mounted on a Pyrex stub by crystal bonding. The sample was then polished to a final thickness of approximately 60 μm . Following this, the sample was dimpled on both sides by a Gatan dimple grinder. One technique used in dimpling to control the dimpled depth was to monitor the color change of sapphire fibers illuminated by a polarized transmitted light. According to the color spectrum of sapphire with thickness, the corresponding thickness could be controlled to 40 to 50 μm . If a very perfect dimple on the sapphire fiber disc was obtained, the time required for perforation during ion mill could be dramatically reduced. Finally, the disc was ion thinned on both sides for perforation using the Ion Technology argon-beam ion mill operating at 5 kV, 100 μA per gun at a 20° incidence angle at the beginning, changed to 15° during final perforation. The TEM specimen was observed in a Hitachi H-800 microscope in the Department of Materials Science and Mechanics at Michigan State University, and in a Jeol 2000 FX at The Electron Microbeam Analysis Laboratory at the University of Michigan in Ann Arbor.

3.9 *Electron Channeling Pattern (ECP) and Atomic Force Microscopy (AFM)*

The surface microstructure of implanted sapphire fiber was also studied by ECP (Electron Channeling Pattern) using CAMSCAN model 44FE. The principle of ECP is that when the impinging electron beam from SEM interacts with the planes of the crystal being illuminated, electron diffraction occurs; as this beam is swept across the crystal, the angle of incidence changes, resulting in changing diffraction conditions. Thus, when the

imaging mode is either back-scattered electron or specimen current, the resulting diffraction pattern may be observed. The electron channeling patterns were obtained by operating the SEM in the channeling mode, i.e., basically by rocking the beam about a stationary point within each grain of interest. For metal and ceramic crystals which are free of plastic deformation, this process generates sharp, fine structured electron channeling patterns; the presence of dislocation damage causes loss of higher order lines, broadening of other lines and, for sufficiently large deformation, the loss of contrast altogether.

In the current study, ECP patterns were obtained for unimplanted and implanted sapphire fibers. The ECP pattern change with ion dose was compared with the TEM information on the same condition sapphire fibers.

A NanoScope III Atomic Force microscope (Digital Instruments Inc.) was used to extract topographical information from sapphire fibers and also to generate a quantitative surface profile of the abrasive paper. Basically, the AFM has a very sharp tip which protrudes from the underside of a small, flexible cantilever. A laser beam reflects off the top side of the cantilever onto a split photodiode. Height variation on the sample surface deflect the cantilever causing the position of the laser beam on the photodiode to change. The differential voltage from the photodiode elements provides a sensitive measure of the cantilever deflection (surface height of the sample).

By NanoScope III AFM, surface topography information on implanted and unimplanted fibers was obtained by scanning areas ranging from 5 μm by 5 μm to 100 μm by 100 μm . Further, surface roughness was analyzed by sectioning the scanning area.

3.10 *Transport Calculations of The Projected Ion Range and Damage Profile*

TRIM-90 (TRansport of Ions in Matter) designed by Ziegler [1985] calculates the penetration of ions into solid using a Monte-Carlo simulation. This program accepts a description of a complex target made up of compound materials, with up to three layers made up of different materials. It calculates both the final distribution of the ions and all

kinetic phenomena associated with the ion's energy loss: target damage, ionization and phonon production. The calculation of cascades, target displacement, replacement collision, etc., is theoretically based on following assumptions:

(1) Incident atoms having atomic number Z_1 and energy E collides with an atom of atomic number Z_2 within the target. After the collision, the incident ion has energy E_1 and the struck atom has energy E_2 . The displacement energy E_d for the target, E_b is the binding energy of a lattice atom to its site, the final energy of a moving atom, below which the atom is considered to be stopped.

(2) A displacement occurs if $E_2 > E_d$ (the struck atom is given enough energy to leave the site). A vacancy occurs if both $E_1 > E_d$ and $E_2 > E_d$ (both atoms have enough energy to leave the site). Both atoms then become moving atoms in the cascade. The energy E_2 of atom E_2 is reduced by E_b before it has another collision. If $E_2 < E_d$, then the struck atom does not have enough energy and it will vibrate back to its original site, releasing E_2 as phonons.

(3) If $E_1 > E_2$ and $E_2 > E_d$ and $Z_1 > Z_2$, then the incoming atom will remain at the site and the collision is called a replacement collision, with E_1 released as phonons. The atom in the lattice site remains the same atom by exchange. If $E_1 < E_d$ and $E_2 < E_d$ and $Z_1 > Z_2$, then Z_1 becomes a stopped interstitial atom.

(4) If $E_1 < E_d$ and $E_2 < E_d$, the E_1 becomes an interstitial and $E_1 + E_2$ is released as phonons. If the target has several different elements in it, and each has a different displacement energy, then E_d will change for each atom of the cascade hitting different target atoms.

The results of TRIM show the number of displacement collisions which records how many target atoms were set in motion in the cascade with energies above their displacement energy; and the number of replacement collision which reduces the number of vacancies, and the interstitial atoms.

TRIM also calculates sputtering, which is ballistic removal of near surface atoms from the target. When a cascade gives a target atom an energy greater than the surface binding energy of that target, the atom may be sputtered. To actually be sputtered, the atom's energy normal to the surface must be above the surface binding energy when it crosses the plane of the surface. The sputtering of a surface is described by a "sputtering yield", which is defined as the mean number of sputtered target atoms per incident ion.

The parameters which are used in calculation of TRIM are:

Ions: Mg (mass = 23.99), Ar (mass = 39.95)
Energy: 175 keV and 120 keV, respectively
Ion Angle to Surface: 0 degree
Target: Al_2O_3 , 40% of Al and 60% of O
Bottom Depth: 1 μm
Density: 3.98 g/cm^3
Displacement Energy: 18 eV for Al Atom and 72 eV for O Atom in Al_2O_3
Total Ions calculated: 4000

Typical TRIM calculation results are shown in Figure 3.11.

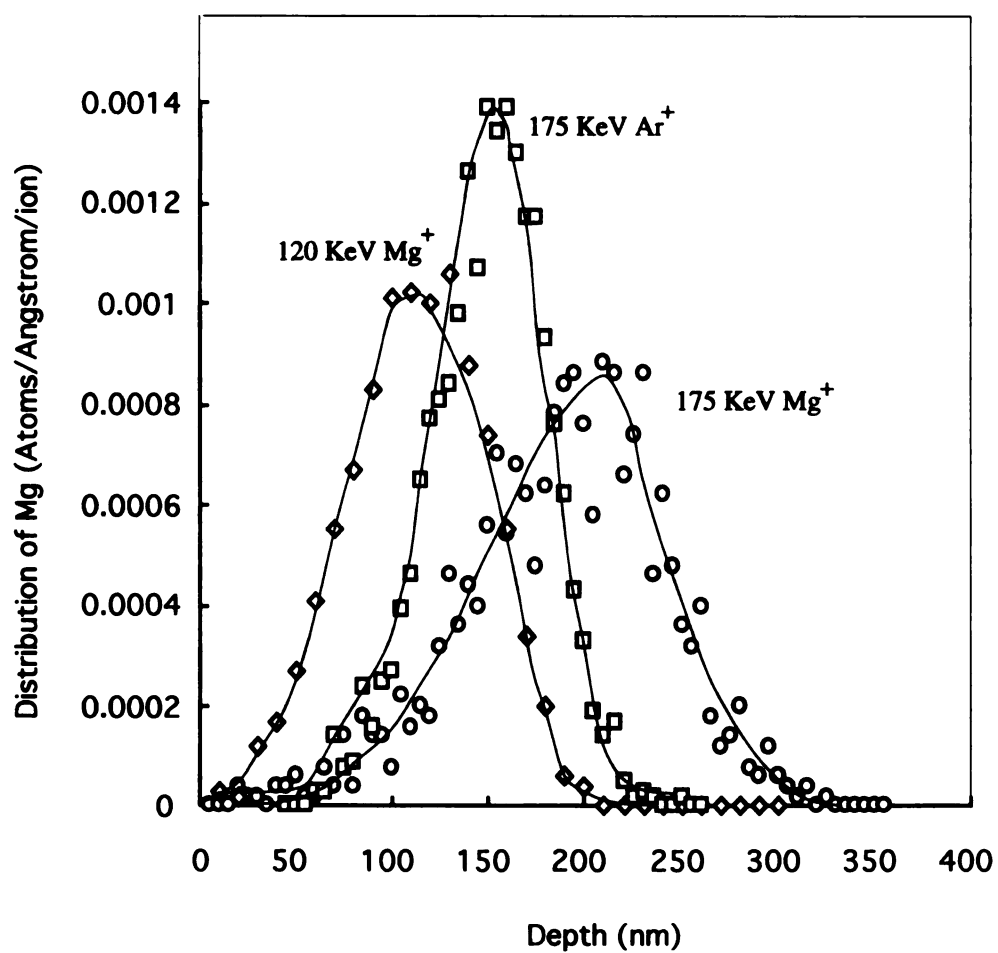


Figure 3.11 The distribution of Mg⁺ and Ar⁺ implanted into sapphire fiber at different energy, calculated by TRIM (90.05).

CHAPTER IV

EXPERIMENTAL RESULTS AND ANALYSIS

In the following section, experimental results in current work will be presented. These results include bend strength of sapphire fibers after different implantation conditions, effects of abrasion on bend strength of control and irradiated fibers, retained bend strength after a process of composite fabrication, annealing effects on bend strength of implanted fibers, estimation of surface stress by micro-indentation technique, microstructure studies by TEM, surface topography after abrasion and fracture surface observed using SEM and ESEM.

4.1 *Three Point Bend Strength without Abrasion*

Single crystal sapphire fibers were implanted at different doses of 2×10^{16} , 4×10^{16} , 5×10^{16} and $2 \times 10^{17} \text{ Mg}^+ \text{ cm}^{-2}$, and 1×10^{16} , 2×10^{16} and $4 \times 10^{16} \text{ Ar}^+ \text{ cm}^{-2}$, (Note: Zero dose refers to unimplanted or control condition). The characteristic bend strength is summarized in Table 4.1. The mean strength and standard deviation is also given in Table 4.1. For Mg^+ implantation, it can be seen that the characteristic bend strength changed very slightly with dose, from $9.31 \pm 0.48 \text{ GPa}$ for unimplanted fibers to $9.47 \pm 0.33 \text{ GPa}$ for the fibers implanted with a dose of $4 \times 10^{16} \text{ Mg}^+ \text{ cm}^{-2}$. At the maximum dose of $2 \times 10^{17} \text{ Mg}^+ \text{ cm}^{-2}$, bend strength decreased slightly to $8.21 \pm 0.32 \text{ GPa}$. The measurement of bend strength on unimplanted sapphire fiber is close to that measured by other investigators on similar material [Sayir, 1992]. The Weibull modulus is about 6.8, consistent with modulus values on Saphikon sapphire fibers reported in the literature [Bowman, 1993; Davis, 1994; Sayir, 1992]. It is apparent that Mg^+ implantation has only a very modest effect on bend strength, producing a maximum increase of only 1.5 percent for irradiation of $4 \times 10^{16} \text{ Mg}^+ \text{ cm}^{-2}$, and degrading unabraded strength by

approximately 8.8 percent for a dose of $2 \times 10^{17} \text{ Mg}^+ \text{ cm}^{-2}$. In the case of Ar^+ implantation, both measured characteristic strength and mean strength are slightly lower than that of the control fiber. For instance, the characteristic bend strength at doses of 2×10^{16} and $4 \times 10^{16} \text{ Ar}^+/\text{cm}^2$ are 8.34 ± 0.40 and $9.24 \pm 0.58 \text{ GPa}$, respectively.

Figures 4.1 and 4.2 present the Weibull plots of bend strength for different doses of Mg^+ and Ar^+ implanted fibers. In these plots, two dashed lines represent 95 percent confidence band for the bend strength of control fiber. It can be seen that most of the strength data points fall within the confidence band for both Mg^+ and Ar^+ implantation. Figure 4.3 compares the variation of characteristic strength with doses in both cases. It shows that the bend strength of Mg^+ and Ar^+ implanted fibers varies slightly from the strength of control fiber. Therefore, it is obvious that without any surface damage by handling or abrasion, ion implantation of Mg^+ and Ar^+ causes, at most, very modest changes in the bend strength of sapphire fibers.

The scatter of characteristic bend strength data comes mainly from the brittleness of sapphire fiber. Since sapphire fiber is sensitive to surface flaws, the depth of surface flaws will affect the fracture behavior during three point bend tests. According to the principle of the weakest link [Ochiai and Murakami: 1981, 1988], the most severe flaw in the bend gauge determines the fracture behavior.

It will be recalled that, in order to remove any contamination particles on the surface of the sapphire fibers, these test fibers were cleaned by soaking in ice water for 1 hour, followed by drying in air. This process might have had an effect on surface properties of the fibers since sapphire fiber is very sensitive to surface condition. Figure 4.4 presents the strength results for the fibers processed by different cleaning methods and tested in different environments. It shows that the bend strength of ice-water cleaned fiber is slightly higher than that of as-received fiber, while moisture environment has little effect on the bend strength. For instance, the characteristic bend strength for ice-water cleaned fibers is 9.3 GPa whereas the fibers were tested in dry air or 65% of humidity environments. For

Table 4.1 Three Point Bend Strength of Sapphire Fiber with Different Implant Doses (175 keV)

Ion Species	Beam Current Density (mA/cm ²)	Estimated Temperature (°C)	Dose (ions/cm ²)	Characteristic Strength (GPa)	Mean Strength (GPa)	Weibull Modulus	Number of Samples
Mg ⁺	0	0	0	9.31 ± 0.48	8.71 ± 0.52	6.83	80
	1.3	198	2 x 10 ¹⁶	8.87 ± 0.52	8.28 ± 0.59	6.57	35
	2.2	252	4 x 10 ¹⁶	9.47 ± 0.33	9.00 ± 0.39	9.43	60
	1.0	171	5 x 10 ¹⁶	9.26 ± 0.56	8.62 ± 0.53	6.41	30
	2.3	257	7 x 10 ¹⁶	8.91 ± 0.44	8.48 ± 0.20	9.26	25
	1.2	188	2 x 10 ¹⁷	8.21 ± 0.32	7.78 ± 0.20	8.65	40
Ar ⁺	1.3	197	1 x 10 ¹⁶	9.15 ± 0.33	8.31 ± 0.42	4.96	25
	1.1	179	2 x 10 ¹⁶	8.34 ± 0.40	7.34 ± 0.50	3.46	25
	0.88	160	4 x 10 ¹⁶	9.24 ± 0.58	8.55 ± 0.43	6.28	25

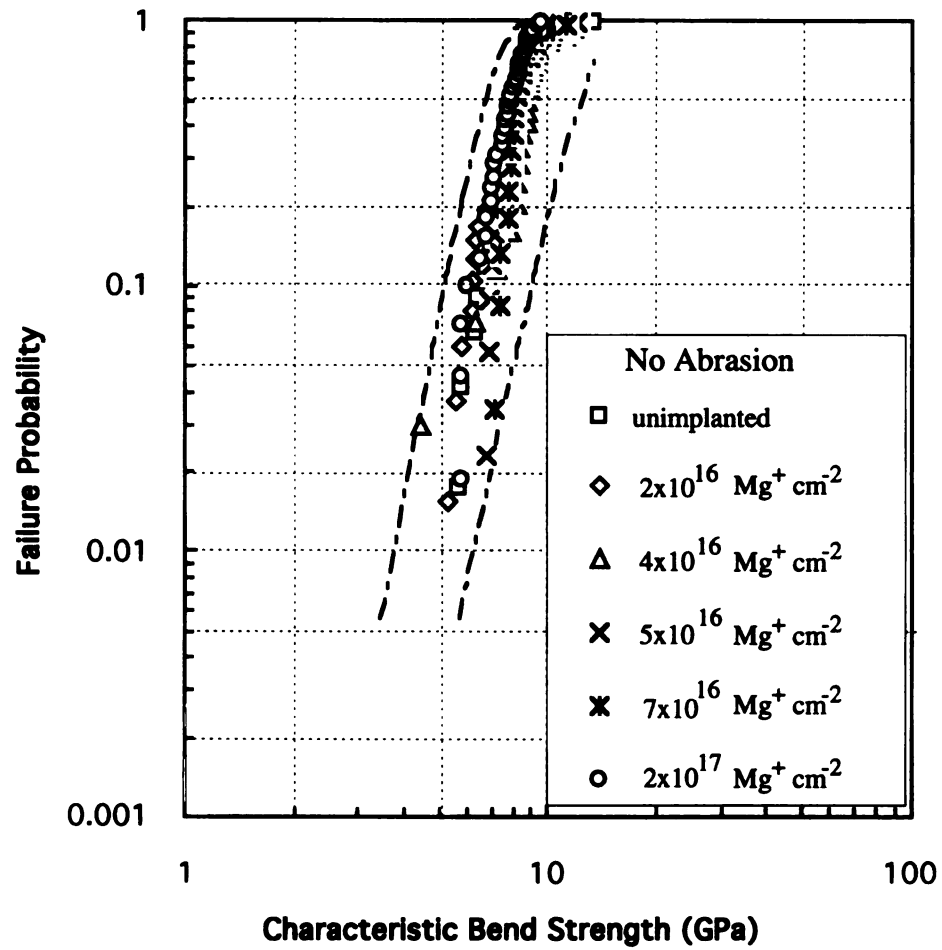


Figure 4.1 Weibull plot of bend strength for Mg⁺ implanted sapphire fiber without abrasion. Two dashed lines represent 95 percent confidence band.

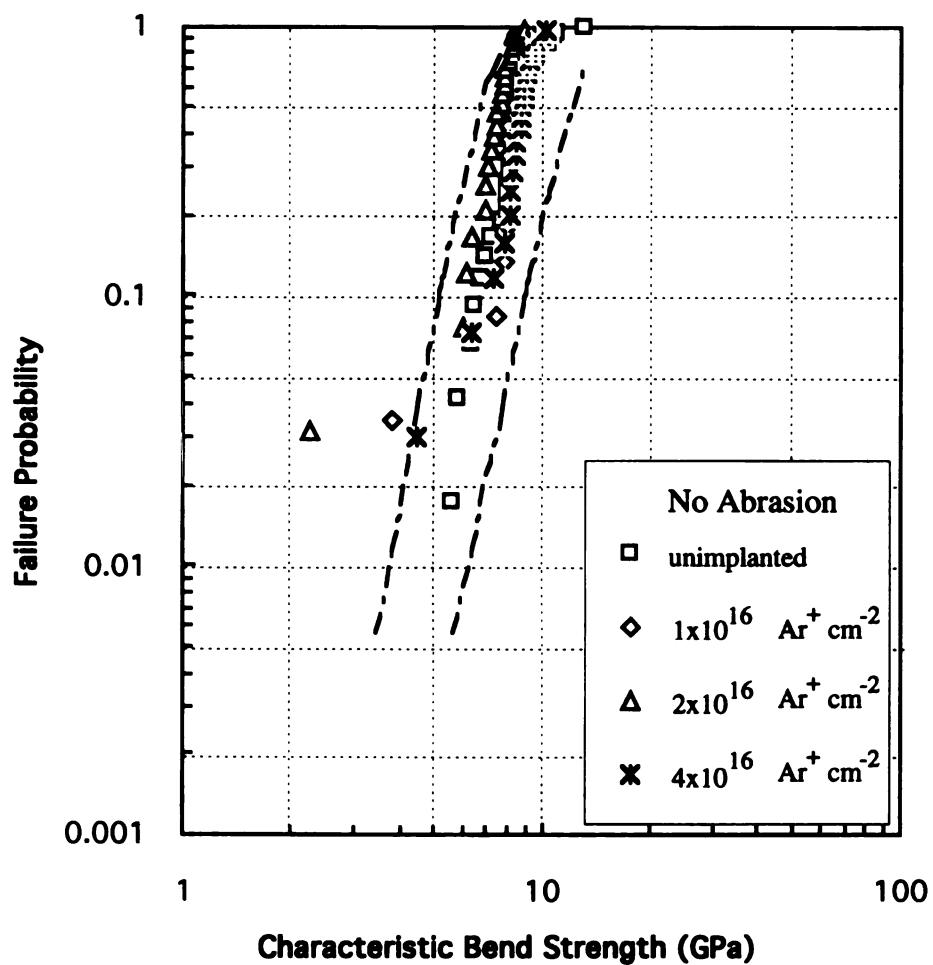


Figure 4.2 Weibull plot of bend strength for Ar^+ implanted sapphire fiber without abrasion. Two dashed lines represent 95 percent band of unimplanted sapphire fibers.

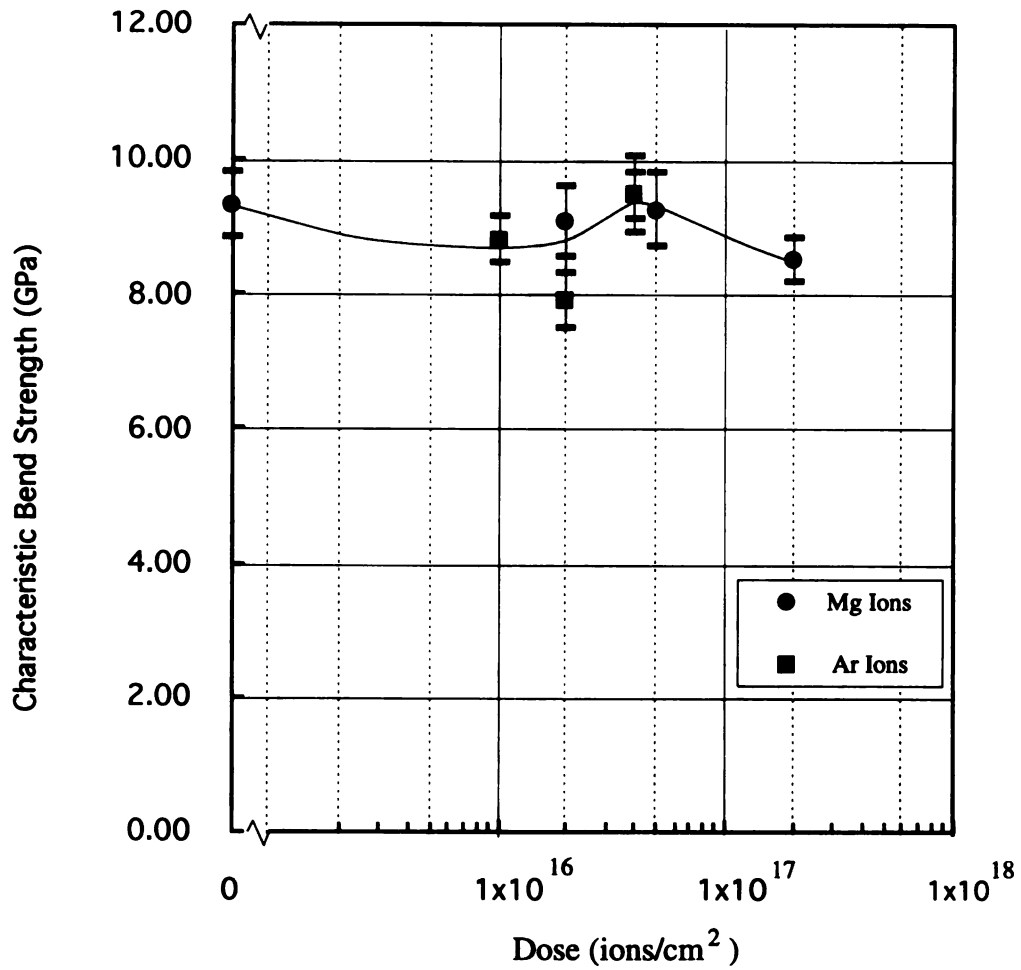


Figure 4.3 Bend strength variation for Mg⁺ and Ar⁺ implanted sapphire fibers at different ion dose without abrasion. The error bar is one standard deviation.

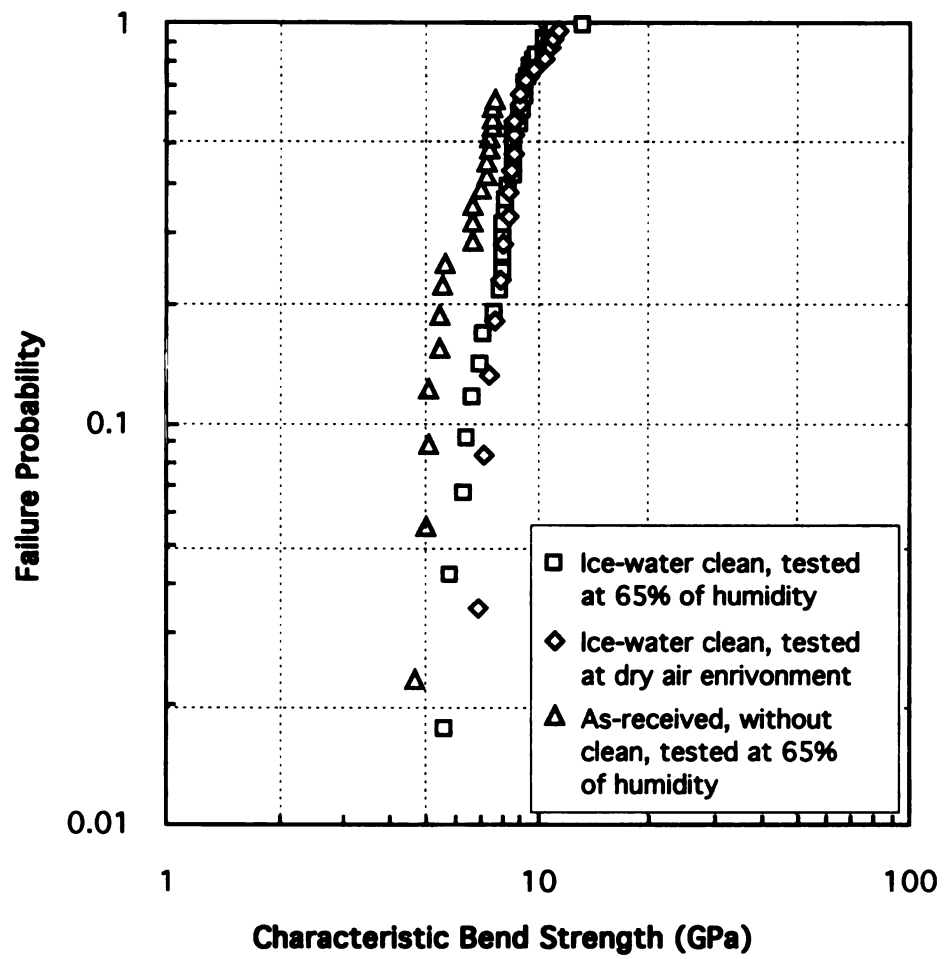


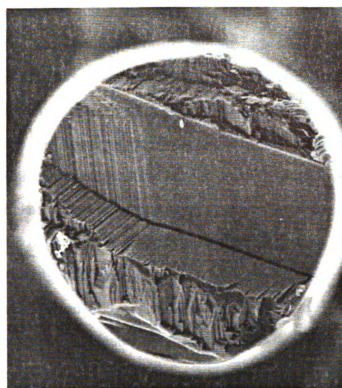
Figure 4.4 Effects of cleaning methods and testing environments on bend strength of unimplanted sapphire fibers.

as-received fibers without cleaning, the bend strength is 8.28 GPa. It has been documented that the strength degradation in the intermediate temperature region (between 200 and 600 °C) is due to stress corrosion, i.e., from chemical species in the environment reacting at crack tips and lowering the bond strength, which in turn lowers the fracture strength [Sayir, 1992; Shahinian, 1971; Heuer, 1966]. However, it is unlikely in this research that stress corrosion cracks occur in sapphire fiber at room temperature.

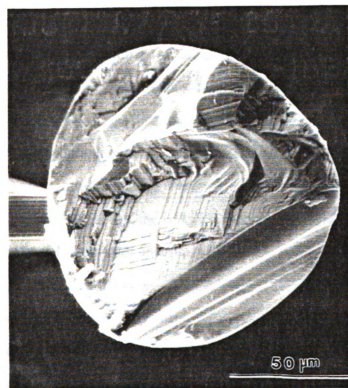
Figure 4.5 shows the SEM observation on the fracture surface for both implanted (dose of $5 \times 10^{16} \text{ Mg}^+/\text{cm}^2$) and unimplanted fibers. It illustrates fully brittle fracture features and shows no substantial difference between the two conditions. The site of crack initiation could not be determined.

4.2 *Effect of Abrasion on Bend Strength*

Abrasion causes markedly different bend strength degradation in control and irradiated sapphire fibers. In the current work, fibers were implanted at doses of 2×10^{16} , 4×10^{16} , 5×10^{16} , and $2 \times 10^{17} \text{ Mg}^+ \text{ cm}^{-2}$, and were subjected to the controlled abrasion process. The results show that there was a significant decrease in bend strength for unimplanted fibers after abrasion, whereas the bend strength of implanted fibers was close to original strength. Table 4.2 summarizes the bend strength change for different abrasion conditions. Figure 4.6 represents the bend strength change with implantation doses of Mg^+ at different abrasion times. It can be observed that abrasion causes strength deterioration, but the extent of degradation depends on surface condition. For unimplanted fibers, the bend strength retention is 51 percent of initial strength after abrasion of 10 minutes; the value rises to 89 percent for fibers irradiated at a dose of $2 \times 10^{16} \text{ Mg}^+ \text{ cm}^{-2}$, and reaches 93 percent for the highest dose of $2 \times 10^{17} \text{ Mg}^+ \text{ cm}^{-2}$. For two other intermediate doses, strength retention is above 72 percent after 10 minute abrasion. Figure 4.7 and Figure 4.8 illustrate the Weibull plots of characteristic bend strength versus failure probability for fibers implanted with Mg^+ and Ar^+ at abrasion times of 20 and 60 mins, respectively. In



(a) unimplanted



(b) $5 \times 10^{16} \text{ Mg}^+/\text{cm}^2$

Figure 4.5 SEM observation on the fracture surface for both unimplanted and implanted sapphire fiber.

these figures, two dashed lines still represent the 95 percent confidence band of bend strength for as-received fibers without abrasion, and are included for reference purposes. It is clear that all lines of failure probability versus strength have been shifted to the left, i.e., characteristic bend strength has been degraded due to abrasion. However, the extent of degradation depends significantly upon irradiation dose. It is worth noticing that the curve of failure probability vs. characteristic bend strength for as-received fibers shifted left away from the lower band of the confidence interval, while the curves of implanted fibers, either Mg^+ or Ar^+ , still fell within the band of the confidence interval. Statistically, one can say with confidence that abrasion causes significant strength degradation on as-received fibers, but no significant degradation on implanted fibers.

The strength loss of unimplanted fibers is comparable to the losses reported by Trumbauer [1992] in which a tumble-mill self-abrasion treatment performed on unsized sapphire fibers resulted in 30 percent strength degradation. Therefore, the abrasion conditions in the current work are somewhat more severe than in a tumble mill. Relating these results to the sapphire fiber handling and shipping process as well as the hot pressing process for sapphire fiber reinforcement composite material, it is obvious that surface damage by abrasion processes will significantly reduce strength.

The fiber surface topography was examined by ESEM (Environment Scanning Electron Microscope) after abrasion testing. Figure 4.9 shows ESEM micrography of sapphire fibers. It is clearly evident that the surface condition of unimplanted fibers is worse than that of implanted fibers after abrasion whereas the surface conditions of the implanted fiber changes little after abrasion. Even though little direct evidence about the depth of surface flaws after abrasion is available, this topographical information is still consistent with the results of bend strength, in which bend strength retention of unimplanted fibers is 48 to 62 percent while retention can reach 90 percent or above for implanted fibers after abrasion.

Table 4.2 Effect of Abrasion on Bend Strength of Sapphire Fibers

Dose (ions/cm ²)	Abrasion Time (min)	Weibull Modulus	Rupture Characteristic (GPa)	Strength Mean (GPa)	Strength Retention ¹ (%)
0	0	6.83	9.31	8.71	100
	5	4.51	5.70	5.20	61
	10	5.16	4.73	4.35	51
	20	3.52	5.78	5.20	62
	40	5.04	5.12	4.70	55
	60	4.29	4.51	4.08	48
2x10 ¹⁶ Mg ⁺	0	6.57	8.87	8.28	95
	5	7.09	8.22	7.71	88
	10	6.88	8.33	7.81	89
	20	6.78	8.40	7.87	90
	40	4.41	7.73	7.04	83
	60	7.60	7.79	7.34	84
4x10 ¹⁶ Mg ⁺	0	9.43	9.47	9.00	102
	10	4.71	7.08	7.47	76
	20	4.19	7.48	6.79	80
5x10 ¹⁶ Mg ⁺	0	6.41	9.26	8.62	99
	5	4.95	7.42	6.83	80
	10	5.35	6.74	6.23	72
	20	4.43	7.57	6.87	81
	40	8.14	8.26	7.79	89
	60	4.66	7.58	6.95	81
2x10 ¹⁷ Mg ⁺	0	8.65	8.21	7.78	88
	5	10.20	8.45	8.06	91
	10	10.97	8.66	8.28	93
	20	5.54	7.84	7.23	84
	40	6.99	8.09	7.56	87
	60	5.20	8.15	7.48	88
1x10 ¹⁶ Ar ⁺	0	4.96	9.15	8.31	98
	20	4.68	6.44	5.87	69
	60	3.93	6.83	6.17	73
2x10 ¹⁶ Ar ⁺	0	3.46	8.34	7.34	89
	20	3.92	7.05	6.36	76
	60	6.71	7.14	6.66	77
4x10 ¹⁶ Ar ⁺	0	6.28	9.24	8.55	99
	20	7.28	7.71	7.23	83
	60	5.82	7.54	6.88	81

¹ The strength retention is the ratio of bend strength to that of as-received condition, i.e. to the characteristic bend strength 9.31 GPa.

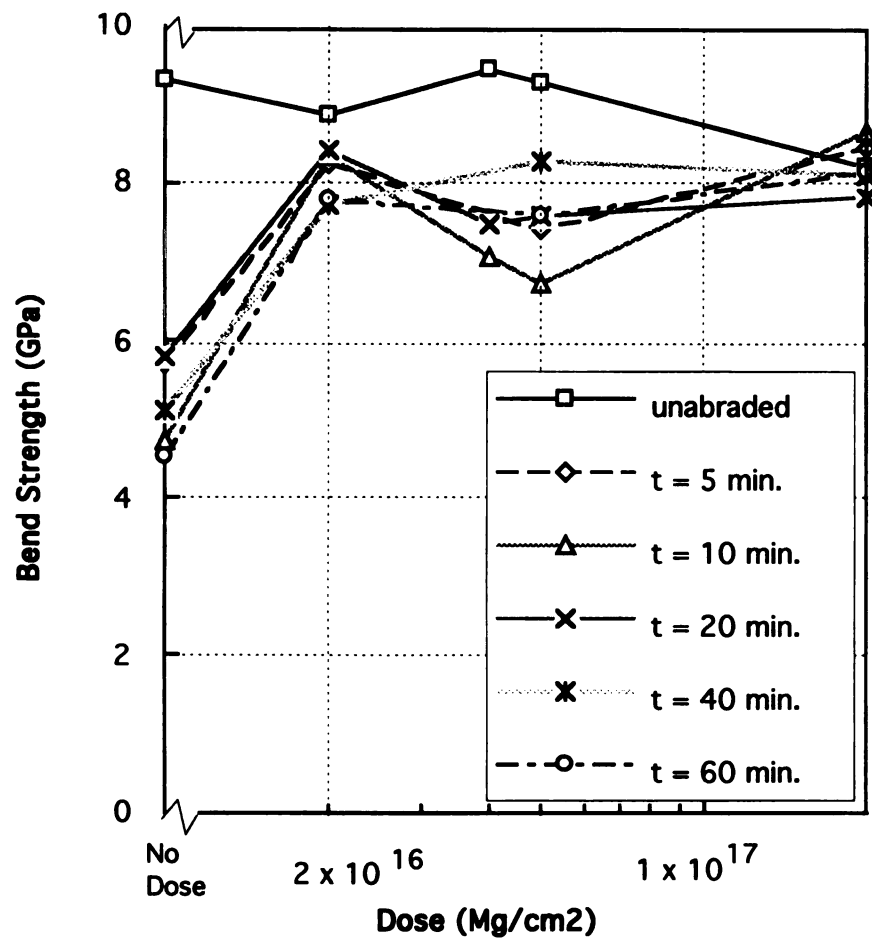


Figure 4.6 Effect of abrasion on bend strength of sapphire fibers.

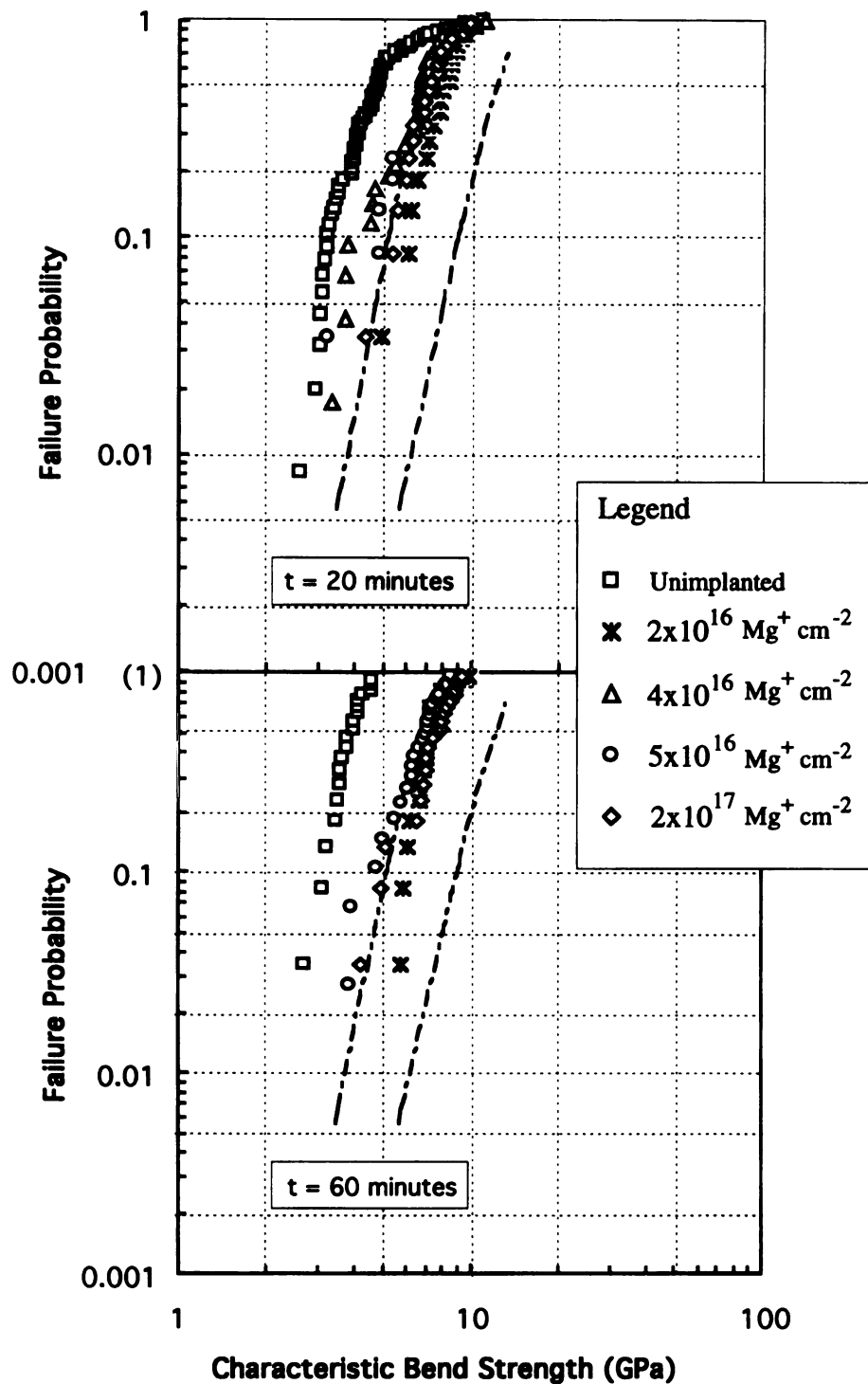


Figure 4.7 Weibull plot of bend strength for Mg^+ implanted sapphire fibers abraded 20 and 60 minutes, respectively. The two dashed lines represent 95 percent confidence band of bend strength for unimplanted sapphire fibers at room temperature without abrasion.

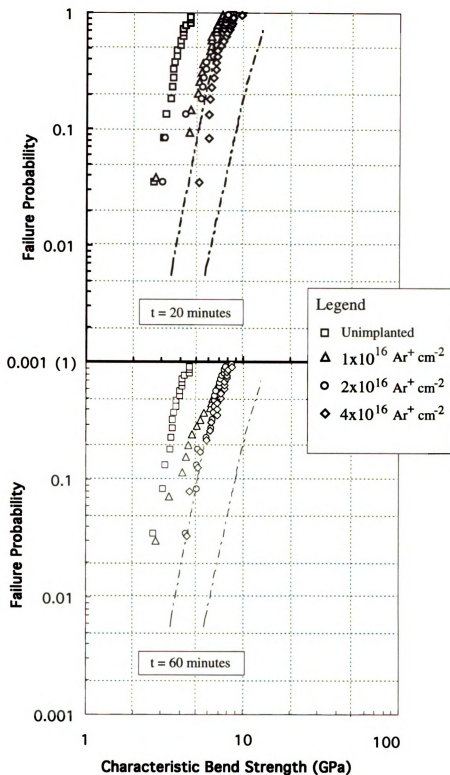
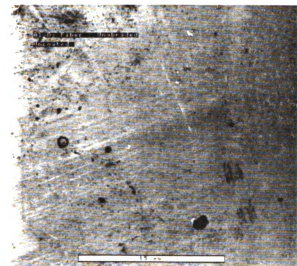
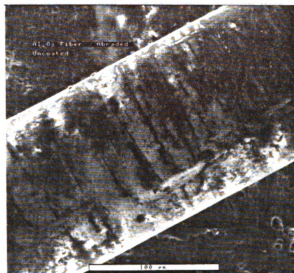


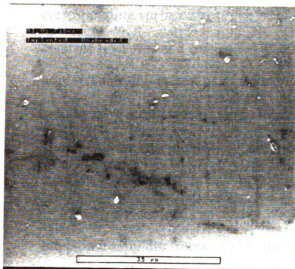
Figure 4.8 Weibull plot of bend strength for Ar^+ implanted sapphire fibers abraded 20 and 60 minutes, respectively. The two dashed lines represent 95 percent confidence band of bend strength for unimplanted sapphire fibers at room temperature without abrasion.



(a) Non-implantation without abrasion



(b) Non-implantation with abrasion (60 min)



(c) Implantation without abrasion
($2 \times 10^{17} \text{ Mg}^+ \text{ cm}^{-2}$)



(d) Implantation with abrasion (60 min)
($2 \times 10^{17} \text{ Mg}^+ \text{ cm}^{-2}$)

Figure 4.9 ESEM images on the surface topography of sapphire fibers for different implantation and abrasion conditions. (a) unimplanted and unabraded; (b) unimplanted and abraded 60 minutes; (c) implanted ($2 \times 10^{17} \text{ Mg}^+ \text{ cm}^{-2}$) and unabraded; (d) implanted ($2 \times 10^{17} \text{ Mg}^+ \text{ cm}^{-2}$) and abraded 60 minutes

4.3 *Surface Residual Stress Determined by Micro-Indentation Fracture*

The Vickers indentation technique was used to estimate the residual stress in the implanted zone according to the methods described in 3.5. Table 4.3 lists the corresponding indentation crack length at different dose. Each average crack length was measured on basis of at least 20 indentation cracks.

Table 4.3 Micro-indentation Crack Length at Different Dose

Dose	unimplanted	$1 \times 10^{16} \text{ Ar}^+/\text{cm}^2$	$2 \times 10^{16} \text{ Mg}^+/\text{cm}^2$	$5 \times 10^{16} \text{ Mg}^+/\text{cm}^2$	$2 \times 10^{17} \text{ Mg}^+/\text{cm}^2$
Crack Length (μm)	32.47 ± 3.1	23.59 ± 3.3	22.52 ± 3.8	22.03 ± 2.5	20.45 ± 3.7

Figure 4.10 shows the SEM images of indentation crack traces for different implantation conditions. It is obvious that the indentation crack length on the implanted sample surface is shorter than the unimplanted fibers. According to Equation 3.18, the corresponding surface stress can be calculated. Here, it was assumed that unimplanted (or control) fiber was at a zero stress state. The integrated residual compressive stress in the implanted region increases as a function of dose as shown in Figure 4.11. The residual compressive stress was found to reach a maximum 2.8 GPa at a dose of $2 \times 10^{17} \text{ Mg}^+ \text{ cm}^{-2}$. This measured residual compressive stress is the same order as that measured by cantilever beam bending by Burnett and Hioki [Burnett, 1985; Hioki, 1989].

This technique can also be used to evaluate the apparent fracture toughness of implanted sapphire fibers. Using the equation of Lawn [1980] for calculating radial cracking around a Vickers indentation, the apparent fracture toughness K_C may be written as:

$$K_C = 0.0139 \frac{E}{H} P c^{3/2} \quad (4.1)$$

where c is the radial crack length in indentation, H is the hardness of sapphire fiber (2000 Kg/mm², from Saphikon, Inc.), E is Young's modulus along c-axis of sapphire fiber (414 GPa), and P is load (100 g in the present study). The apparent fracture toughness was found to increase with implantation dose as shown in Figure 4.12. Compared with unimplanted fibers, the fracture toughness of sapphire fibers at a dose of 2×10^{17} Mg⁺ cm⁻² increased to almost twice as that of unimplanted fibers. For other doses, the apparent superficial fracture toughness increases over 50 percent.

Changes in the indentation fracture behavior by ion implantation will arise mainly from (1) the generation of surface residual stress [Burnett and Page, 1984, 1985] and/or (2) the increased surface plasticity accompanied by the implantation-induced surface amorphization [Hioki, 1986]. The increase in measured K_C has been qualitatively attributed to radial cracks shortened by the existence of surface compressive stresses generated by ion implantation. It is well known that ion implantation has two main effects on the indentation fracture behavior of brittle materials. First, a suppression of lateral crack breakouts takes place, together with a suppression of subsurface lateral crack propagation or nucleation. Second, a small but significant decrease in the extent of the radial crack trace on the test surface yields an apparent increase in the K_C value.

It should be pointed out that the fracture toughness K_C change due to ion implantation is a so called 'apparent' fracture toughness. Because of ion implantation, the near surface microstructure has been changed, therefore, the resistance of surface to fracture has also been changed, but not the material below the irradiated depth. Apparent fracture toughness is different from bulk material's fracture toughness.

Since micro-indentation tests were directly done on sapphire fiber surfaces, it is necessary to make some comments on the technique. It has been shown that indentation fracture technique can measure the compressive stress induced by ion implantation [Burnett and Page, 1984, 1985; Hioki, 1986]. The indentation fracture around a Vickers indentation trace in brittle single crystal materials, however, is strongly anisotropic, i.e., it

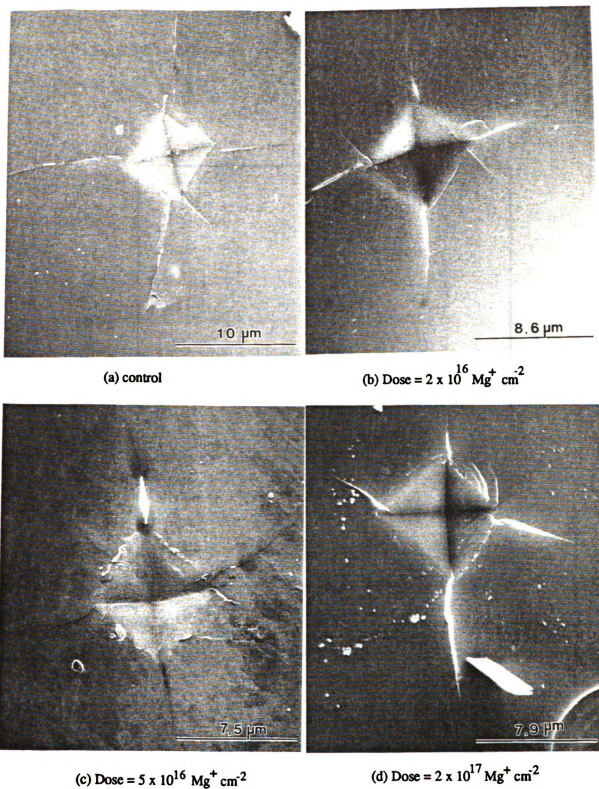


Figure 4.10 SEM images of the indentation traces on sapphire fibers at different doses (load 100 grams). (a) unimplanted; (b) $2 \times 10^{16} \text{ Mg}^+ \text{ cm}^{-2}$; (c) $5 \times 10^{16} \text{ Mg}^+ \text{ cm}^{-2}$; (d) $2 \times 10^{17} \text{ Mg}^+ \text{ cm}^{-2}$.

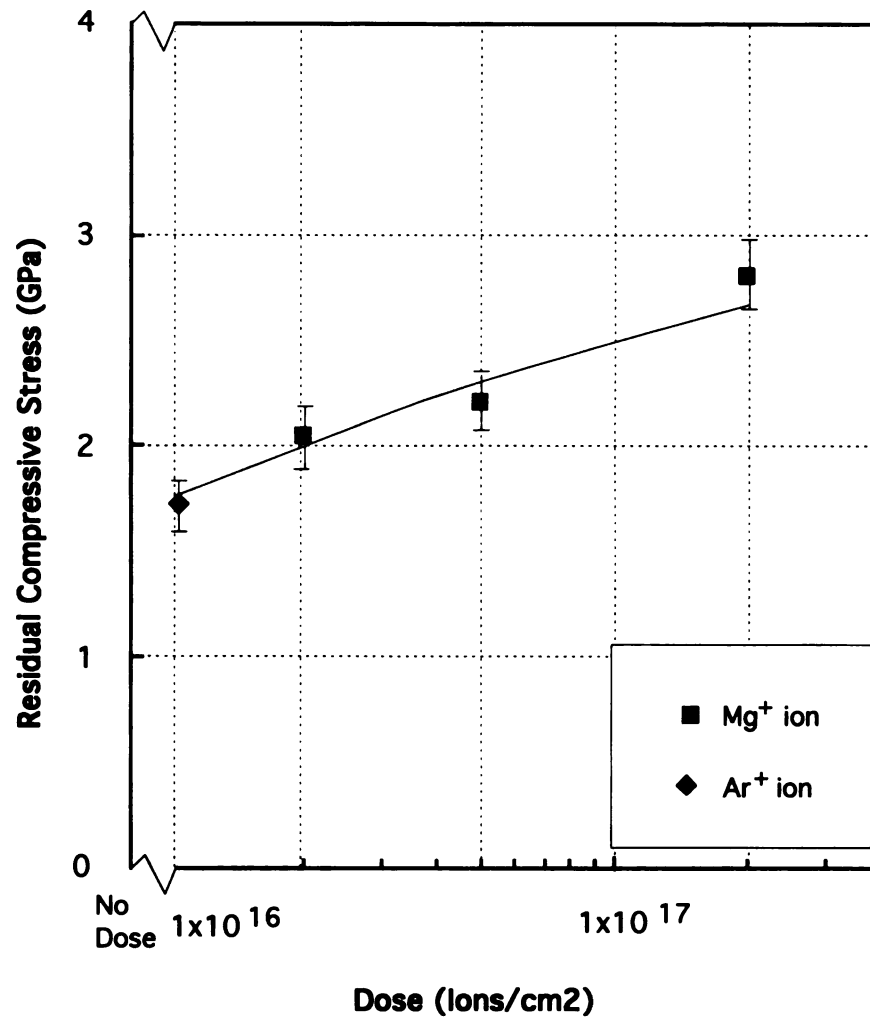


Figure 4.11 Variation of integrated surface stress with doses of Mg^+ implantation into sapphire fibers. The error band is one standard deviation. The stress is compressive.

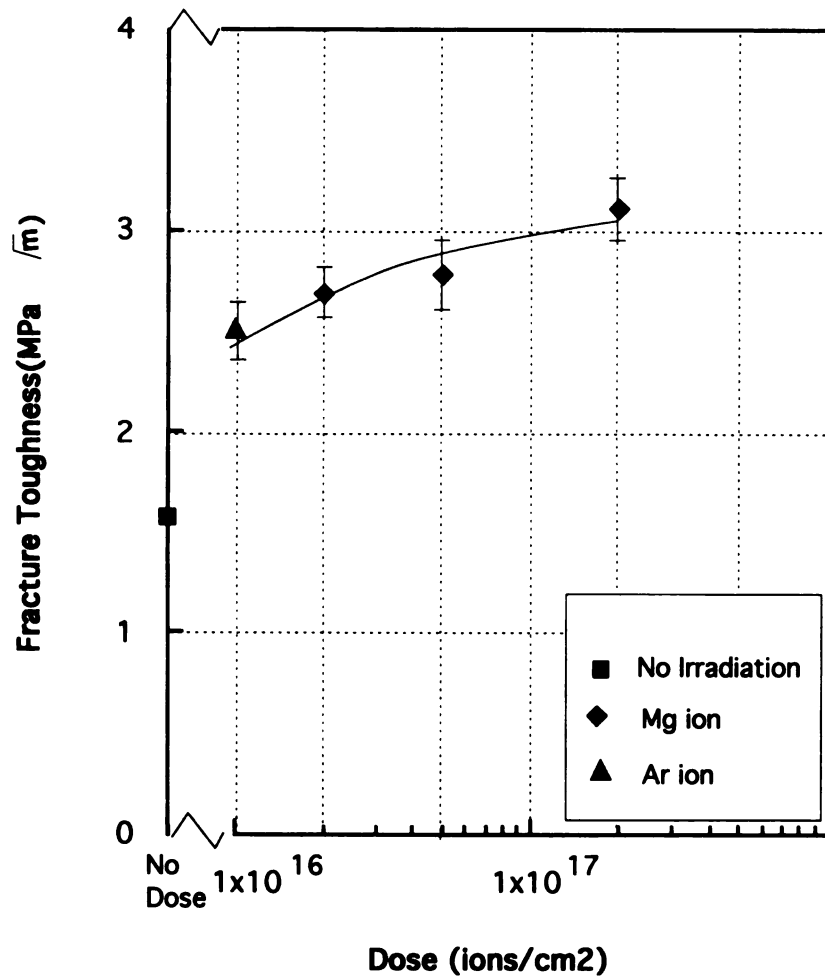
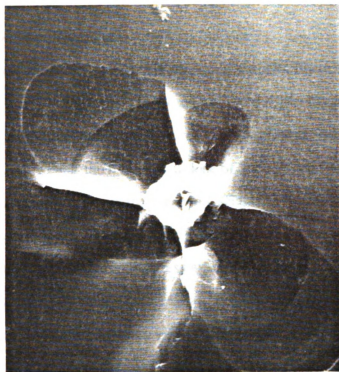


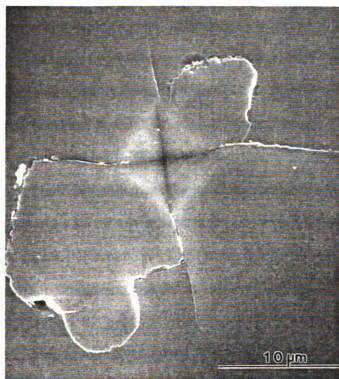
Figure 4.12 Variation of surface indentation fracture toughness (K_c) with doses. The error band is one standard deviation.

changes with the orientation of the planes of easiest cleavage with respect to the tensile components of the indentation stress field. Burnett and Page [1984] have summarized a stereogram of single crystal sapphire, which shows the crystallography of possible median/radial crack systems. For instance, for a $(10\bar{1}2)$ test surface, only one of the $\{2\bar{1}\bar{1}0\}$ cleavage planes forms, i.e., $(\bar{1}2\bar{1}0)$ is perpendicular to the surface and produces a $[10\bar{1}\bar{1}]$ crack trace. Of the $\{10\bar{1}2\}$ cleavage forms, both $(0\bar{1}12)$ and $(\bar{1}102)$ are very nearly perpendicular to the test surface producing the near-orthogonal $\langle 2\bar{2}01 \rangle$ traces. Therefore, the tested surface should be kept perfectly flat in order that the crystallography could be determined and measurement of radial cracks could be accurate and reproducible. In our current indentation test, the diagonal of pyramid Vickers indenter is $4\text{ }\mu\text{m}$. Compared this diagonal with corresponding curve with radius of $70\text{ }\mu\text{m}$, the error is 0.05%. The contact surface, thus, is assumed to be flat. In addition, extreme care was taken to align one of pyramidal edge with respect to $[0001]$ direction. The tested surface should thus be one of prism planes.

It is worth noting that lateral fracture becomes particularly important in wear processes where lateral crack break-out combined radial cracks can lead to substantial material removal. In general, lateral break-out in the current work was a rare occurrence, even though some lateral break-out takes place as shown in Figure 4.13, both for unimplanted and implanted sapphire. This observation is different from the case of silicon [Burnett and Page, 1984], in which ion implantation considerably reduced the lateral break-out and surface-lifting, due to sub-surface lateral cracks. However, Burnett and Page [1984] observed the extent and number of the lateral cracks underneath the surface is reduced after implantation by using reflected polarized light micrography. Again, stresses induced by implantation are presumed to be responsible for the lateral crack retardation.



(a) control



(b) $4 \times 10^{16} \text{ Ar}^+ \text{ cm}^{-2}$

Figure 4.13 SEM observation on the trace of lateral crack propagation.

4.4 *Nano-Indentation Hardness*

The variation of nano-indentation hardness on sapphire fibers with implantation doses of 2×10^{16} , $2 \times 10^{17} \text{ Mg}^+ \text{ cm}^{-2}$ is shown in Figure 4.14. Compared with unimplanted fiber, nano-indentation hardness reaches a maximum value at the dose of $2 \times 10^{16} \text{ Mg}^+ \text{ cm}^{-2}$. However, the hardness at dose of $2 \times 10^{17} \text{ Mg}^+ \text{ cm}^{-2}$ is approximately equal to that at unimplanted state. In the preceding section, it has been presented that the compressive stress induced by ion implantation monotonically increases with ion dose, in other words, the measured compressive stress at a dose of $2 \times 10^{17} \text{ Mg}^+ \text{ cm}^{-2}$ is 2.8 GPa, larger than the dose of $2 \times 10^{16} \text{ Mg}^+ \text{ cm}^{-2}$ (2 GPa). A question arises to why nano-indentation hardness reaches a maximum value in an intermediate compressive stress instead of at maximum compressive stress? For a better answer to the question, the characteristic bend strength corresponding to each implantation condition are also presented in Figure 4.14 for reference, which are the same data as in Figure 4.3. To some degree, the trend in hardness changes is consistent with the observed bend strength changes. As it is known, hardness measurement is associated with plastic deformation behavior at the ahead of indenter tip. Hardness is usually measured on the indenter's contact area left due to plastic flow after removal of load. Therefore, the extent of elastic-plastic and elastic recovery at the head of indenter influences the hardness measurement. In other words, irradiated surface properties are closely related to the hardness measurement. According to the model described in 2.3.1 [Burnett, 1985], Burnett and Page predicted that amorphization of surface should occur at doses over $1 \times 10^{17} \text{ ion cm}^{-2}$. Before the occurrence of amorphization, the irradiated surface is still crystalline but damaged. The production of defects such as vacancy clusters, dislocation loop and existence of compressive stress leads to surface hardening, as discussed in section 2.4.3.5. The production of an amorphous surface layer causes a surface compressive stress due to the volume change that accompanies the transformation. The deformation of amorphous phases occurs by viscous flow rather than by dislocation slip or cleavage fracture.

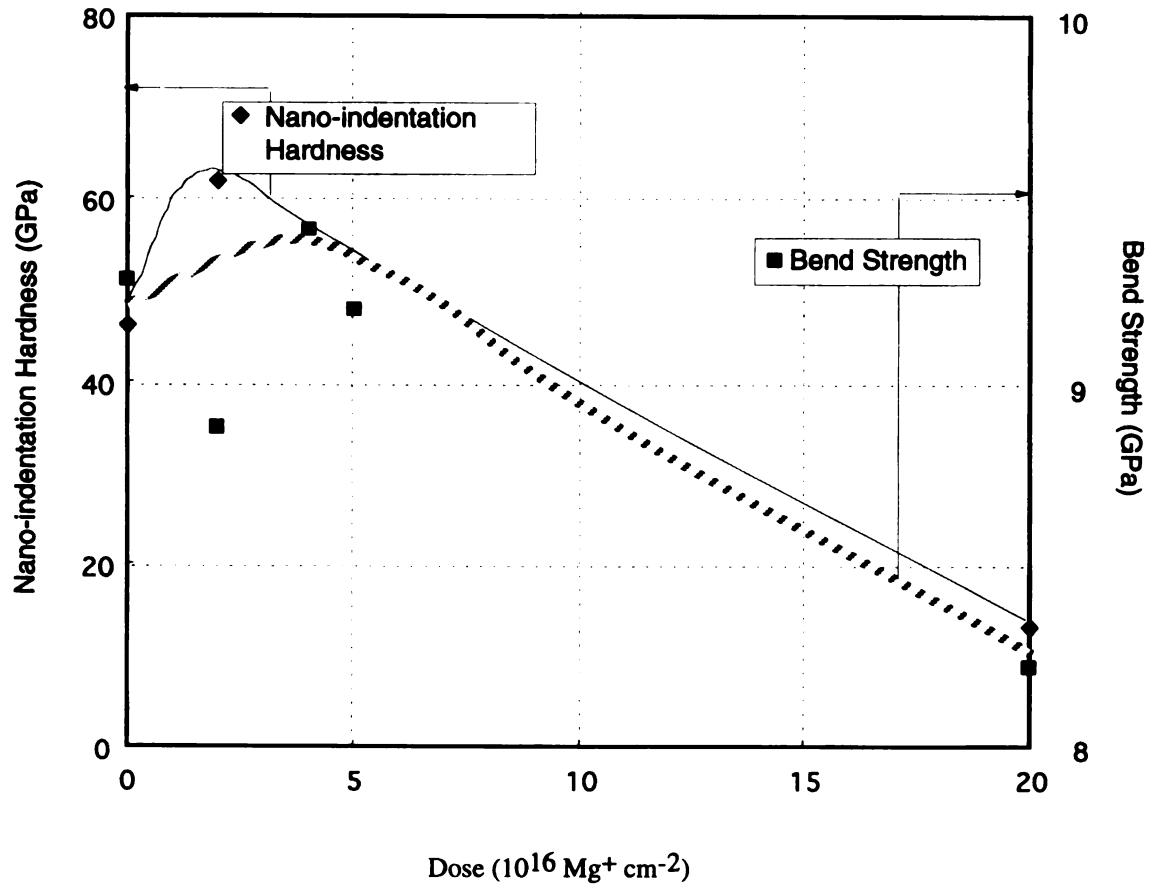


Figure 4.14 Nano-indentation hardness of sapphire fibers with ion implantation dose. Corresponding bend strength included for comparison.

However, TEM observations, discussed later in section 4.9.1, particularly in Figure 4.37, on the near-surface microstructure of sapphire fiber implanted with the highest dose of $2 \times 10^{17} \text{ Mg}^+ \text{ cm}^{-2}$ does not show amorphization within the implanted region. Due to TEM resolution, it does not exclude possible partial amorphization within the implanted zone, as observed by McHargue [1987]. Another possibility for the hardness behavior might arise from the fact that the penetration depth of nano-indentation exceeds the implanted zone thickness. The penetration depth in the case of $2 \times 10^{17} \text{ Mg}^+ \text{ cm}^{-2}$ is about 1100 nm while the whole implanted zone is 350 nm (as shown in Figure 4.37 later). The measured surface stress is an integrated surface stress over the implanted zone. It is unknown how the stress changes with ion distribution because the ion distribution inside the implanted zone is supposed to be Gaussian distribution as verified by many investigators by using Rutherford Backscattering techniques [Ohkubo, 1986; Hioki, 1985]). Beyond the implanted zone, it is not clear how the existence of compressive stress affects the indentation displacement.

In Figure 4.14, bend strength change with dose shows a similar trend as hardness does. The relationship between bend strength and compressive stress will be explored further in section 5.2.

4.5 *Annealing Effects*

It is known that ion implantation is a non-equilibrium process, which introduces massive foreign atoms into host substrate, thus causing lattice or crystalline damage. It has been shown that Mg^+ and Ar^+ implantation into sapphire fibers in the current study has only modest effects on their bend strength. But the retained strength of implanted fibers after abrasion is higher than that of unimplanted fibers. These characteristics are attributed to the introduction of compressive stress by ion implantation. Questions arise regarding the effects on the bend strength of sapphire fibers after implanted fibers undertake post-implantation treatment, because the microstructure created by the non-equilibrium

implantation process can be expected to change after heat treatment. In this section, the effects of annealing on the bend strength of sapphire fibers will be presented and discussed.

The fibers implanted with Mg^+ and Ar^+ , together with unimplanted fibers, were annealed in a vacuum environment for 2 hours. The annealing led to the disappearance of the violet coloration produced by implantation, indicating that color centers had undergone recombination reactions. Table 4.4 summarizes the bend strength for annealing temperatures ranging from 800°C to 1400°C . In general, bend strength decreases with increase of the annealing temperature as shown in Figure 4.15. For control fibers, the bend strength decreased 23 percent from 9.31 GPa for the as-received condition to 7.15 GPa for fibers annealed at 1400°C . Over the same temperature range, the strength decrease was about 21 percent for $5 \times 10^{16} \text{ Mg}^+/\text{cm}^2$ implanted fibers, and 28 percent decrease for $2 \times 10^{17} \text{ Mg}^+/\text{cm}^2$ implanted fibers. Annealing of Ar^+ implanted fibers showed similar behavior. Figures 4.16 and 4.17 show Weibull plots for unimplanted and implanted fibers after annealing 2 hours at 1200°C vacuum environment, respectively. These figures show that all Weibull curves for both Mg^+ and Ar^+ have shifted to the low bound of 95 percent confidence interval of as-received bend strength, even for high dose implantation case ($2 \times 10^{17} \text{ Mg}^+$). Furthermore, comparing Figure 4.1 with Figure 4.16, or Figure 4.2 with Figure 4.17, one can see that the only change between them is that the Weibull curves of annealed fibers shifts to the left, i.e., bend strength is reduced.

In comparison, Figure 4.18 shows the Weibull plot of bend strength for Mg^+ implanted fibers annealed in air. The bend strength of as-received fiber decreases about 10 percent from 9.31 GPa at room temperature to 8.34 GPa at 1000°C . The decrease is about 36 percent for $2 \times 10^{17} \text{ Mg}^+ \text{ cm}^{-2}$ implanted fibers (bend strength decreases from 8.31 GPa at room temperature to 5.23 GPa after annealed in air environment). Annealing in air environment is more detrimental to the retained strength than a vacuum environment, and that more prior irradiation causes a greater reduction in strength.

Table 4.4 Characteristic Bend Strength of Sapphire Fibers at Different Annealing Temperature (GPa)

Temperature	25°C	800°C	1000°C	1200°C	1400°C
0	9.31	8.61	8.41	7.01	7.15
$2 \times 10^{16} \text{Mg}^+$	8.87	8.41	8.41	8.10	8.11
$4 \times 10^{16} \text{Mg}^+$	9.47	8.30	7.82	7.37	6.25
$5 \times 10^{16} \text{Mg}^+$	9.26	8.66	8.19	7.01	7.36
$7 \times 10^{16} \text{Mg}^+$	8.92	8.35	7.22	6.08	6.93
$2 \times 10^{17} \text{Mg}^+$	8.21	7.46	6.60	6.19	5.92
$1 \times 10^{16} \text{Ar}^+$	9.15			6.94	
$2 \times 10^{16} \text{Ar}^+$	8.34			5.63	
$4 \times 10^{16} \text{Ar}^+$	9.24			6.19	

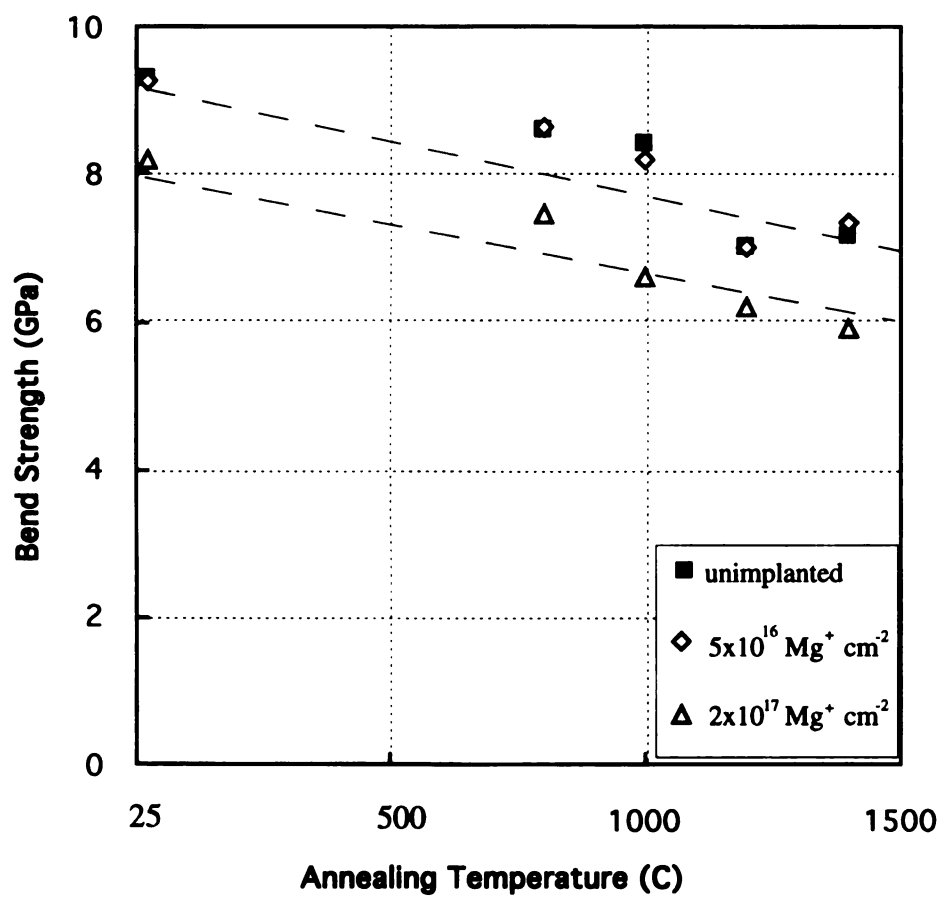


Figure 4.15 Effects of annealing temperatures on the bend strength of implanted fibers. Two dashed line is the curve fit which indicates that three point bend strength of sapphire fibers decreases with increase of annealing temperature.

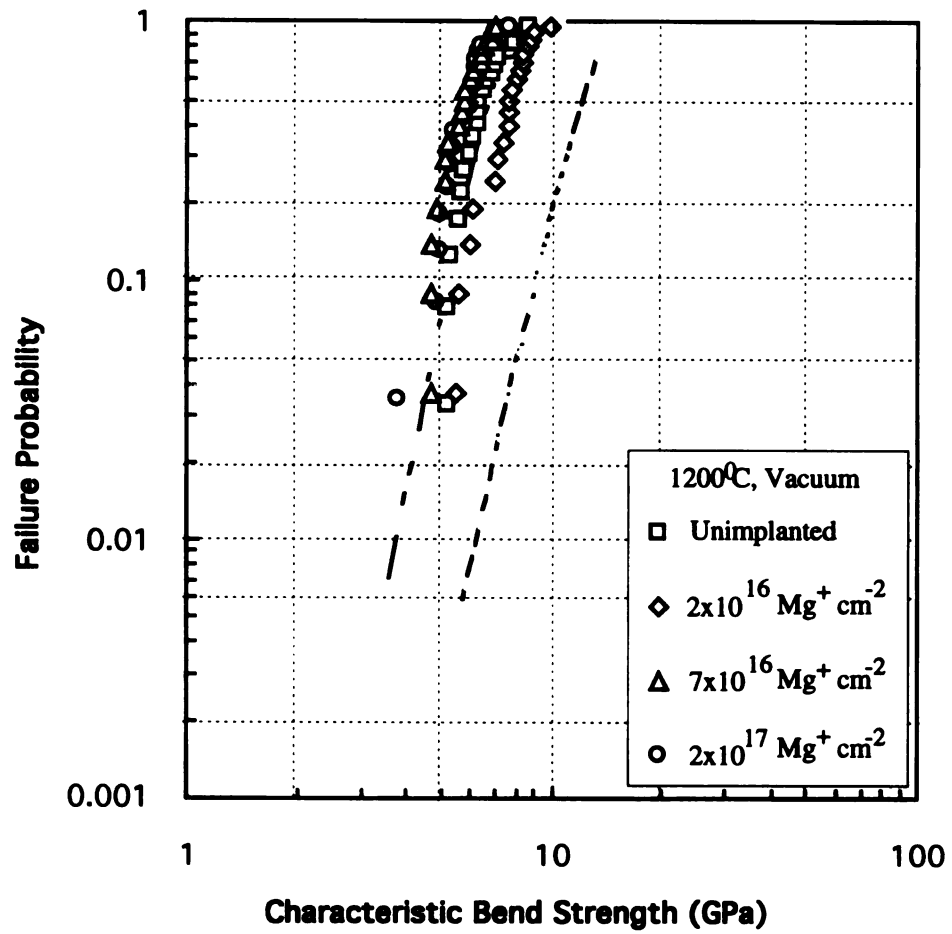


Figure 4.16 Weibull plot of bend strength for Mg⁺ implanted sapphire fibers at annealing temperature of 1200 °C for 2 hours. The two dashed lines represent 95 percent confidence band of bend strength for unimplanted sapphire fibers at room temperature.

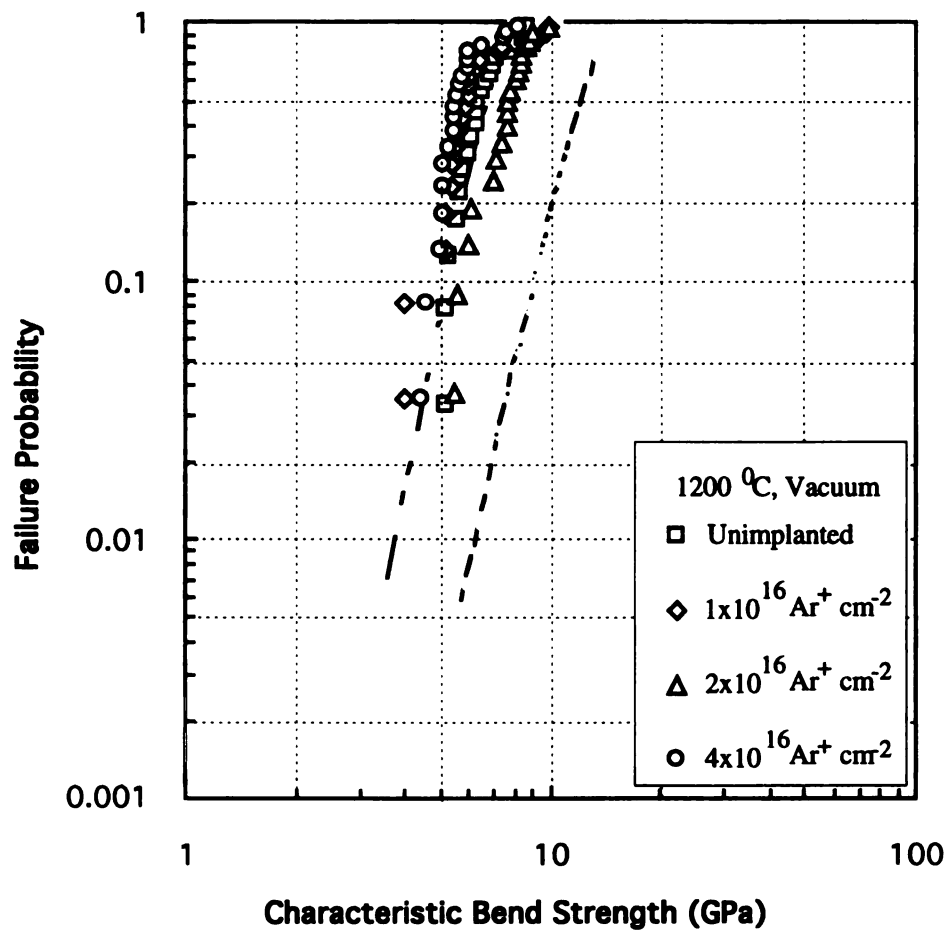


Figure 4.17 Weibull plot of bend strength for Ar⁺ implanted sapphire fibers at annealing temperature of 1200 °C for 2 hours. The two dashed lines represent 95 percent confidence band of bend strength for unimplanted sapphire fibers at room temperature.

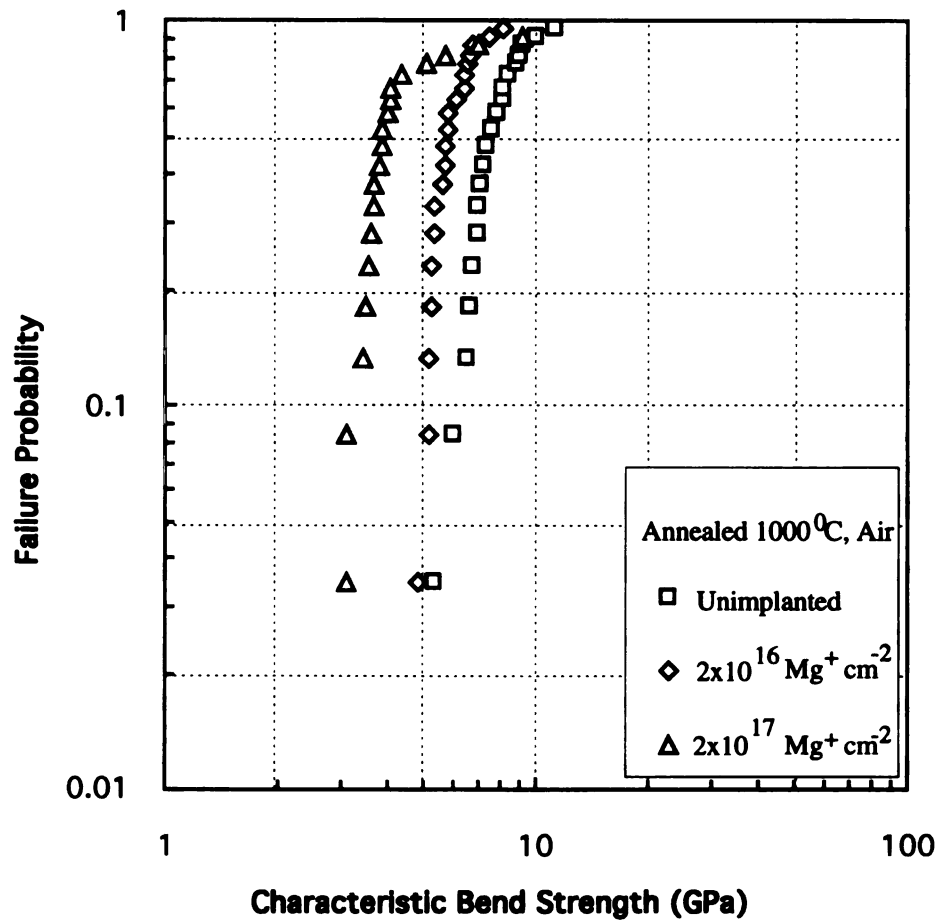


Figure 4.18 Weibull plot of comparison of bend strength for Mg^+ implanted sapphire fibers annealing at 1000 °C for 2 hours in air environment.

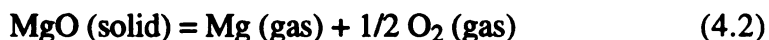
It is expected that thermal diffusion or segregation occurs for the impurity atoms induced by ion implantation during annealing. The impurity atoms which come to rest within the implanted region are mobile once the thermal driving force is available.

Studies of Mg implanted sapphire after thermal annealing revealed that Mg may segregate to the [0001] basal plane, or diffuse deeply into bulk material, or volatilize from the surface, depending strongly upon the annealing environment [Baik, 1985, 1986; Mukhopadhyay, 1988; Jardine, 1987]. Annealing in air led to surface enrichment of Mg [Baik, 1985, 1986]. The surface concentration of magnesium was found to decrease monotonically with increasing temperature above 1300°C. Below 1300°C, the surface concentration of magnesium was found to be very non-uniform [Baik, 1985]. In addition, SIMS analysis indicates that the concentration of Mg decreases dramatically with depth for air annealed sapphire which was implanted with Mg [Jardine, 1987]. Annealing in air probably allows oxygen to diffuse into the implanted sapphire to compensate charge imbalances created by the diffusing-out Mg ions. By using low-energy electron diffraction, Baik, *et al* [1985] showed the presence of two-dimensional ordered overlayer structures in which Mg is present in form of small “islands”, suggesting that Mg ions form a substitutional solution with host Al in the Al_2O_3 surface. In the current study, no attempts were made to relate the formation of the substitutional solution with surface topography change. However, based on the fact that bend strength of $2 \times 10^{17} \text{ Mg}^+$ implanted sapphire fibers after annealing in air environment decreased to a larger extent than control fibers, it is postulated that the formation of the substitutional solution might alter the surface topography, and further deteriorate the surface uniformity.

Hioki *et al* [1985] verified that a spinel compound NiAl_2O_4 was formed on the Ni implanted sapphire surface after the sample was annealed in air at 1000 °C. This thin film spinel compound affects the flexural strength because thermal properties of the thin film are different from the underlying bulk material. In this case, the thermal expansion coefficient

of NiAl_2O_4 is 6% smaller than that of $\alpha\text{-Al}_2\text{O}_3$, and results in a residual surface compressive stress while the specimen is cooled down to room temperature.

Previous research [Mukhopadhyay: 1988] on Mg^+ implanted sapphire¹ by Auger electron spectroscopy has shown that no trace of Mg on the surface was found after the implanted samples were annealed under vacuum environment. Instead, Ca was found to segregate strongly to the surface although the bulk concentration of Ca was known to be very low. The absence of a magnesium signal was attributed to a rapid loss of surface Mg through a vaporization process which increases with decreasing partial pressure of O_2 . The decomposition reaction of MgO is:



The vaporization flux of magnesium will be proportional to the equilibrium vapor pressure of the Mg-containing species.

In summary, Mg segregation to the surface and formation of precipitates after annealing in air, as well as Ca segregation to the surface during annealing in vacuum, and degradation of bend strength is not fully understood at this time. It is reasonable to postulate, based on previous research [Mukhopadhyay: 1988; Baik: 1985, 1986] and the current bend strength measurements, that any reaction of Mg or Ca with host Al_2O_3 results in change on the surface uniformity which in turn affects fracture behaviors.

4.6 *Sapphire Fiber Strength Degradation During Composite Fabrication*

The following section describes fiber strength degradation after etching from $\text{NiAl}/\text{Al}_2\text{O}_3$ composite, and discusses the efficiency of ion implantation on protection of sapphire fiber during the composite fabrication process. As described in section 3.7,

¹ Total impurity in the sapphire was 40 ppm. The samples were implanted with 200 keV Mg^+ ions to a dose of 1×10^{17} to 2×10^{17} ions/cm². The samples were annealed at vacuum (10^{-6} to 10^{-7} Pa), temperature (1300 °C) for 2 hours.

NiAl/Al₂O₃ composites were fabricated, and then sapphire fibers were extracted from the composite after hot-press consolidation, and, finally, bend strength was obtained by three point bend tests on the etched fibers.

The extracted fibers from the NiAl composite with as-received fibers had serious strength degradation, which decreased from 9.31 GPa to 3.36 GPa, as shown in Figure 4.19. In comparison, the bend strength of extracted fibers from the NiAl composite with implanted fibers also showed degradation to some degree, exhibiting residual strength slightly higher than as-received fibers, as shown in Figures 4.20. The average characteristic bend strength for extracted fibers from the NiAl/implanted fiber composite (both Mg⁺ and Ar⁺) is as follows: for Mg implanted fiber, the retained strength increased from 3.33 to 4.51 GPa; for Ar implanted fiber, the retained strength from 4.13 to 5.35 GPa. However, this retained strength is substantially lower than the strength before fabrication (8.56 GPa for 2×10^{16} Mg⁺ cm⁻², 8.34 GPa for 2×10^{16} Ar⁺ cm⁻²), and lower than the strength after annealing (8.1 GPa for 2×10^{16} Mg⁺ cm⁻², 5.63 GPa for 2×10^{16} Ar⁺ cm⁻², after vacuum annealing at 1200 °C).

The percentage of fiber breakage occurring during composite fabrication is shown in Figure 4.21. The majority of fibers etched from a 25 mm long NiAl/Al₂O₃ plate fabricated by foil/fiber/foil technique were less than 4 mm in length, accounting for over 80 percent of the extracted fibers. Unimplanted and implanted fibers both have the same general trend of fragmentation.

The complicated factors associated with the fabrication process can also be demonstrated by comparison of bend strength among control, abraded and extracted fibers. Figure 4.22 compares the bend strength variation for unimplanted and Mg implanted fibers in conditions of as-received, abraded 60 minutes and extracted from NiAl/Al₂O₃ composite, respectively. For unimplanted fibers, bend strength decreases in order from 9.31 GPa at as-received condition, to 4.51 GPa after abrasion for 60 minutes, and to 3.36 GPa after extraction from the composite. Similarly, for Mg implanted fibers, the strength decreases

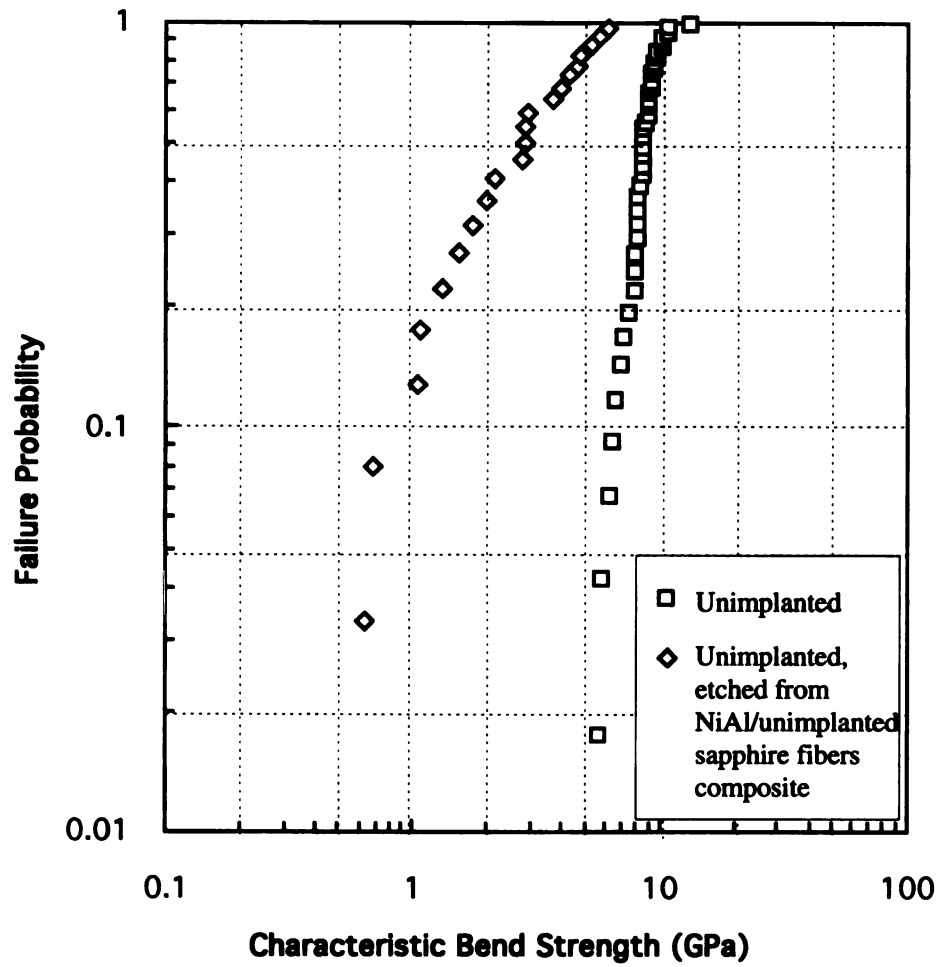


Figure 4.19 Comparison of bend strength Weibull plots for unimplanted sapphire fibers, which include unimplanted sapphire fibers as reference and etched unimplanted fibers from NiAl/unimplanted sapphire fiber composite.

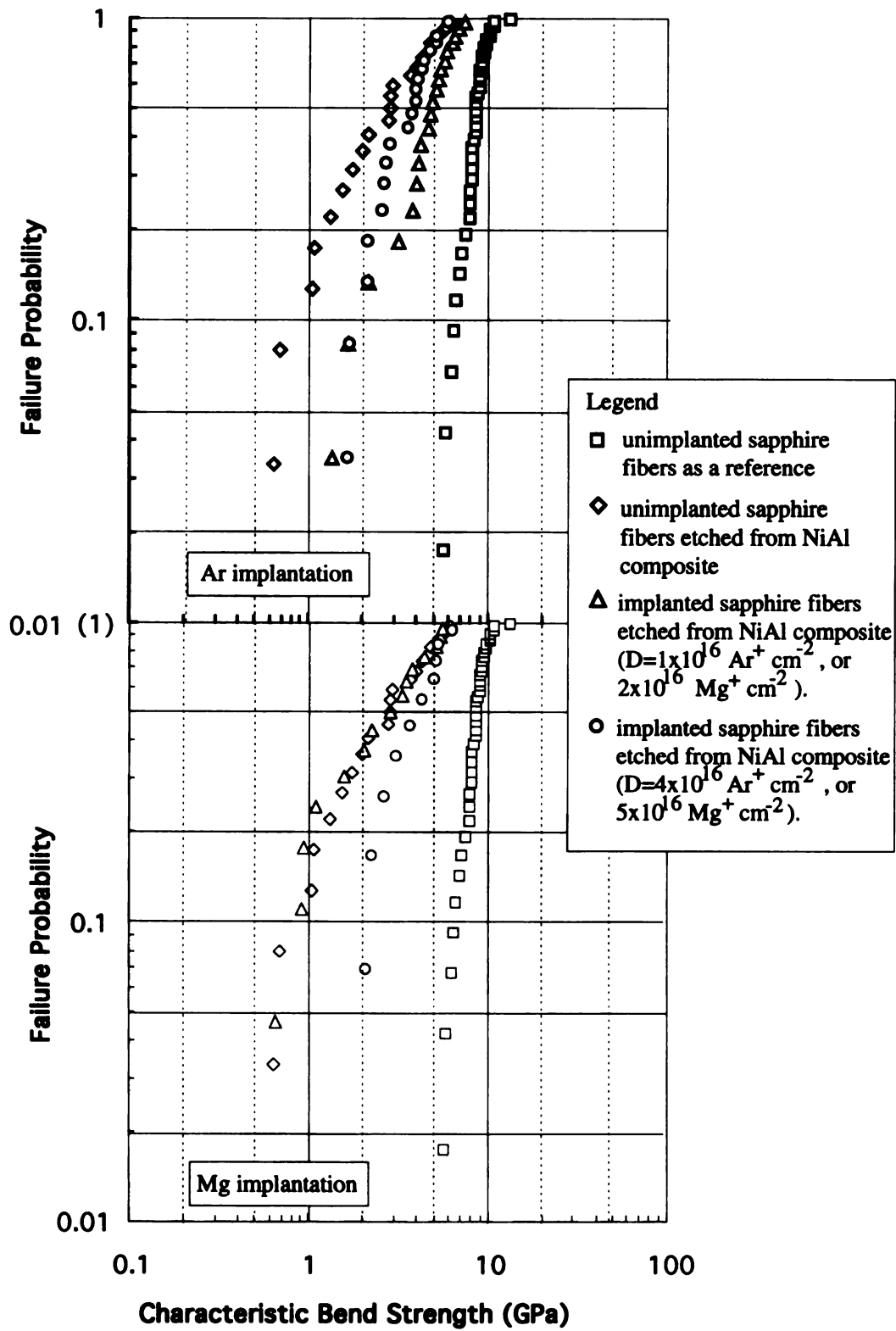


Figure 4.20 Comparison of bend strength Weibull plots for implanted sapphire fibers etched from NiAl/sapphire fibers composite. Bend strength for both unimplanted sapphire fibers and unimplanted sapphire fibers etched from NiAl/sapphire fibers composite are also included.

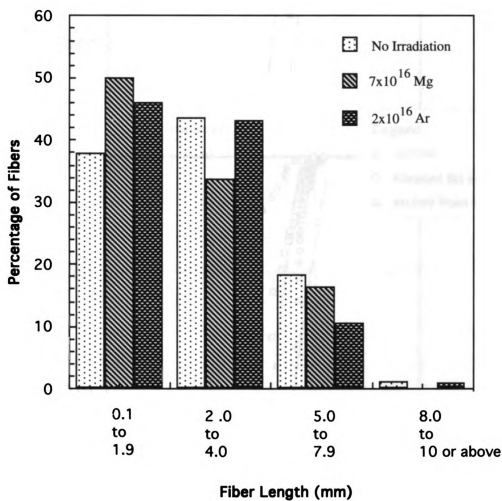


Figure 4.21 Fragmentation of sapphire fibers etched from NiAl/Al₂O₃ composite.

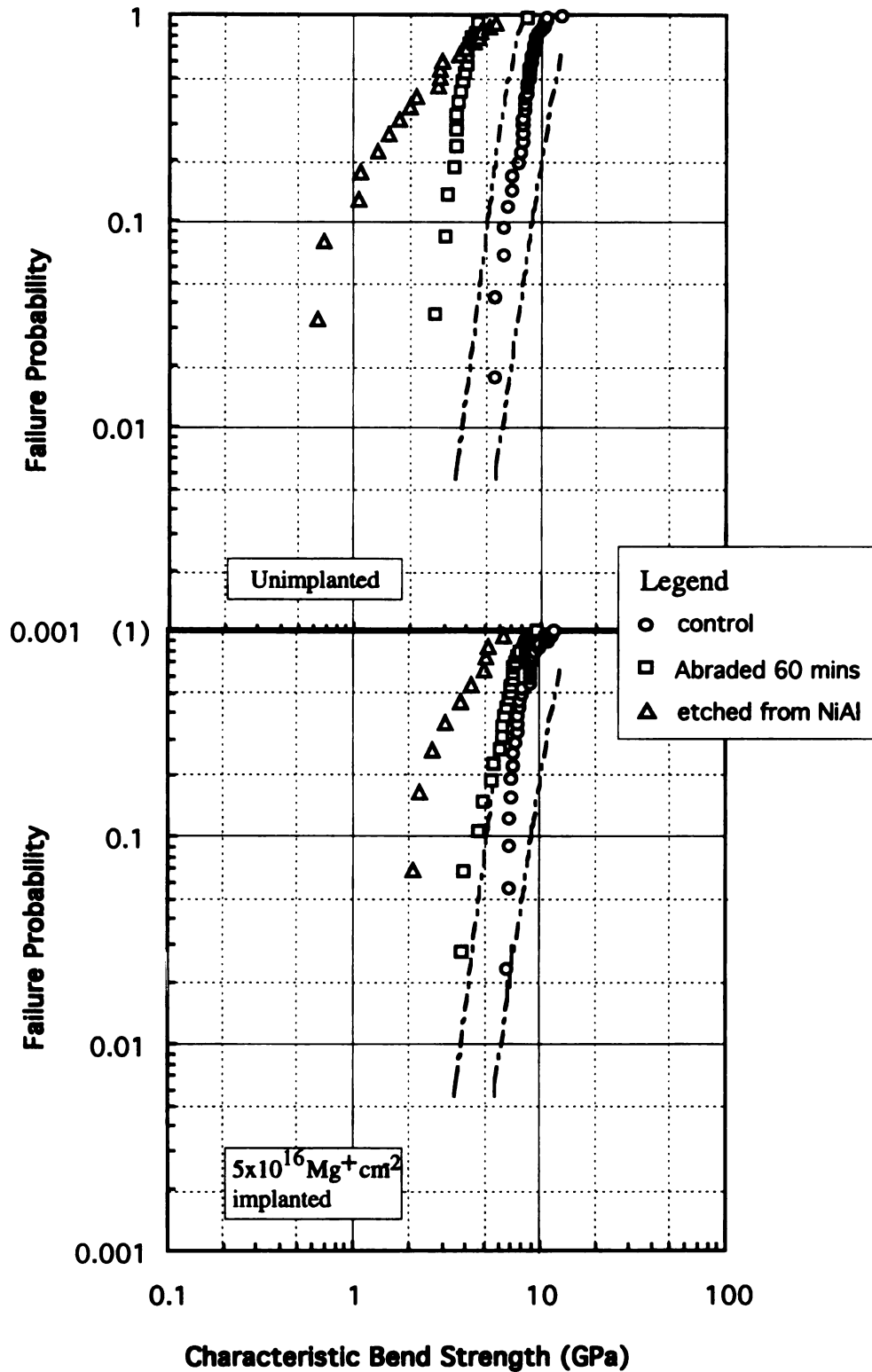


Figure 4.22 Effects of different processes on the bend strength Weibull plots for both unimplanted and Mg implanted sapphire fibers. Two dashed lines represent 95 percent confidence band of bend strength for unimplanted sapphire fibers at room temperature. The top figure is for unimplanted sapphire fibers, the bottom is for implanted sapphire fibers.

from 9.26 GPa at as-implanted condition, to 7.58 GPa after abrasion for 60 minutes, and to 4.51 GPa after extraction from the composite. This clearly shows that the fabrication process leads to severe strength degradation on sapphire fibers. This process involves not only possible abrasion and point load effects, but also fiber-matrix reactions and other elevated temperature effects.

Three possible mechanisms can contribute to the strength loss. The first mechanism should be related to fabrication temperature. In the preceding section, annealing at fabrication temperature led to fiber strength degradation for both as-received and implanted cases. The reason is that impurity segregation to the surface during annealing could alter the fiber surface uniformity. During the fabrication process, the NiAl/sapphire fiber composite was held at constant temperature of 1523 K for 3 hours. Therefore, it is expected that impurity segregation to surface would take place. The second mechanism could be related to the role of hot pressing. During the fabrication operation, matrix could exert point loads on the sapphire fibers. The extracted fiber fragmentation strongly suggests that during fabrication process, fibers are subjected to stress, though it is also possible that a circumferential compressive stress around the fiber arises from the contraction due to mismatch of thermal expansion coefficient between fiber and matrix during fabrication cooling process. However, Draper *et al* [1994] reported that the strength of the fibers etched from a powder cloth composite was nearly the same as the strength of fibers sputter-coated with matrix and exposed to elevated temperature. They concluded that the contribution from the hot press or HIP process might not be a major factor in the degradation of Al_2O_3 fiber strength, and that the effect of the pressure from hot pressing may cause a degradation in fiber strength if all contributions from matrix reaction were eliminated. The third possible mechanism for strength loss is related to the fiber-matrix reaction. Sapphire is thermodynamically stable in NiAl at 1523 K. However, chemical reaction on sapphire during fabrication of NiAl/sapphire composite may take place. Further SEM observations on the surface topography will be presented in the next section.

4.7 *Fiber Surface Morphology*

A high magnification SEM morphology of a washed as-received sapphire fiber is shown in Figure 4.23, which demonstrates a very smooth character. Few flaws or pores were observed. This is in contrast to another investigation [Davis, 1995], in which flaws were observed in the as-received fibers that were believed to be associated with porosity developing during fiber growth. The SEM morphology of an as-received sapphire fiber subjected to the extraction chemical solution, shown in Figure 4.24, exhibits the same surface features as shown in Figure 4.23. The absence of pitting or surface morphology alternations indicate that the fiber extraction process has no effect on the fiber.

Figure 4.25 is a low magnification SEM morphology of sapphire fiber etched from NiAl/Al₂O₃ composite. In Figure 4.25(a) there are impurity particles adherent on the surface, ranging in size from approximately a few to 15 microns. These adherent particles are believed to come from the matrix. In contrast, the etched surface of $7 \times 10^{16} \text{ Mg}^+/\text{cm}^2$ implanted sapphire fiber shows different sized pore features, as shown in Figure 4.25(b). These pores evidently result from chemical reactions between fiber and matrix during composite fabrication process. These pores usually correlate with failure origins and account for the strength loss. Figure 4.26 is a high magnification SEM observation on etched Ar⁺ implanted fiber surface along with extracted unimplanted fiber surface. One still can see many residues attached on the surface.

The residues in Figure 4.25 were analyzed by EDS as shown in Figure 27. The EDS results on the residues on control fibers show that a small amount of Ni exists as a compound component in which Al and O are major compound elements. On the $7 \times 10^{16} \text{ Mg}^+ \text{ cm}^{-2}$ implanted fibers surface, Mg was also found. These results are similar to that reported by Draper [1994]. It is likely that the reaction with the matrix resulted in pores or adherent particles on the fiber surface. The strength of sapphire fiber is dependent upon surface roughness. If the surface roughening due to the pores or adherent particles was

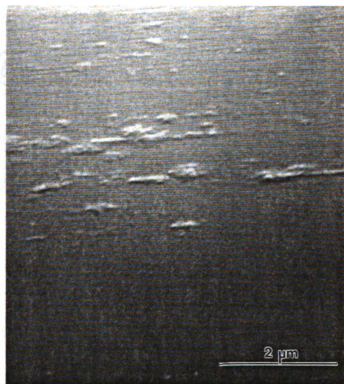


Figure 4.23 SEM observation on a clean as-received sapphire fiber surface.

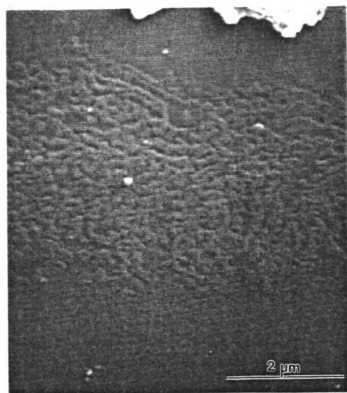
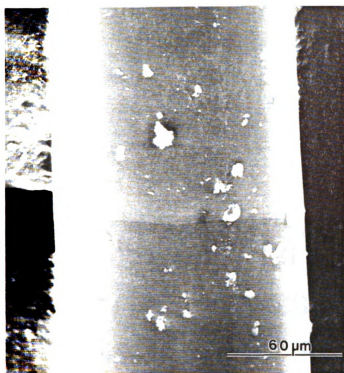


Figure 4.24 SEM observation on the surface of sapphire fiber subjected to chemical etch solution, which is composed of 50 % H_2O , 33 % HNO_3 and 17 % HCl (by volume).



(a) control fiber

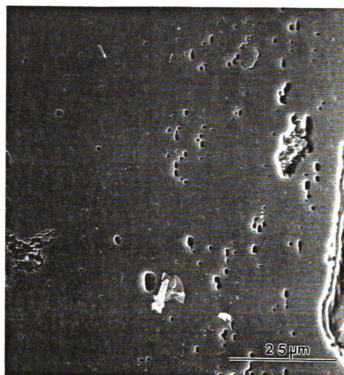
(b) $7 \times 10^{16} \text{ Mg}^+ \text{ cm}^{-2}$ implanted fiber

Figure 4.25 SEM observation on the surface of extracted fibers from $\text{NiAl}/\text{Al}_2\text{O}_3$ composite.



(a) control fiber

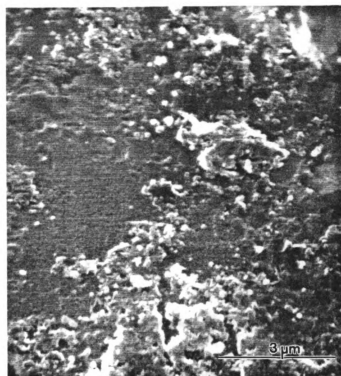
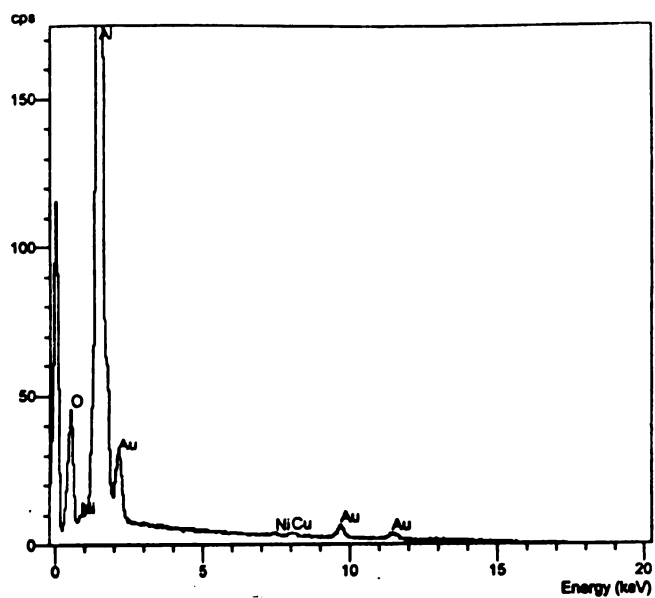
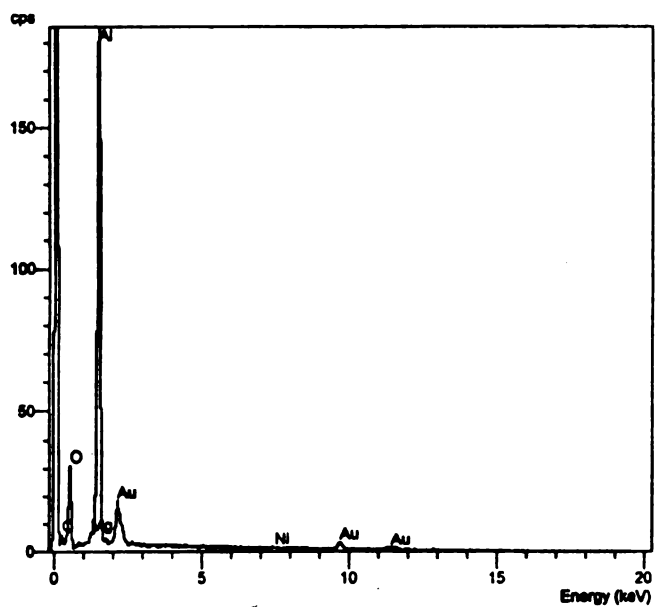
(b) $1 \times 10^{16} \text{ Ar}^+ \text{ cm}^{-2}$ implanted fiber

Figure 4.26 High magnification SEM observation on the surface of extracted fibers from NiAl/Al₂O₃ composite.



(a)



(b)

Figure 4.27 EDS composition analysis on the residues shown in Figure 4.25. (a) extracted unimplanted fibers; (b) extracted $7 \times 10^6 \text{ Mg}^+ \text{ cm}^{-2}$ implanted fibers.

more severe than the pre-existing flaws, fiber strength was reduced.

Upon heat treatment, the fiber surface morphology was also found to be strongly influenced by diffusion effects. The surface morphology of an etched sapphire fiber processed for 3 hours at 1523 K and with an applied stress of 5 MPa is shown in Figure 4.28. There are thermally grooved grain boundary imprints on the surface and small pores were sometimes associated with these ridges. These ridges may arise from matrix sintering to the fiber, and are diffusion-related phenomena which is driven by the reduction of grain boundary and surface energies. It is believed that any polycrystalline material will eventually result in ridges on the fibers' surface given enough time at a high enough temperature. Since the ridges extend to outward from the surface, the strength loss due to ridges may not be as severe as with the other types of flaws.

In principle, NiAl is thermodynamically compatible with Al_2O_3 . However, from the SEM observations on the fibers extracted from NiAl, as shown in Figure 4.26, it is evident that an interfacial chemical reaction took place between Al_2O_3 and NiAl. Since the fabrication process was carried out without a binder, the reaction must be associated with both the surface chemistry of the fiber, and the matrix composition. Table 5.1 lists the chemical composition of NiAl for different fabrication processes [Bowman, 1994]. (Note: we have the same source of materials from the NASA Lewis Research Center in Cleveland, OH). One possible reaction mechanism is that: Al_2O_3 reacts with carbon

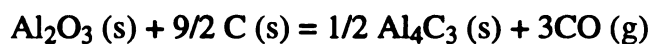
Table 4.5 Chemical Composition of NiAl

	Ni	Al	C	O	N
Starting Powder	50.3	49.7	0.011	0.046	0.006
Powder Cloth	50.2	49.8	0.101	0.211	0.005
Binderless	50.1	49.8	0.023	0.073	0.005



Figure 4.28 SEM observation of ridge on the surface of etched sapphire fiber from $\text{NiAl}/\text{Al}_2\text{O}_3$.

because Al_2O_3 and carbon can react to form a volatile aluminum suboxide at temperatures as low as 1100°C (Note: carbon contamination may also come from the vacuum furnace). The chemical reaction of interest and the standard free energies, ΔG^0 (J/mol), are as follows [Davis, 1995]:



$$\Delta G^0 = 1260904.5 - 575.5 T$$

where T is the temperature.

Bowman [1994] found that fibers extracted from powder-cloth processed material in which organic binder (poly(methyl methacrylate) PMMA) was used often had C-rich areas on the fiber surface. These C-rich areas contain residue left from incomplete volatilization of the binder materials; these deposits may act as fracture initiation sites and thus become detrimental to fiber strength.

4.8 *Fracture Surface Morphology*

In Figure 4.5, it has been shown that the fracture surface of the three point bend test on sapphire fiber demonstrates brittle fracture features, for both unimplanted and implanted cases. The crack initiation origin is almost invisible since the crack size is very small (as discussed in chapter V). Figure 4.29 further compares fracture surface features from low strength to high strength. It apparently shows brittle fracture features for both cases, i.e., no distinct difference on the fracture surface was observed.

However, for the sapphire fibers extracted from an NiAl/fiber composite, fracture surface features can be divided into two categories. The first group is the fracture surface of extracted fibers after subjecting to three point bend test, as shown in Figure 4.30, where brittle fracture features are characteristic of both extracted unimplanted and implanted fibers. The other is the fracture surface which result from the fiber fragmentation during

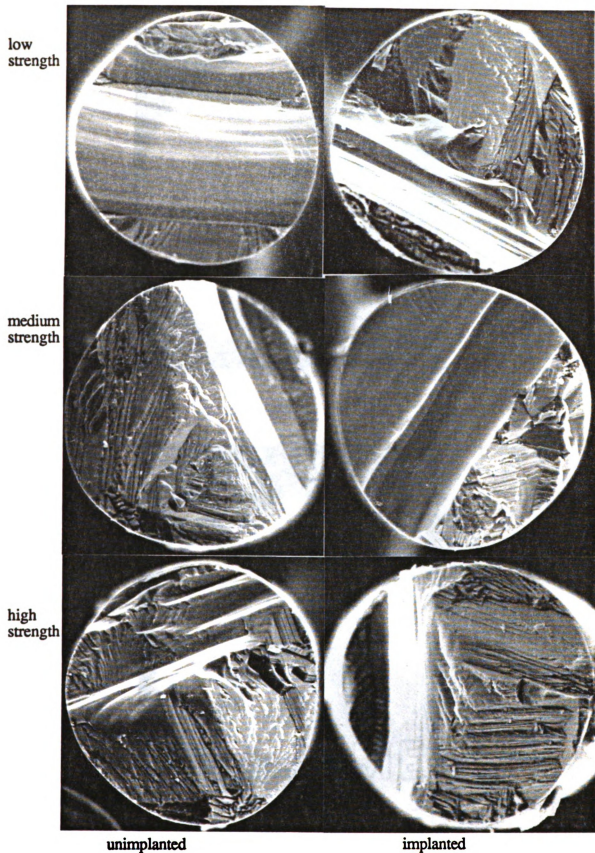
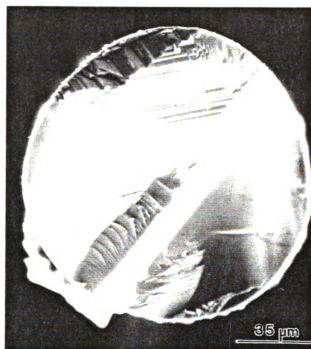


Figure 4.29 SEM observation on fracture surface variation with three point bend strength. Low, medium and high bend strength are 7.2, 8.5 and 9.5 GPa, respectively.



(a)



(b)

Figure 4.30 SEM observation on fracture surface feature of sapphire fibers which were subjected to three point bend test after they were extracted from $\text{NiAl}/\text{Al}_2\text{O}_3$ composite material. (a) unimplanted sapphire fibers; (b) $5 \times 10^{16} \text{ Mg}^- \text{ cm}^{-2}$ implanted sapphire fibers.

the fabrication process of NiAl/fibers composite, which is the so called “Naturally Fragmented” surface. Two subcategories about this kind of fracture surface can be classified. The first kind of feature is shown in Figure 4.31. The features are still in the nature of brittle fractures, similar to the feature in Figure 4.5, but shows more coarse characteristics for both implanted and unimplanted cases. This is probably related to the fabrication process, in which the fibers were subjected to 1523 K at stress of 5 MPa for 3 hours. During the process, creep or slow crack propagation may have taken place.

The second is the feature originating from internal pores, as shown in Figure 4.32. This fracture surface can be divided into four zones, i.e., ‘region 1’ is crack initiation zone where the internal pore acts as a stress concentrator; ‘region 2’ is crack propagation zone, where crack propagated in the radial direction and left behind a flat propagation path; ‘region 3’ is transition zone from crack propagation to brittleness fracture; Finally, ‘region 4’ is brittle fracture. The size of internal pores ranges from a few tenth micrometers to 1 micrometer. The internal pores are attributed to shrinkage voids inherent from the Saphikon fiber growth process (EDFG), in which sapphire fiber is drawn from the melt, and voids form by entrapment of liquid behind the solid surface. The void density in Saphikon fiber ranges from 33 to 105 pores/mm³ while size ranges from less than 0.1 microns to 2 microns.

Two possible fracture mechanisms might initiate the fracture behavior for the naturally fragmented fibers. In Figure 4.31, the surface flaw which is externally stressed is the control step for fiber fragmentation, similar to the fracture behavior in three point bending. Surface flaws may arise from original surface imperfection, or from abrasion during consolidation assembly, or surface faceting due to creep at consolidation temperature (because creep may be activated at this temperature). Once the crack is loaded, and the fracture criteria is reached, fracture occurs quickly. Brittle fracture dominates the process. This is why no crack initiation site was able to be detected from SEM observation.



(a)



(b)

Figure 4.31 SEM observation on fracture surface feature of sapphire fibers which fractured during consolidation process of NiAl/Al₂O₃ composite. (a) unimplanted sapphire fibers; (b) $5 \times 10^{16} \text{ Mg}^+ \text{ cm}^{-2}$ implanted sapphire fibers.

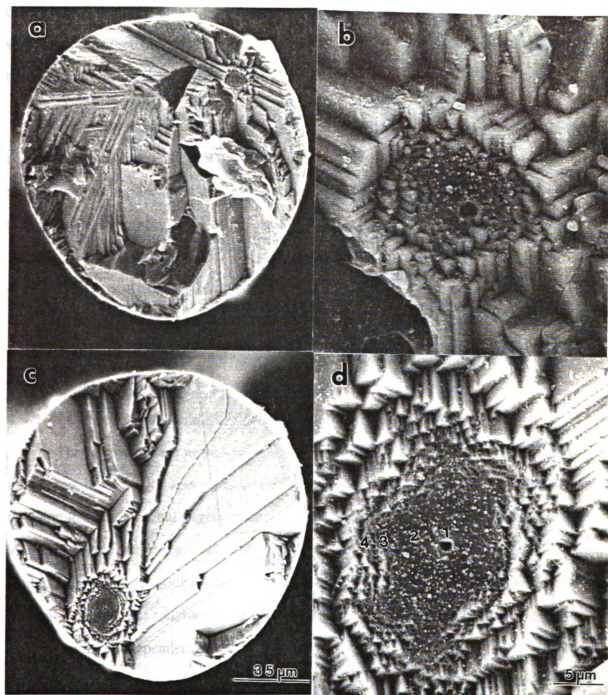


Figure 4.32 SEM observation on internal pores in sapphire fibers which fractured during consolidation process of $\text{NiAl}/\text{Al}_2\text{O}_3$ composite. (a) pore occurred in unimplanted sapphire fibers; (b) high magnification image of (a); (c) pore occurred in Mg implanted sapphire fibers; (d) high magnification image of (c). Region 1: pore site (crack initiation site); region 2: crack propagation; region 3: fracture mode transition; region 4: brittle fracture.

In Figure 4.32, failure resulting from creep of internal pores is the controlling mechanism. It is apparent that the crack due to internal pore has to propagate a certain distance until the stress state of crack reaches the fast fracture condition. Figure 4.32 shows that the creep deformation is about a few micrometers. Beyond the creep zone, brittle fracture features are distinct.

The control mechanism is dependent upon the competition between surface flaws and internal pore creep. Figure 4.33 shows that an internal pore initiates slow crack growth, and propagates to the surface edge. Failure resulting from internal pore creep dominates the process.

4.9 *TEM Investigation of Microstructure*

In this section, TEM observations on irradiated near-surface microstructure and relevant channeling effects during ion irradiation will be reported and discussed.

4.9.1 *TEM Observation and ECP Results*

The microstructure in the implanted region depends on several factors, including ion energy, ion dose, ion species and combinations of ion and target as well as implantation temperature. For ions and targets of relatively high atomic number and for relatively low ion beam energy, the energy lost by the ion is concentrated in a thermal spike which can lead to amorphization along a single ion cascade by the melting of a small region followed by rapid cooling. For relatively light atoms and high energies, amorphization follows an accumulation of independent single atomic displacements rather than a collective, thermal process. As proposed by Burnett and Page [1984], amorphization occurs after an ion dose reaches a certain threshold for a given ion implantation temperature, energies and combinations of ion and target. This is because at low temperature, recovery is suppressed and defects accumulate as the dose is increased. If recovery is sufficiently inhibited, a concentration of defects may be reached where the long-range order of the crystal lattice is

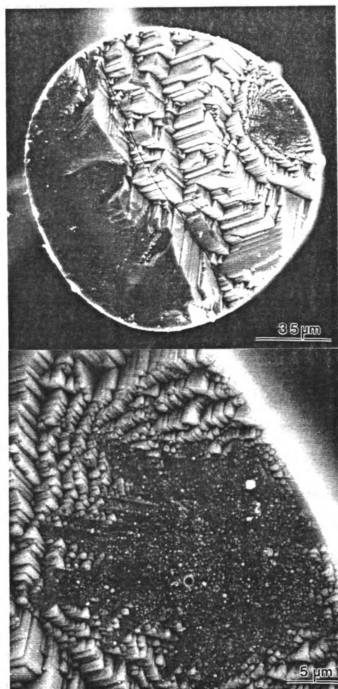


Figure 4.33 SEM observation on internal pores in sapphire fibers which occurred near edge. The fibers fractured during consolidation process of NiAl/Al₂O₃ composite.

destroyed and an amorphous state is produced. Before the amorphization dose, the implanted region is still crystalline but damaged.

Figure 4.34 shows the cross section TEM results for a sapphire fiber implanted with 175 keV Mg^+ of 7×10^{16} ion/cm² at room temperature. Because of limitations on the resolution of the TEM, the diffraction pattern actually overlays the implanted region and the substrate. From the present micrograph it can be seen that the surface region is still crystalline but there are many small networks or dark contrast features which are suspected of being small dislocation loops [McHargue, 1991] in the implanted region or in the buried layer of incident ion species.

There are four different regions in the implanted zone, i.e., free surface; near-surface region which is about 40 nm beneath the free surface, and is free of visible loops or networks but contains many small (~ 2 nm) features which exhibit contrast consistent with that of voids; the buried layer which is 200 nm to 400 nm below the near-surface region; and finally, the un-damaged fiber interior.

The characterization can be seen more clearly in Figure 4.35, which shows the TEM cross section observation on the sapphire fiber implanted with 2×10^{17} Mg^+ /cm² at room temperature. The TEM photo was taken using a JOEL 2000FX in the Michigan Ion Beam Laboratory in Ann Arbor. The insert diffraction pattern of the buried layer clearly shows that this region at dose of 2×10^{17} Mg^+ /cm² is still crystalline but a more heavy density of dark contrast features are present. Figure 4.36 is a high magnification TEM observation of this buried layer. In this case, the width of near-surface is about 50 nm and the buried layer is about 350 nm.

Although Ar has very different chemical properties than Mg, comparison of the behavior of Ar and Mg implanted fiber shows little difference between two cases, from bend strength measurement to abrasion resistance, to TEM microstructure observation. Therefore it is suspected that the ballistic collision dominates the effects of implantation rather than the chemical effect for these two particular cases. Figure 4.37 is a TEM

observation on sapphire fiber implanted with $1 \times 10^{16} \text{ Ar}^+/\text{cm}^2$ at room temperature. Similar features as Figure 4.34 and 4.35 were observed. Figure 4.38 is a high magnification TEM observation on the implanted region. There is a high density of dark contrast features within the buried layer and no bubbles or macro-scale voids were visible. There is no evidence for the formation of amorphous zones in the buried layer region. In Figure 4.37, the near-surface is about 40 nm wide, and the buried layer is about 180 nm.

Microstructural change in the subsurface induced by ion implantation is a complicated phenomenon and depends upon many factors. McHargue [1989, 1991], Burnett and Page [1984] and Hioki [1986] have observed microstructure in sapphire implanted with different ions at a given implantation condition such as ion species, ion energy, substrate temperature, ion dose, and temperature. For instance, McHargue [1991] reported that the TEM microstructure of $\alpha\text{-Al}_2\text{O}_3$ implanted with $4 \times 10^{16} \text{ Zr}^+ \text{ cm}^{-2}$ (280 keV at room temperature), combined with RBS spectra, has following features: the region from the free surface to 40 nm is still crystalline but damaged; region between 40 to 100 nm is amorphous; the region below 100 nm is also crystalline, but there is a high density of defects. However, TEM investigation by Specht [1994] on sapphire substrate implanted with 160 keV at $4 \times 10^{16} \text{ Cr}^+ \text{ cm}^2$ and $1 \times 10^{17} \text{ Cr}^+ \text{ cm}^2$ at room temperature showed no evidence for the amorphous formation in the implanted region. The TEM features are similar to the current observations, i.e., near-surface is about 60 nm and the buried layer is about 170 nm. A mass of dark contrast features (which the author considered as an array of dislocation loops and networks) is present within the buried layer. Based on TEM observation, Specht suggested that sapphire samples implanted at room temperature exhibit a high amorphization threshold because a local equilibrium is established where vacancies and interstitial recombine at the same rate that are produced. For amorphization at such a high dose ($2 \times 10^{17} \text{ Cr}^+ \text{ cm}^{-2}$) in single crystal Al_2O_3 , Specht proposed that accumulation of defects may serve as a mechanism of amorphization. These defects come from high-

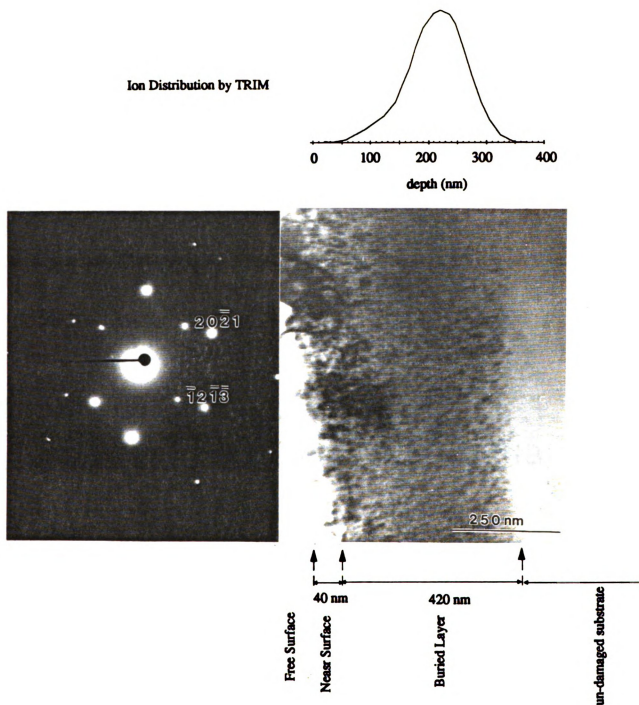


Figure 4.34 TEM observation on $7 \times 10^{16} \text{ Mg}^+ \text{ cm}^{-2}$ implanted sapphire fibers (insert is the diffraction pattern of the implanted zone). Near-surface region is defined as the region between free surface and the left side tail of implanted ions distribution; Buried layer is defined as the ion distribution region.

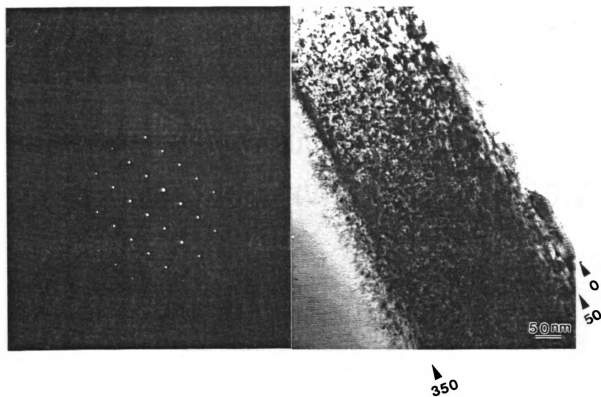


Figure 4.35 TEM observation on $2 \times 10^{17} \text{ Mg}^+ \text{ cm}^{-2}$ implanted sapphire fibers at room temperature. The diffraction pattern is taken from the inside of implanted zone.

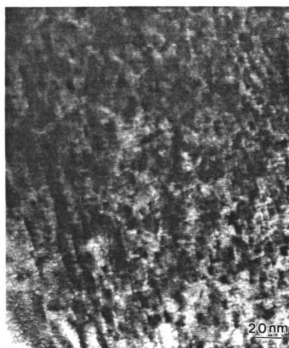


Figure 4.36 High magnification TEM observation on $2 \times 10^{17} \text{ Mg}^+ \text{ cm}^{-2}$ implanted zone.

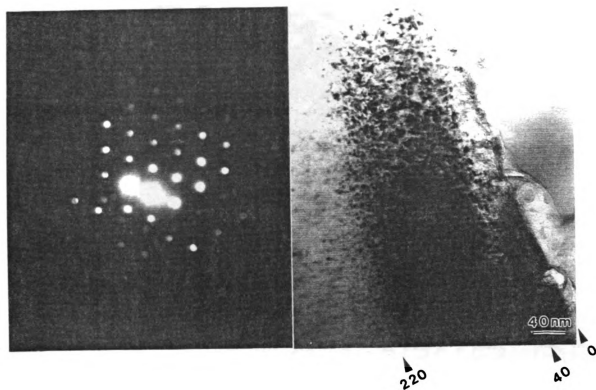


Figure 4.37 TEM observation on $1 \times 10^{16} \text{ Ar}^+ \text{ cm}^{-2}$ implanted sapphire fibers at room temperature. The diffraction pattern is taken from the inside of implanted zone.



Figure 4.38 High magnification TEM observation on $1 \times 10^{16} \text{ Ar}^+ \text{ cm}^{-2}$ implanted zone.

energy-transfer collisions which knock Al and O deeper into the crystal and leave a shallow vacancy and a deep interstitial.

Mechanical properties are closely related to subsurface microstructure. In the case of ion implantation, both the injection of the implanted ions and the creation of point defects cause a volume increase in the implanted region. Since the material is free to expand only in one direction (normal to the free surface) the constraints of the substrate to hold the lateral dimension constant produce a biaxial compressive stress in the implanted region. If the implantation produces residual compressive stress large enough, it will affect the mechanical properties by increasing the applied stress necessary to place the stressed surface into tension, thus reducing the probability of propagating a pre-existing flaw, or by affecting the crack tip stress fields.

Though the biaxial residual compressive stress is produced on the ion end of the range region, the stress distribution in the midrange is totally different. Specht [1994] found that the density¹ of Al₂O₃ in midrange decreases by 4% after Cr⁺ implantation while the volume expansion in the midrange was only ~0.2%. He attributed the density reduction of Al₂O₃ to high energy transfer collisions that knock Al and O atoms deep into the crystal and give rise to excess vacancies and deep interstitials. Therefore, it is expected that the stress state in the midrange about 40 nm from free surface is tensile. It seems controversial because compressive stress has been measured on the implanted surface by indentation technique. Keep in mind that the penetration depth during micro indentation is greater than the thickness of the midrange (40 nm), while in the nano-indentation measurement the average penetration depth is about 900 nm. This issue will be treated in further discussion.

Figure 4.39 shows an electronic channeling pattern comparison of unimplanted and implanted fibers, which illustrates the surface microstructure is still in crystalline. This observation was consistent with TEM observations, which confirms that there is no large scale amorphization formation on the implanted sapphire fiber surface.

¹ The density profile was measured by x-ray reflectivity. Detail can be referred to R. A. Cowley and T. W. Ryan, J. Phys., D 20 (1987) 61.

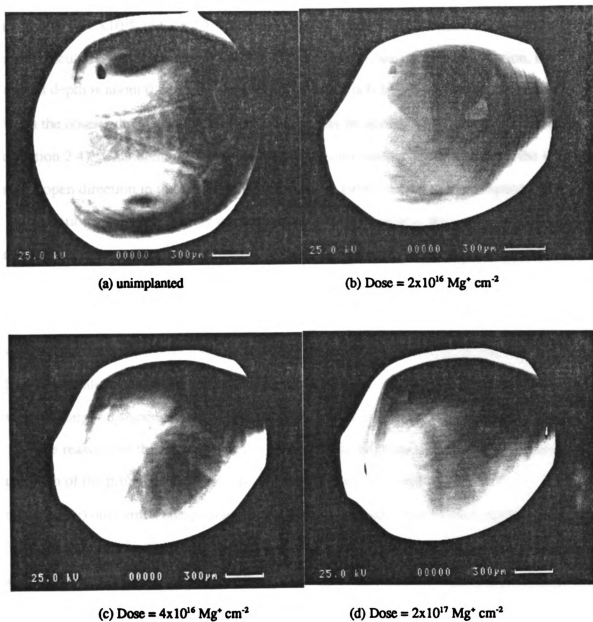


Figure 4.39 Electron channeling pattern for control and implanted sapphire fibers. The fiber axes is on the image plane.

4.9.2 *Channeling Effects*

It is interesting to note that the measured implantation depth (or range) is about 0.4 μm (in case of 7×10^{16} and $2 \times 10^{17} \text{ Mg}^+ \text{ cm}^{-2}$, 175 keV), which is about 33 % greater than the calculated depth (about 0.3 μm) by TRIM. For the case of Ar^+ implantation, the measured depth is about 0.22 μm while calculated depth is 0.14 μm . The discrepancy between the observed and calculated damage range may be attributed to a channeling effect (see section 2.4). Channeling is a process whereby atoms move over a distance in the solid along an open direction in the crystal structure [Carter: 1968]. In the current experiment, ion implantation was carried out by implanting ions perpendicular to the c-axis, or, in other words, the ion beam trajectory was parallel to the basal plane. In the hexagonal crystalline structures of Al_2O_3 , the c/a ratio is 2.73. The most open structure is in a direction perpendicular to the c-axis, or parallel to the basal plane. Ions moving along this crystallographic direction favorable to channeling can lose energy mainly by glancing collisions with atoms ringing the axis of motion. Therefore, channeled ions are able to move much larger distances than original knock-ons before coming to rest.

The reason that the channeling travel distance will be large is that since the distance of approach of the primary knock-ons and the lattice atoms are always large ($= 1/\sqrt{2}$ atomic spacing) only small energy transfer will occur, compared to a random sequence of collisions where, in a head on collision, all primary energy may be dissipated. On the other hand, channeled ions can materially reduce the anticipated defect production rate, particularly at high ion energies. These production of defects is dependent upon the interatomic potential. TRIM (version 90.05) doesn't take into account the probability of channeling. Therefore, the calculation results from TRIM can only represent a lower bound for penetration depth.

CHAPTER V

DISCUSSION

The results in the preceding section have shown that Mg^+ and Ar^+ implantation have little effect on the bend strength of unabraded sapphire fibers, and that there is an apparent compressive stress zone with a magnitude of 2 GPa in the implanted zone. Further TEM observations revealed that the implanted zone consists of different regions. The most striking results, the observed changes in bend strength retention during abrasion process, have been postulated to be associated with the implantation induced compressive stress. Based on these experimental results, this section will further explore this hypothesis, but first, the general nature of the accumulated lattice damage structures will be discussed.

5.1 *Chemical versus Ballistic Effects*

It may be recalled in section 2.1 that sapphire belongs to the space group R3C. The O^{2-} anions are hexagonal closed-packed, and the Al^{3+} cations occupy two-thirds of the available octahedral sites. The displacement energy was found to be 18 eV for aluminum and 72 eV for oxygen. It is possible to substitute isovalent or aliovalent impurities for Al^{3+} , but such impurities cannot be added without creating charge-compensating defects. The vacant octahedral sites are structural vacancies, and are ordered to balance the electrostatic force in the crystal [McHargue: 1991].

Since Mg^+ and Ar^+ have different chemical properties, the defects produced by each species may be supposed to be different. In the case of Mg, for example, a spinel phase, MgAl_2O_4 , may form when the MgO content exceeds the solubility. The spinel phase is normally found in form of precipitates. Figure 5.1 shows the pseudo-binary phase diagram of MgAl_2O_4 - Al_2O_3 system. As seen from the phase diagram, Mg solubility in Al_2O_3 is very limited. For instance, while the solubility reaches a maximum of 1% at the

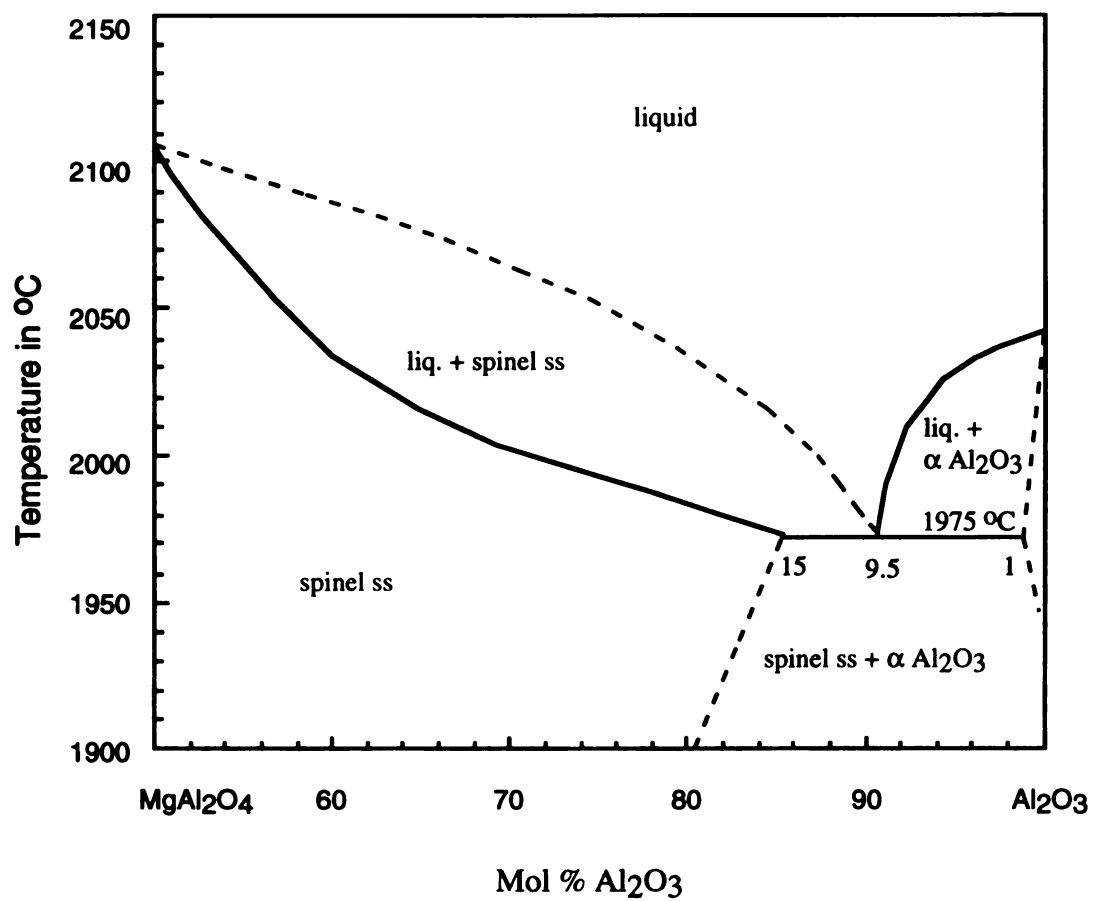
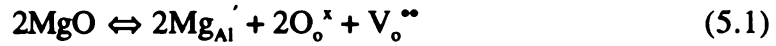


Figure 5.1 The system MgAl_2O_4 - Al_2O_3 . (After Dorre and Hubner: *Alumina*, Springer-Verlag Berlin, Heidelberg 1984.)

eutectic at 1975 °C, the solubility is 1400 ppm at 1830 °C, and only 300 ppm at 1630 °C [Dörre: 1984]. At room temperature, the solubility of Mg is thus effectively negligible.

Mg⁺ can be incorporated into sapphire as MgO in several different ways [Lagerlöf: 1983] as follows:



The Schottky reaction is



The anion Frenkel reaction is



and the cation Frenkel reaction is



Upon the implantation of Mg⁺ into sapphire, a large quantity of defects are produced due to energetic collisions between ions and the host crystal (non-equilibrium defects). For instance, the color of the fibers was observed to change from the original transparent to violet coloration in case of Mg⁺, and black in case of Ar⁺ implantation. These colorations come from oxygen vacancies containing trapped electrons (i.e., the F⁻ center (an oxygen vacancy containing one electron) and the F center (an oxygen vacancy containing two electrons) [McHargue, 1991].

These defects exist along with the formation of displacement spikes created by collisions between energetic ions and host crystal atoms. The displacement spike consists of multiple vacancies surrounded by interstitial atoms. It is the displacement spike that creates a damaged region where a structure differs from the original lattice. When the

displacement spike grows or collapses, defect clusters, or dislocation loops, or dislocation tangles and networks are created. McHargue [1991] reported that for $\alpha\text{-Al}_2\text{O}_3$ implanted with $2 \times 10^{16} \text{ Cr/cm}^2$ (280 keV) at room temperature contained a high density of dark contrast features identified as defect clusters, and further confirmed that these defect clusters were stoichiometric, interstitial dislocation loops. In the current TEM observation, similar dark contrast features were found within the implanted region for both Mg^+ and Ar^+ implantation. Further confirmation on the nature of these features is needed in future studies.

Ar^+ implanted into sapphire can exist in form of interstitials, defect clusters, or in form of gas within voids created by irradiation damage, depending upon implantation conditions. Gas in the latter form can develop into a bubble or blister. Hioki [1985] reported that blister formation in Al_2O_3 occurs only at high doses. For instance, the threshold dose of blister formation for 400 keV nitrogen implanted in Al_2O_3 at 300 K was about $2 \times 10^{17} \text{ N cm}^{-2}$. McHargue [1987] also reported that 30% of the sapphire (0001) surface was covered by blisters after implantation of $1 \times 10^{17} \text{ Ar}^+ \text{ cm}^{-2}$ (230 keV) at room temperature; in contrast, only 1% coverage consisting of smaller bubbles for a dose of $1 \times 10^{16} \text{ Ar}^+ \text{ cm}^{-2}$. Obviously, blistering is associated with the processes of inert gas evolution and accumulation, instead of chemical reactions with host crystal.

Hioki *et al* [1985] also compared the mass effects of ion implantation on the flexural strength of planar sapphire. They found that heavier ions were more effective at low doses in strengthening. Their results showed that at the dose of $5 \times 10^{15} \text{ ions cm}^{-2}$, 800 keV Ar^+ implantation at room temperature can increase the flexural strength by 60%, but only 20% for N^+ . They concluded that radiation damage due to ballistic collision entirely accounts for the observed strengthening effects.

In the current work, it was observed that after annealing, colorations due to ion implantation disappeared for both Mg^+ and Ar^+ implantation. This is because diffusion or aggregation of implanted ions occurs during annealing, thus causing annihilation of color

centers. Based on measurements of bend strength from Mg^+ and Ar^+ implanted sapphire fibers, and effects of abrasion and annealing on the retained bend strength, it was found that there was little difference between the effects of ion species on fiber properties, though Mg^+ and Ar^+ have very different chemical properties. Thus, ballistic interactions apparently dominate the effects of the implantation process, primarily, as will be shown, through creation of a special residual stress distribution within the implantation zone.

5.2 *Residual Surface Stress and Bend Strength*

Comparing the results of the bend strength for both unimplanted and implanted sapphire fiber, as shown in Figure 4.1 and Figure 4.2, ion implantation has little effect on bend strength behavior, even with the presumed existence of ~ 2 GPa surface compressive stress due to ion implantation. According to simple superposition principle, if there is a certain magnitude of compressive stress which exists in front of a pre-existing surface flaw, an increase in magnitude of external applied stress should be required to initiate tensile fracture the sample during a three-point bend test. The explanation of the question as to why the existence of compressive stress does not affect unabraded fiber bend strength can be rationalized by considering the nature of pre-existing flaws and the interaction of surface compressive stress with external stress states. The external stress states in three-point bend loading are different from the local stress states arising during the abrasion process.

Three point bend strength of unimplanted fibers

As shown in Figure 5.2(a), assume a single circular V-notch surface flaw with a length c existing as an initial flaw on a sapphire fiber. The diameter of the fiber is $2b$. After a bending moment, M , is applied to the fiber, the outermost layer of the fiber endures either maximum tensile stress or maximum compressive stress. Here, only tensile state is

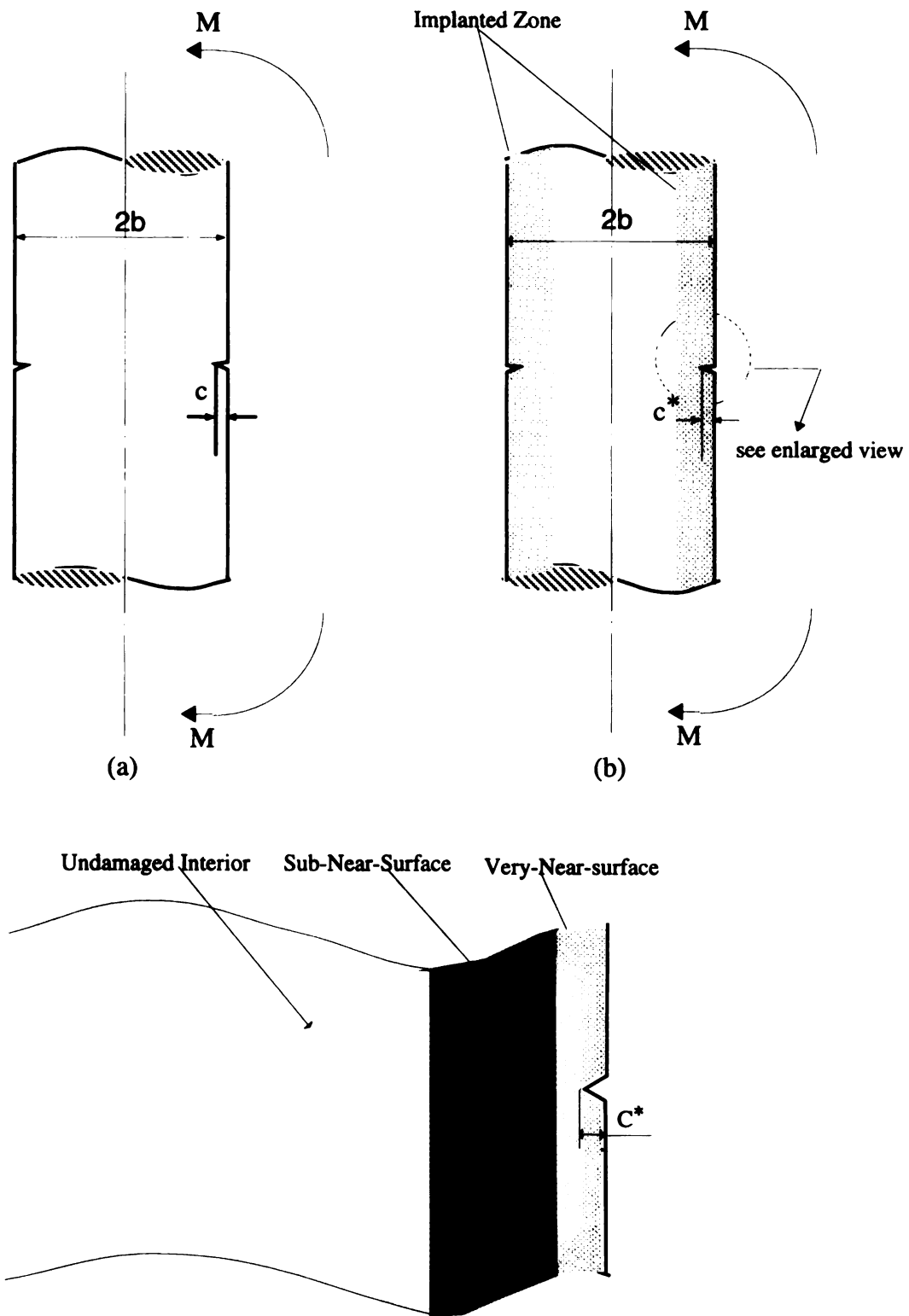
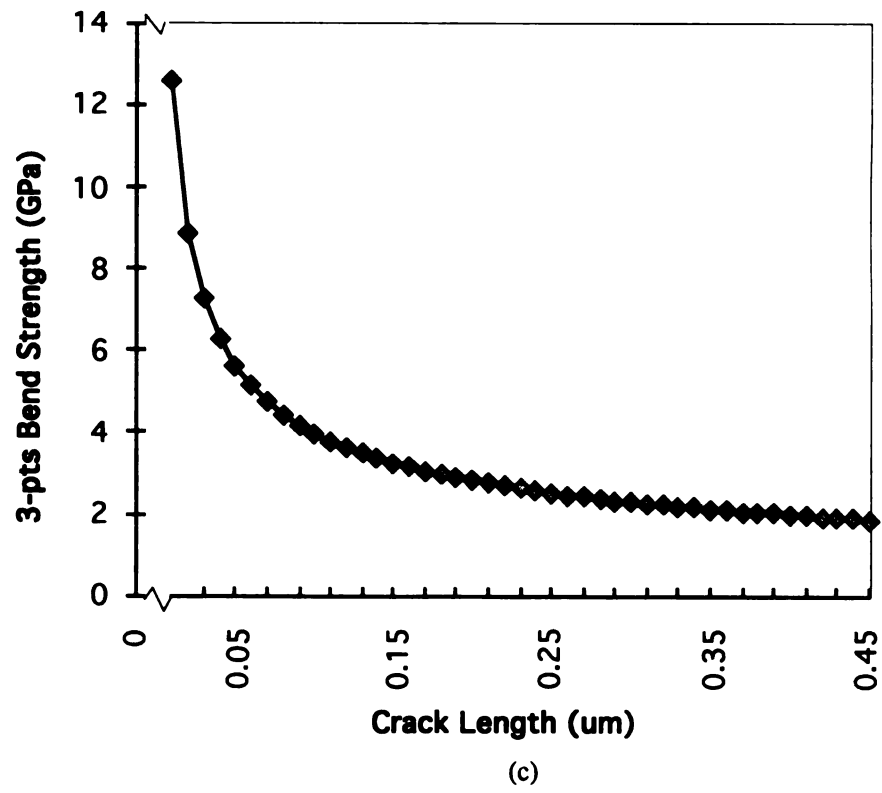


Figure 5.2 (a) Circular V-notch crack on unimplanted fiber surface; (b) Circular V-notch crack on the implanted fiber surface; (c) Theoretical calculation of bend strength changes with crack length.



(Figure 5.2 continue)

considered. The stress intensity factor, K_I , in the front of a crack of a length c , can be written as [Tada, 1973]:

$$K_I = \frac{PL}{\pi b^3} \sqrt{\pi c} F(b, c) \quad (5.7)$$

where P is the applied load, L is the fiber length between load points, and $F(b, c)$ is a geometrical factor, which can be described as:

$$F(b, c) = \frac{3}{8} \left(\frac{b}{b-c} \right)^{\frac{5}{2}} \left\{ 1 + \frac{1}{2} \frac{b-c}{b} + \frac{3}{8} \left(\frac{b-c}{b} \right)^2 + \frac{5}{16} \left(\frac{b-c}{b} \right)^3 + \frac{35}{128} \left(\frac{b-c}{b} \right)^4 + 0.537 \left(\frac{b-c}{b} \right)^5 \right\} \quad (5.8)$$

i.e.,

$$K_I = \frac{3}{8} \sigma_0 \sqrt{\pi c} \left(\frac{b}{b-c} \right)^{\frac{5}{2}} \left\{ 1 + \frac{1}{2} \frac{b-c}{b} + \frac{3}{8} \left(\frac{b-c}{b} \right)^2 + \frac{5}{16} \left(\frac{b-c}{b} \right)^3 + \frac{35}{128} \left(\frac{b-c}{b} \right)^4 + 0.537 \left(\frac{b-c}{b} \right)^5 \right\} \quad (5.9)$$

where σ_0 is the bend strength. Note that in the present case, since $c \ll b$, equation (5.9) can be reduced to

$$K_I \cong 1.1242 \sigma_0 \sqrt{\pi c} \quad (5.10)$$

When K_I reaches the critical stress intensity factor K_{Ic} ($K_{Ic} = 2.5 \text{ MPa} \sqrt{m}$ for single crystal Al_2O_3 [Tressler, 1990]), the fiber will fail instantaneously. Thus taking the bend strength $\sigma_0 = 9.3 \text{ GPa}$, the corresponding critical crack length by equation (5.10) is 18 nm. it should be pointed out that 18 nm crack length is difficult to detect with our available equipment. The relation between bend strength σ_0 and critical crack length c can be plotted as shown in Figure 5.2(c).

Ochiai and Osamura [1988] calculated the average crack length in terms of an energy release rate. According to them, the flaw size C_{max} can be calculated by:

$$\sigma_f = (1/1.12) [E_f G_c^* / (\pi C_{max})]^{1/2} \quad (5.11)$$

or

$$C_{max} = \frac{E_f G_c^*}{1.25 \pi \sigma_f^2} \quad (5.12)$$

where σ_f is strength, E_f is Young's modulus of the fiber, G_c^* is critical elastic strain energy release rate of the fiber, given by $G_c^* = K_c^2 / E_f$ (K_c is the critical stress intensity factor for mode I). Taking $\sigma_f = 9.3$ GPa for unabraded fiber, $E_f = 414$ GPa, $K_c = 2.5$ MPa \sqrt{m} , the corresponding flaw size is again 18 nm. The calculation results are consistent for both approaches.

This analysis basically states that the maximum crack length in sapphire fiber is 18 nm to be consistent with the observed 9.3 GPa bend strength in three point bend loading.

Three point bend strength of implanted fibers

Before discussing the bend strength of implanted fibers, it is necessary to consider sputtering effects, since the relevant surface crack length is only 18 nm long. To assess the effects of sputtering on the surface removal of sapphire fiber, TRIM codes were used to theoretically calculate the sputter yield for the given ion implantation conditions. Displacement energies for Al_2O_3 were used (18 eV for Al and 72 eV for O). During the simulation, a total of 10,000 ions were counted. The calculated sputter yield was 0.1429 atoms/ion for Al and 0.2333 atoms/ion for O. Therefore, about 7 nm of the surface was removed during the implantation process, for an implantation dose of 5×10^{16} ion/cm² (assuming implantation was carried out on a planar substrate, and the density of Al_2O_3 is 3.97 g/cm³).

Since the measured bend strength of implanted fibers in the current work showed slight change compared with unimplanted fibers, and since compressive stress of 2 GPa was measured in implanted fibers, two questions arise: First, considering the 7 nm surface removal by sputtering, the length of pre-existing flaws may have been reduced to as little as 11 nm, consequently, by equation (5.10), the bend strength should be increased to 11.96 GPa. However, the highest bend strength was found to be only 9.5 GPa at the dose of $4 \times 10^{16} \text{ Mg}^+ \text{ cm}^{-2}$. At some doses, bend strength actually showed slight decrease¹. Thus, the first question is: why is there no increase in bend strength even if surface crack length becomes shorter? Secondly, if the presumed 2 GPa compressive stress is superimposed on the bending stress, the bend strength of implanted fibers should increase to a value of 11.3 GPa even in the absence of sputter losses. Why does the compressive stress not contribute to bend strength? Both of the questions are more easily approached by consideration of details of the sub-surface stress distribution in irradiated sapphire fibers.

The penetration depth in compressive stress measurement by indentation technique is about 2 μm , which actually penetrate through the implanted zone. The compressive stress is treated as if it were distributed over an equivalent depth. Such consideration does not represent the actual induced stress distribution. In Chapter 2, it has been stated that during the implantation process, high energy transfer collisions knock host atoms deep into the host, leaving a shallow vacancy region. Most implanted ions come to rest in projectile range region which is deeper inside the host. The host volume expands in the project range since the introduction of mass of foreign atoms, but it is constrained by the underlying substrate. Therefore, the stress state in the shallow vacancy region is different from the projectile range, and may in fact be tensile [Specht, 1994].

In Figure 4.34, TEM observations on implanted fibers revealed that there are four different regions in implanted zone, i.e., the free surface, the very-near-surface zone (VNS) between free surface and the buried layer or 'sub-near-surface' zone, the sub-near-

¹ For example, the bend strength was 8.87 GPa at dose of $2 \times 10^{16} \text{ Mg}^+ \text{ cm}^{-2}$, 8.91 GPa at dose of $7 \times 10^{16} \text{ Mg}^+ \text{ cm}^{-2}$, and 8.21 GPa at dose of $2 \times 10^{17} \text{ Mg}^+ \text{ cm}^{-2}$.

surface zone (SNS), and the unaffected interior of the fiber. The depth of VNS is about 40 nm deep (after a 7 nm sputter loss), and the SNS is about 200 to 400 nm deep for the implantation conditions examined. A schematic diagram in Figure 5.3 was constructed to demonstrate the relationships between relevant regions and surface stress distribution. Results from TRIM calculations are also included in the figure for implantation projectile range reference.

The compressive stress in sub-near-surface zone (SNS) should be balanced by VNS zone and fiber interior. Therefore, VNS zone and fiber interior are both in a tensile state. It is reasonable to assume the resulting tensile stress is uniformly distributed in these two regions. Since sapphire is an ionic crystalline it is difficult to cause lattice distortion on the neighbor atoms, and since the indentation penetration is 2 μm , it is reasonable to assume that the compressive stress is balanced over the indentation penetration region. The magnitude of tensile stress in very-near-surface region at each implantation dose and consequently the measured bend strength, measured compressive stress, sputtering yield, theoretical bend strength calculation are listed together in Table 5.1.

Table 5.1 Comparison of Magnitude of Tensile Stress in Very-Near-Surface (VNS), Measured Bend Strength, Measured Compressive Stress at Each Implantation Dose.

Dose (ions/cm ²)	Sputtered Thickness (nm) (Note 1)	Estimated Crack Length (nm)	Predicted Bend Strength (GPa) (Note 2)	Estimated Compressive Stress (GPa)	Measured Bend Strength (GPa)	Estimated Tensile Stress (GPa) (Note 3)	Estimated Bend Strength (GPa) (Note 4)
0	0	18	9.31	0	9.31	0	9.31
1x10 ¹⁶ Ar ⁺	1.4	16.6	9.7	1.8	9.15	0.036	9.66
2x10 ¹⁶ Mg ⁺	2.8	15.2	10.17	2	8.87	0.04	10.13
5x10 ¹⁶ Mg ⁺	7.0	11	11.96	2.2	9.26	0.044	11.91
2x10 ¹⁷ Mg ⁺	28	0	23 (Note 5)	2.6	8.21	0.052	22.95

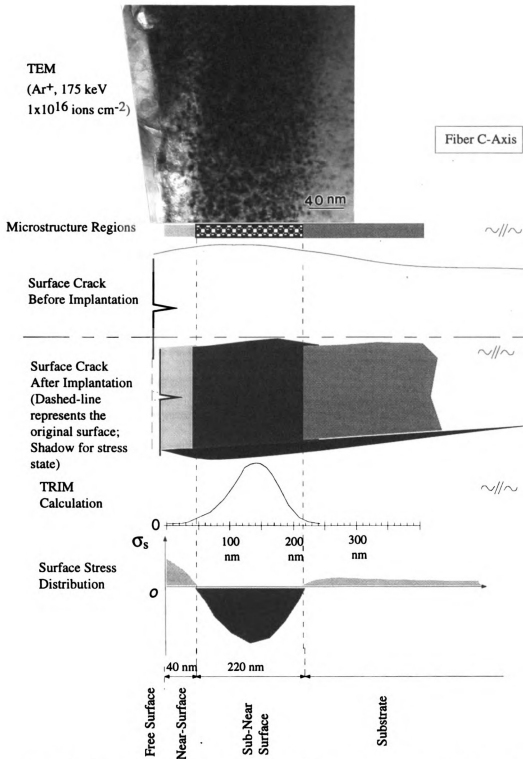


Figure 5.3 Schematic of implanted zone, surface crack geometry before and after ion implantation, and surface stress distribution. There four region in an implanted zone: free surface, near-surface (40 nm), buried layer (220 nm, depending on ion implantation conditions), and substrate.

- Note: 1. Sputtered thickness is based on TRIM sputter yield calculation, i.e., sputtered thickness is proportional to ion dose.
 2. Predicted bend strength is calculated by equation (5.10).
 3. Estimated tensile stress is calculated based on the thickness of VNS and undamaged fiber interior.
 4. Estimated bend strength is the difference between the predicted bend strength and estimated tensile stress.
 5. Theoretical strength ($G / 2\pi$), $G = 144$ GPa.

Comparison from this table, it can be seen that ion implantation has two effects on the bend strength, i.e., tensile stress in near-surface causes strength to decrease, and the compressive stress enhances the bend strength. The effects of compressive stress on the bend strength are discussed as follows.

Assume a same circular V-notch surface flaw pre-existing on the sapphire fiber. The compressive stress region induced by ion implantation is depicted as shadow area underneath the fiber surface, as shown in Figure 5.2(b).

Consider a crack retarded by the compressive stress region. The additional stress intensity factor K_a generated by the compressive stress in the front of a crack can be calculated by following relationships according to Lawn and Fuller [1984]:

$$K_a = 2\psi\sigma_s d^{1/2} \quad (5.13)$$

where d is the thickness of the implanted region, ψ is a crack geometry term ($4/\pi^2$), and σ_s is the surface stress. Taking $d = 0.4 \mu\text{m}$ (taken from the TEM observation), the additional stress intensity factor from the compressive region is:

$$K_a = -1.03 \text{ MPa}\sqrt{m} \quad (5.14)$$

Therefore, the new fracture criteria is:

$$\begin{aligned} K_{IC}' &= K_{IC} - K_a \\ &= 2.5 + 1.03 \end{aligned}$$

$$= 3.53 \text{ MPa} \sqrt{m} \quad (5.15)$$

In other words, if the stress intensity factor in front of a crack, K_I , is greater than K_{IC}' , fracture occurs; otherwise, the crack is arrested in the implanted zone.

Now, to resume the argument on the bend strength of implanted fibers. It was shown that the maximum crack length is 18 nm, which has been reduced to 11 nm considering sputtering effects for a dose of 5×10^{16} , to maintain 9.3 GPa bend strength. During three point bend test, the pre-existing crack with a presumed length of 11 nm propagates from initial position under constant loading as an external bending moment is applied to the fiber. The tensile stress in the VNS -Zone (0.044 GPa) may cause the onset of crack propagation at a low stress. But when the crack reaches the compressive SNS-Zone at a depth of 40 nm, the stress intensity factor K_I may be greater than K_{IC}' , the crack will not be arrested. This is because the crack is now 40 nm long. Specifically, at this point, the stress intensity factor can be calculated using equation (5.10) by taking $c = 40$ nm, and $\sigma_0 = 9.3$ GPa, one can obtain:

$$K_I = 3.71 \text{ MPa} \sqrt{m} \quad (5.16)$$

Comparing K_I and K_{IC}' , it turns out that:

$$K_I > K_{IC}', \quad (5.17)$$

Thus, the propagating crack continuously propagates through the implanted region, despite the existence of the compressive stress zone.

Based on the above analysis, it is important to realize that in the current three point bend test of 140 μm fiber, the pre-existing crack length is very small (about 11 nm) to

maintain the measured bend strength (9.3 GPa). With increase in pre-existing crack length, the bend strength decreases rapidly. Thus, even though there is a compressive stress region which is beyond the scale of the pre-existing crack, once the crack fails spontaneously upon application of external load, it becomes unstable. The existence of the compressive stress region couldn't retard the crack propagation, even though the magnitude of the compressive stress is very large. Unfortunately, the compression stress induced by ion implantation in our work is only about 2 GPa. This, therefore, is why there was no significant change in the bend strength of implanted fibers when compared with that of the unimplanted ones.

Now, to resume discussions on the sputtering effects on fiber surface morphology. Kawalski [1982, 1986, 1987, 1990] has developed a theoretical model to predict the surface morphology during ion bombardment. In the model, changes in the real surface profile caused by ion erosion depend on the angle of ion-beam incidence and the angle between beam direction and normal of the surface. Experimental results on 99.5% Al_2O_3 show that with a large ion incidence angle the Al_2O_3 surface becomes smooth or decreases in roughness, while the mean roughness of an ion-sputtered surface at a right angle is much greater than the unsputtered one. In our implantation process, the sample rotates around the central axis of a fixture. The angle of beam incidence with the normal of the surface changes with time. Thus there is not a clear relationship between ion sputtering and surface roughness for the present experiments. AFM (Atomic Force Microscopy) was used to obtain the sapphire fiber topography after implantation, as shown in Figure 5.4. The mean roughness difference between sputtered fiber and unsputtered fiber is less than 3 nm. Furthermore, whether the roughened surface consists of sharp surface flaws is doubtful. This result implies that the effect of ion sputtering on the fiber surface morphology is minor at this stage.

In summary, the tensile stress in near-surface region causes bend strength degradation slightly, compensating for crack shortening by sputter loss. The existence of a

buried compressive stress zone establishes a new fracture criterion of $3.53 \text{ MPa}\sqrt{m}$. When a pre-existing surface crack (with length 11 nm) propagates to the implanted zone (40 nm beneath the free surface), the corresponding stress intensity factor is $3.71 \text{ MPa}\sqrt{m}$, which is greater than the new fracture criterion. The implanted zone cannot arrest crack propagation in three-point bend loading. Therefore, no significant increase in bend strength was observed in current work.

5.3 *Residual Surface Stress and Abrasion Behavior*

In section 4.2, it has been well documented that abrasion leads to a significant strength degradation for unimplanted fibers, whereas the strength retention for implanted fibers is considerably higher after abrasion. This is intuitively puzzling in view of the failure of ion implantation to modify bend strength directly. It is reasonable to assume that abrasion causes surface damage to a certain extent. In the abrasion process, sapphire fibers are forced into contact with hard, sharp and irregularly shaped particles. Some of them may be considerably larger than the average particle size. Figure 5.5 illustrates the SEM observation on the contact interface between fiber and abrasive particles. The surface roughness profile is shown by AFM image section analysis in Figure 5.6. The average particle size is 5 μm in diameter. Figure 5.6 (c) schematically illustrate the contact position between sapphire fiber and SiC particle during abrasion process. Therefore, the abrasion process used in this study may be compared directly to the micro-indentation process where sharp contact takes place on the sample surface.

Figure 5.7 depicts one complete loading and unloading cycle during indentation [Lawn, 1975]:

(a) *Initial loading* The sharp indenter induces a zone of irreversible deformation about the contact point. The size of this zone increases with load;

(b) *Critical zone formation* At some critical indenter load, a crack suddenly initiates below the contact point, where the stress concentration is greatest;

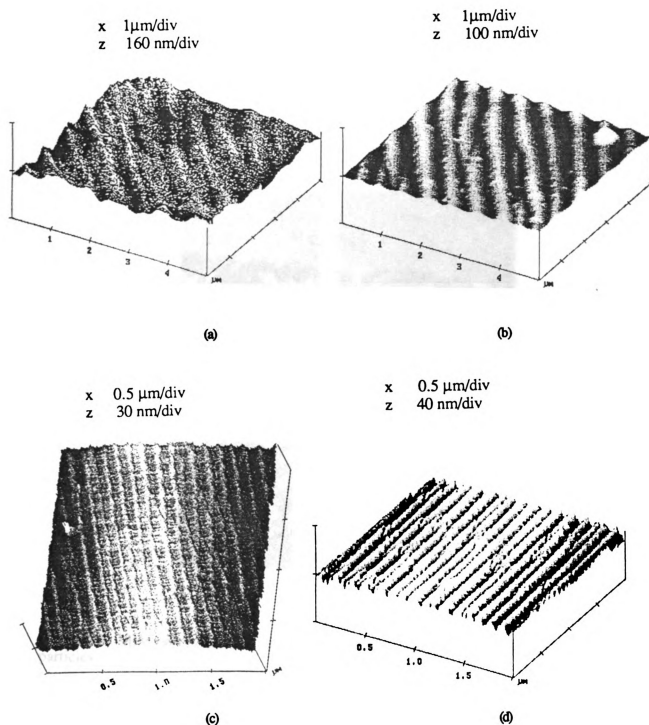


Figure 5.4 AFM topography on sapphire fiber surface (a) control fiber without abrasion; (b) control fiber with abrasion; (c) implanted fiber ($5 \times 10^{16} \text{Mg}^+ \text{cm}^{-2}$) without abrasion; (d) implanted fiber ($5 \times 10^{16} \text{Mg}^+ \text{cm}^{-2}$) with abrasion.

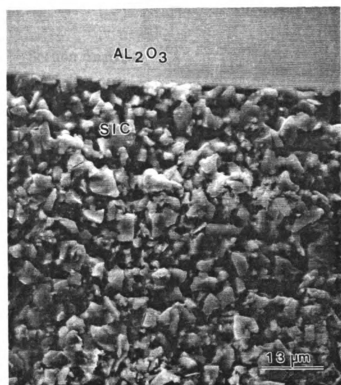


Figure 5.5 SEM observation on the interface between sapphire fiber and abrasive particles.

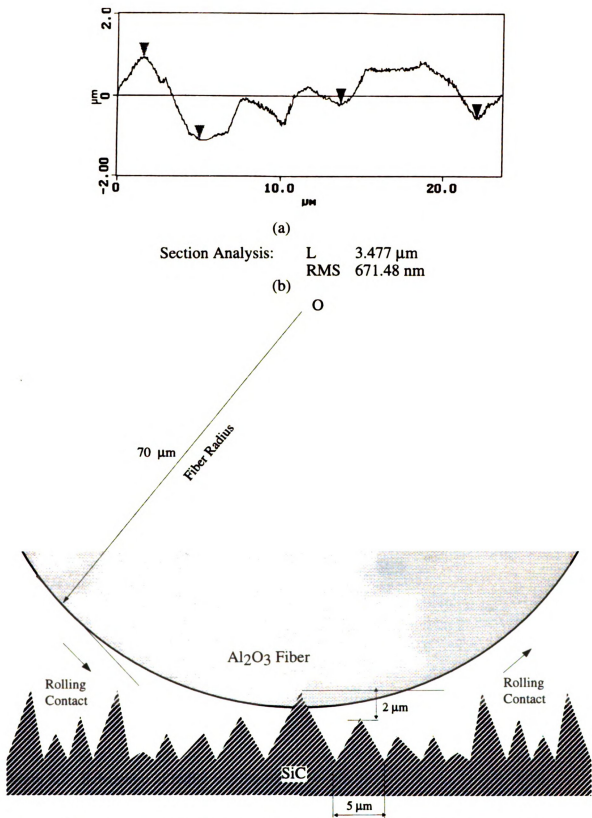


Figure 5.6 AFM section analysis on SiC abrasive paper surface profile. (a) Surface profile. Two pairs of arrows indicate the section position; (b) surface roughness calculation analysis; (c) Schematic of sharp point contact between a fiber and the abrasive paper.

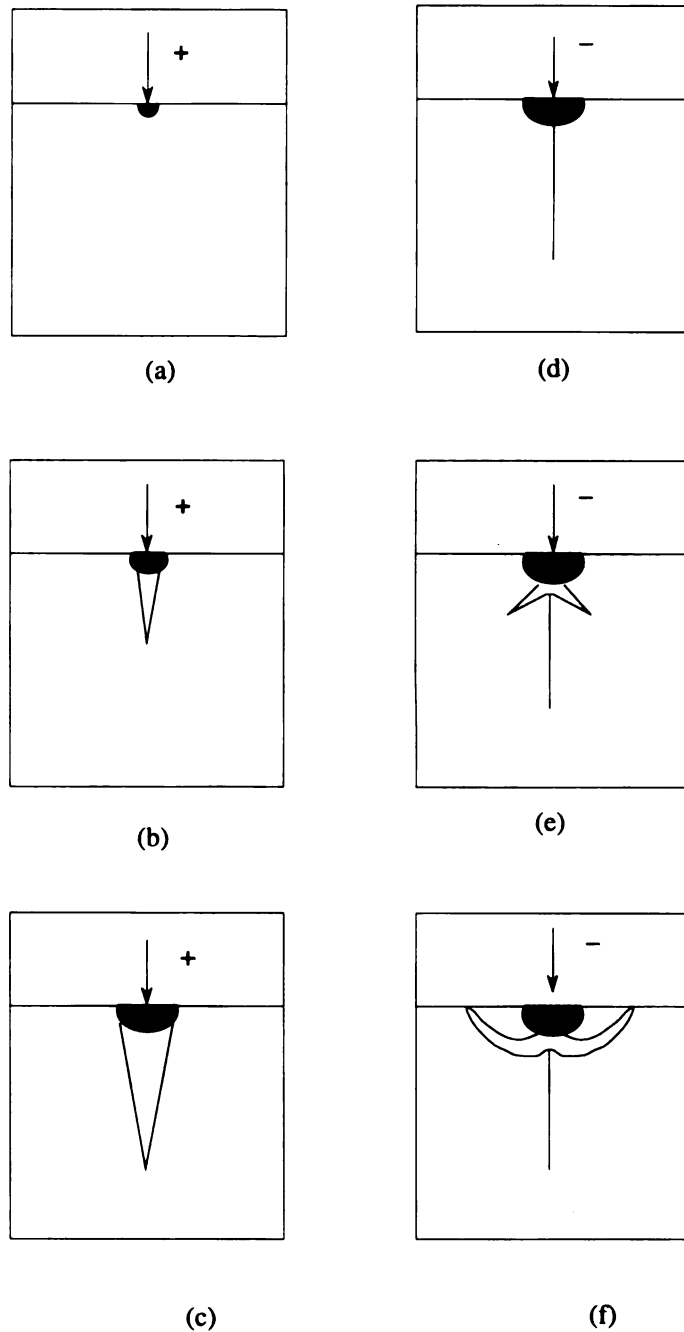


Figure 5.7 Schematic of radial and lateral cracks evolution under point indentation. Radial crack forms during loading (+) half cycle, lateral crack during unloading (-) half cycle. Fracture initiates from deformation zone (dark region). (a) initial loading, (b) critical zone formation, (c) stable crack growth, (d) initial unloading, (e) residual stress cracking, (f) complete unloading. (after B. R. Lawn and M. V. Swain, *J. Mater. Sci.*, **10**, 1975).

- (c) *Stable crack growth* Increasing the load causes further, stable extension of the median crack;
- (d) *Initial unloading* The median crack begins to close (not heal);
- (e) *Residual stress cracking* Relaxation of deformed material within the contact zone just prior to removal of the indenter superimposes intense residual tensile stress upon the applied load; and
- (f) *Complete unloading* The lateral crack continues to extend and may cause chipping.

The stress distribution beneath the point-load indentation is known as Boussinesq problem as depicted in Figure 5.8. Timoshenko [1951] has given the elastic solutions to the problem in polar coordinating system as follows:

$$\begin{aligned}
 \sigma_{rr} &= \frac{P}{2\pi} \left\{ (1-2\nu) \left[\frac{1}{r^2} - \frac{z}{r^2} (r^2 + z^2)^{-1/2} \right] - 3r^2 z (r^2 + z^2)^{-5/2} \right\} \\
 \sigma_{\theta\theta} &= \frac{P}{2\pi} (1-2\nu) \left\{ -\frac{1}{r^2} + \frac{z}{r^2} (r^2 + z^2)^{-1/2} + z (r^2 + z^2)^{-3/2} \right\} \\
 \sigma_{zz} &= -\frac{3P}{2\pi} z^3 (r^2 + z^2)^{-5/2} \\
 \sigma_{rz} &= -\frac{3P}{2\pi} r z^2 (r^2 + z^2)^{-5/2} \\
 \sigma_{r\theta} &= \sigma_{\theta z} = 0
 \end{aligned} \tag{5.18}$$

The principal normal stresses can be transformed by following relationship:

$$\begin{aligned}
\tan 2\alpha &= 2\sigma_r / (\sigma_z - \sigma_r) \\
\sigma_{11} &= \sigma_r \sin^2 \alpha + \sigma_z \cos^2 \alpha - 2\sigma_r \sin \alpha \cos \alpha \\
\sigma_{22} &= \sigma_{\theta\theta} \\
\sigma_{33} &= \sigma_r \cos^2 \alpha + \sigma_z \sin^2 \alpha + 2\sigma_r \sin \alpha \cos \alpha
\end{aligned} \tag{5.19}$$

The stress contours at the head of the indenter tip can be plotted by using Mathematica, as shown in Figure 5.9. Both σ_{11} and σ_{33} are contained within planes of symmetry through the normal load axis, with σ_{11} everywhere tensile, σ_{33} everywhere compressive. σ_{22} is perpendicular to the plane which contains load axis and σ_{11} and is tensile with a conical $\phi < 51.8^\circ$ below the indenter and compressive outside this region. In these stress contours, point load, P , is 30 mg. The stress values are labeled on each contour.

If there is a 2 GPa compressive stress zone in the front of the indentation tip, the resulting stress contours are changed. Generally, original tensile portions contract into a lower stress value, while compressive contours expand to a high compressive stress value. This is important because existence of compressive stress substantially affects indentation crack evolution as discussed as follows.

In order to better understand compressive stress effects and indentation crack evolution, a schematic is constructed in Figure 5.10 to show the stress distribution in implanted fibers, along with TEM microstructure observation and indentation stress contours which was imposed by the 2 GPa compressive stress. From Figure 5.10 (c), it can be seen that the stress changes from tensile to compressive. It is the compressive stress state that inhibits the median crack evolution. Since the tensile stress in the near-surface is small compared with the tensile stress σ_{11} caused by indentation, it thus is negligible.

During the indentation process, a penny-like median crack is formed upon the

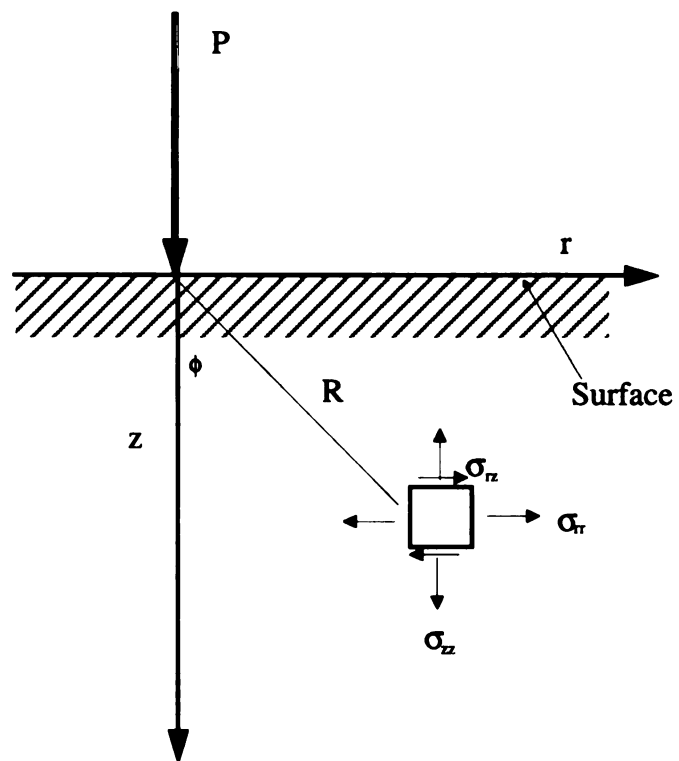


Figure 5.8 Polar coordinate system for Boussinesq axially symmetric point load P . $\sigma_{\theta\theta}$ is perpendicular to the plane.

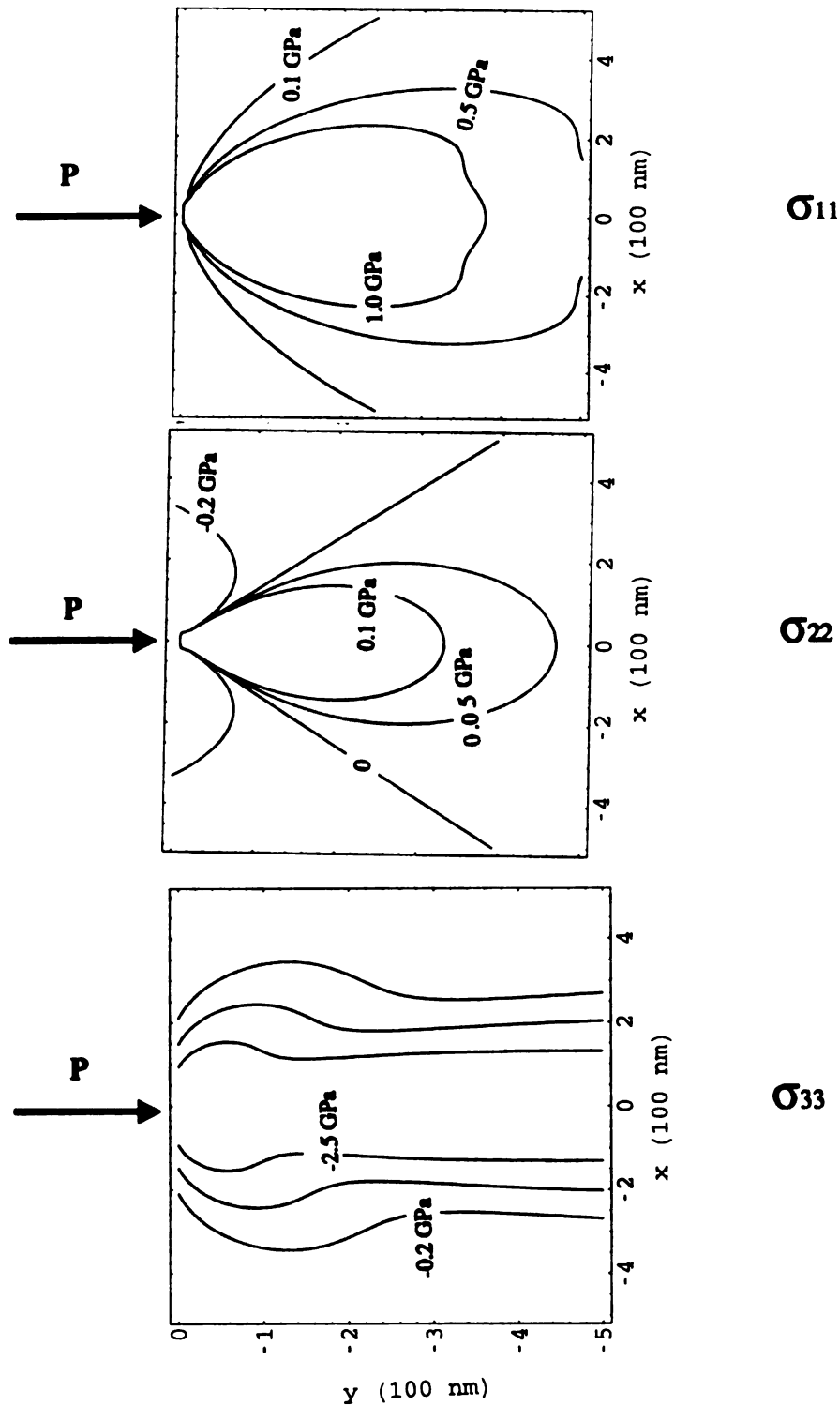


Figure 5.9 The stress contours in the front of point load indentation during sharp point contact. σ_{11} and σ_{33} are contained within planes of symmetry through the normal load axis, with σ_{11} everywhere tensile, σ_{33} compressive. σ_{22} is perpendicular to the plane containing load axis and σ_{11} and is tensile with $\phi < 51.8^\circ$ below the indenter and compressive outside this region.

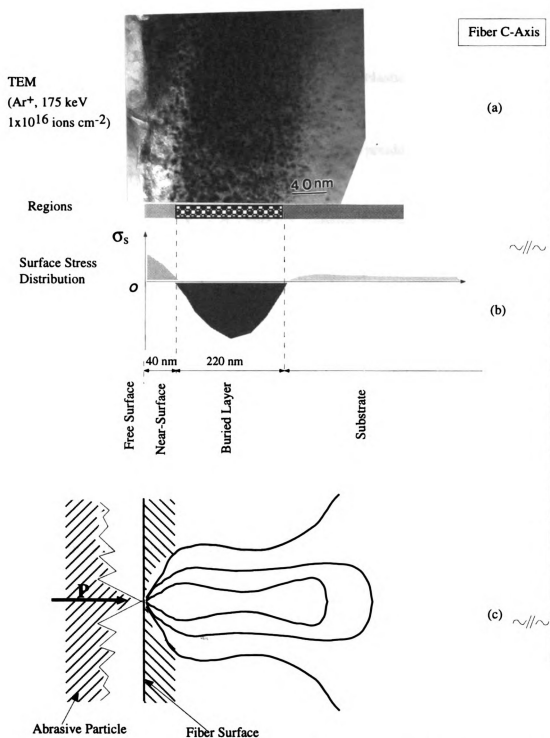


Figure 5.10 Schematic of the surface stress distribution in the implanted zone, and stress contour beneath sharp point contact during implanted fiber abrasion process. (a) TEM observation on 175 keV, 1×10^{16} Ar⁺cm⁻²; (b) Distribution of compressive stress induced by implantation; (c) Stress contour on the fiber surface produced by an abrasive particle (after superimposed by compressive stress).

application of point load P . Figure 5.11 shows median crack formation during an indentation process. According to Marshall [1979], the corresponding stress intensity factors are:

$$K_e = \frac{\chi_e P}{c^{3/2}} \quad (\text{arising from elastic driving force}) \quad (5.20)$$

$$K_r = \frac{\chi_r P}{c^{3/2}} \quad (\text{arising from residual stress}) \quad (5.21)$$

$$K_s = \sigma_s (\pi \psi c)^{1/2} \quad (\text{arising from surface stress}) \quad (5.22)$$

where χ_e , χ_r , ψ are dimensionless constants related to crack geometry, and $\psi = 4/\pi^2$, $\chi_r + \chi_e = 0.0139E/H$, $\chi_e > 3\chi_r$, E is Young's modulus, H is the hardness, $E = 414$ GPa, and $H = 20$ GPa for sapphire [Hioki: 1986]; P is the point load (30 mg), c is the median crack length and σ_s is the surface stress (2 GPa).

By the principle of superposition, the stress intensity factor is the summation of the three components, i.e.,

$$K_e + K_r + K_s = K_c \quad (5.23)$$

Considering the loading and unloading relation separately gives:

$$\frac{\chi_e P}{c^{3/2}} + \frac{\chi_r P}{c^{3/2}} + \sigma_s (\pi \psi c)^{1/2} = K_c \quad P \uparrow \quad (5.24)$$

$$\frac{\chi_e P}{c^{3/2}} + \frac{\chi_r P^*}{c^{3/2}} + \sigma_s (\pi \psi c)^{1/2} = K_c \quad P \downarrow \quad (5.25)$$

where P^* is the maximum load, $P \uparrow$ and $P \downarrow$ stand for loading and unloading cycles, respectively. When the unloading half cycle begins, the effective load in residual stress

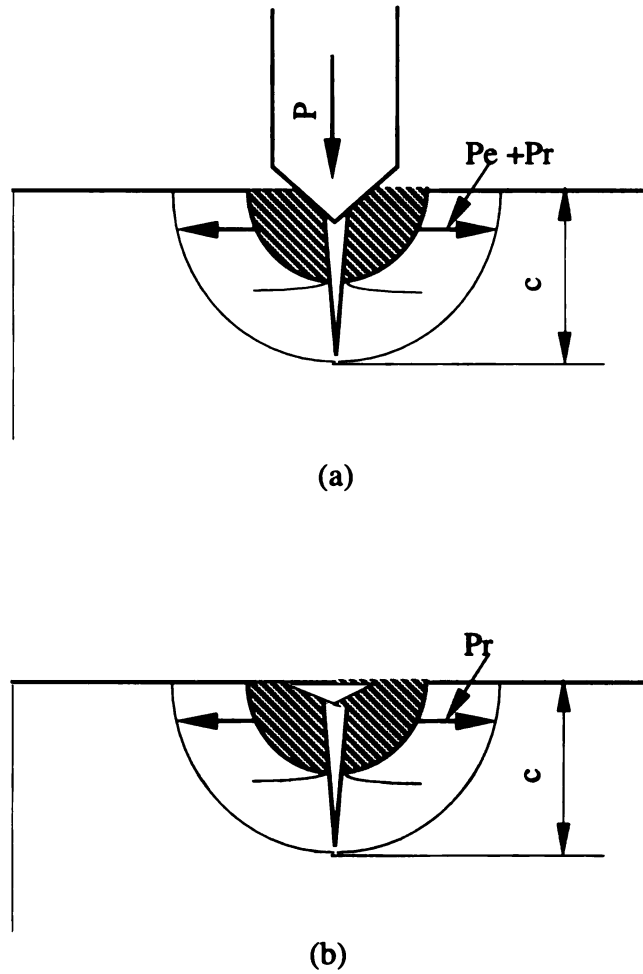


Figure 5.11 Stress distribution during indentation process. P is an applied external load, P_e is the elastic component of the field, and P_r is the residual stress. (a) during loading; (b) unloading.

zone reaches a maximum. Therefore, P^* was substituted for P in the second term of equation (5.25). The process of median crack evolution can be described as follows: the median crack reaches its maximum length, C^* , at the end of the loading half cycle, and then begins to contract when the unloading half cycle begins, and finally reaching an equilibrium length, C^v , when the point load P has been completely withdrawn. Thus, the median crack contraction arises from elastic recovery.

For unimplanted fibers (stress-free surface), taking $\sigma_s = 0$, during the loading cycle, $\Delta P > 0$, and $\Delta c > 0$, the maximum crack length, C^* , at maximum loading $P = P^*$ is:

$$C^* = [(\chi_e + \chi_r)P^*/K_c]^{2/3} \quad (5.26)$$

Substitute $\chi_e = 0.23$, $\chi_r = 0.057$, $P^* = 30$ mg, and $K_c = 2.5 \text{ MPa}\sqrt{m}$ into equation (5.26), one obtains:

$$C^* = 106 \text{ nm}$$

Similarly, during the unloading process, the residual portion $\frac{\chi_r P^*}{c^{3/2}}$ becomes constant, and differentiating equation (5.25) relative to c by taking $\sigma_s = 0$, the final equilibrium crack length is:

$$C^v = [\chi_e P^*/K_c]^{2/3} \quad (5.27)$$

Substitute $\chi_e = 0.23$, $P^* = 30$ mg, and $K_c = 2.5 \text{ MPa}\sqrt{m}$ into equation (5.27), one obtains:

$$C^v = 91 \text{ nm.}$$

By equation (5.10), the bend strength corresponding to this crack length is:

$$\sigma_0 = 4.15 \text{ GPa}$$

This calculated bend strength is close to measured bend strength for abraded unimplanted sapphire fibers.

Likewise, for implanted sapphire fibers (stressed surface), the maximum crack length during the loading cycle can be obtained by:

First, differentiating equation (5.24):

$$\frac{\partial c}{\partial P} = 2(\chi_e + \chi_r) / [3K_c^{1/2} + 4\sigma_s(\pi\psi)^{1/2}c] \quad (5.28)$$

Then integrating in the interval of load $[0, P^*]$:

$$\int_0^{P^*} (\chi_e + \chi_r) dP = \int_0^{C^*} \left(\frac{3}{2} K_c c^{0.5} - 2\sigma_s(\pi\psi)^{0.5} c \right) dc \quad (5.29)$$

Substituting $\chi_e = 0.23$, $\chi_r = 0.057$, $P^* = 30 \text{ mg}$, $\sigma_s = -2 \text{ GPa}$ and $K_c = 2.5 \text{ MPa}\sqrt{m}$ into equation (5.29), the maximum crack length during loading is:

$$C^* = 90 \text{ nm.}$$

Similarly, in order to obtain the final equilibrium crack length, first differentiating equation (5.25), and then integrating at the interval $[P^*, 0]$, gives:

$$\int_{P^*}^0 \chi_e dP = \int_{C^*}^0 \left(\frac{3}{2} K_c c^{0.5} - 2\sigma_s(\pi\psi)^{0.5} c \right) dc \quad (5.30)$$

The final crack length is

$$C^{\vee} = 32 \text{ nm.}$$

By equation (5.10), the bend strength is:

$$\sigma_0 = 7.01 \text{ GPa}$$

This calculated strength is also reasonably close to the measured bend strength for implanted fibers after abrasion.

The indentation fracture mechanics analysis on median crack evolution has good agreement with measured bend strength retention for abraded sapphire fibers. Without compressive stress, indentation can generate a median crack with a length three times as long as that with compressive stress. The existence of compressive stress can change stress distribution in the front of indenter tip, and effectively inhibit median crack growth. For the fiber abrasion process, this effect in turn allows retention of high bend strength for implanted fibers after abrasion.

In summary, for unimplanted fibers, abrasion produces deeper crack and thus causes fiber bend strength degradation. For implanted fibers, the irradiation-induced compressive stress of 2 GPa did not enhance fiber bend strength, even though a high fracture resistance is established in the implanted region. This is because the beginning of the compressive zone is buried deep enough not to affect pre-existing crack tips extension. By the time pre-existing cracks have grown into the compressive zone, their additional length brings the stress intensity level above the critical value even when the excess compressive stress is considered. In the case of implanted fibers subjected to the abrasion process, however, a compressive stress *can* effectively retard the median crack evolution, and thus retain a higher bend strength.

CHAPTER VI

SUMMARY OF RESULTS AND CONCLUSIONS

In the current work, effects of 175 keV Mg^+ and Ar^+ implantation into single crystal sapphire fibers were studied. TRIM calculations showed that the ion range of 175 keV Mg^+ implanted into sapphire is 190 nm with straggling 52 nm. The sputter yield during ion implantation is 0.14 atoms/ion for Al, and 0.23 atoms/ion for O; For 175 keV Ar^+ implantation, the ion range is 178 nm with straggling 42 nm.

TRIM calculations correlated with TEM observations if focusing and channeling effects are considered. TEM observations on implanted fibers with doses of $1 \times 10^{16} \text{ Ar}^+$, $7 \times 10^{16} \text{ Mg}^+$, and $2 \times 10^{17} \text{ Mg}^+/\text{cm}^2$ showed that there were four distinct regions in the implanted zone, i.e., free surface; a near-surface zone which was 40 ~ 50 nm underneath the free surface; a buried layer beginning at a depth of ~ 40 nm which was 200 nm to 400 nm thick and contained a high density of dark contrast features; and below this, the undamaged fiber interior. Diffraction patterns in these areas showed that the microstructures in these regions were crystalline after implantation.

By three-point bend tests, a characteristic bend strength of 9.31 GPa was measured for as-received fibers. Mg^+ and Ar^+ implantation into the fibers changed the characteristic bend strength only slightly. The Weibull distribution of the bend strength of all implanted fibers fall within the 95 percent confidence interval of the bend strength of unimplanted fibers.

The ability of ion implantation to enhance wear resistance was apparent. The bend strength of unimplanted fibers decreased about 49 percent after subjected to an abrasion process, whereas Mg^+ and Ar^+ implanted sapphire fibers retained up to 93 percent of their original strength. In terms of Weibull statistical analysis, abrasion caused significant

strength degradation on the unimplanted fibers but no significant degradation on implanted fibers.

The observed wear resistance enhancement was attributed to generation of a subsurface compressive stress region induced by ion implantation. By micro indentation technique, the magnitude of compressive stress was estimated to be about 2 GPa. The superficial fracture toughness was also found to increase monotonically with ion dose.

Based on these results, following conclusions are drawn:

1. The characteristic bend strength of Saphikon single crystal sapphire fiber is 9.31 ± 0.48 GPa.
2. 175 keV Mg^+ implantation into sapphire fibers has little effect on the bend strength for unabraded fibers. A slight enhancement in bend strength, to a maximum of 9.47 ± 0.33 GPa, resulted from a dose of 4×10^{16} ions cm^{-2} .
3. Similarly, 175 keV Ar^+ implantation also shows little effect on the bend strength for unabraded fibers. Measured bend strength varies from 8.34 ± 0.4 GPa to 9.24 ± 0.58 GPa.
4. Abrasion for 60 minutes causes 52 percent bend strength degradation in unimplanted fibers.
5. Mg^+ implantation substantially enhances the fiber abrasion resistance, resulting in over 90 percent of bend strength after abrasion.
6. Ar^+ implantation also allows over 90 percent of bend strength retention after abrasion.
7. The magnitude of the compressive stress induced by implantation is estimated to be at least 2 GPa, as measured by Vickers micro-indentation techniques.
8. The superficial fracture toughness of implanted fibers monotonically increases with ion dose.
9. Mg^+ implantation causes slight increase in nano-indentation hardness in intermediate implantation doses, and a decrease at the dose of 2×10^{17} Mg^+ cm^{-2} .

10. Residual bend strength of extracted unimplanted fibers from fiber-reinforced NiAl composite is sharply reduced, to 3.36 GPa. Residual bend strength of extracted Mg^+ implanted fibers is reduced to 4.51 GPa. Similarly, residual bend strength of extracted Ar^+ implanted fibers is reduced to 4.13 GPa.
11. Annealing fibers at 1400 °C for 2 hours produces 23 percent bend strength decrease for unimplanted fibers, and 21 to 28 percent for both Mg^+ and Ar^+ implantation.
12. TEM observations on implanted fibers show that there are four regions, i.e., the free surface, the near-surface region (40 nm) beneath free surface where there are few implanted ions, and the buried layer (200 nm to 400 nm width) where there is a high density of dark contrast features, and the un-damaged fiber interior.
13. Diffraction analysis in TEM observations shows that implanted region was still crystalline.
14. Fracture mechanics calculations show that a compressive stress establishes a higher fracture criterion of $3.53 \text{ MPa} \sqrt{m}$ in the implanted zone. However, since the zone is buried ~ 40 nm below the surface, the compressive zone can not arrest pre-existing crack propagation during three-point bend tests.
15. Indentation fracture mechanics calculations suggest that indentation events during abrasion produces deeper cracks in unimplanted fibers, whereas the compressive stress in implanted fibers can effectively resist crack extension during abrasion.

Results from the current work have shown that ion implantation is a useful technique to enhance surface abrasion resistance, and it indicates that ion implantation can be a powerful method to overcome the high surface sensitivities of sapphire fibers, which usually causes substantial strength degradation.

In order to continue the progress toward a better understanding of the efficiency of ion implantation in modification of surface properties, the following recommendations are made for future work:

1. Implantation of different ions such as Zr^+ , Cr^+ should be carried out to consider the chemical effects in irradiation damage.
2. High dose and low temperature implantation resulting in surface amorphization, which in turn affects surface properties.
3. TEM observation on characterization of defect clusters, possible diffusion and precipitate effects, and relationships between defect production and implantation conditions.

CHAPTER VII

BIBLIOGRAPHY

- Appleton, B.R., "Ion Beam and Laser Mixing Fundamental and Application," Ion Implantation and Beam Processing, ed. J. S. Williams and J.M. Poate, Academic Press, 1984.
- Asthana, R., Tewari, S. N., and Bowman, R. R., "Influence of Fabrication Technique on the Fiber Pushout Behavior in a Sapphire-Reinforced NiAl Matrix Composite," *Met. Mat. Trans. A* Vol. 26A, 209-223 (1995).
- ASTM Designation: E 382-89, "Standard Test Method for Microhardness of Materials," ASTM, 1989.
- Becher, P.F., "Abrasive Surface Deformation of Sapphire," *J. Amer. Ceram. Soc.*, Vol. 59, No. 3-4, 143-145 (1976).
- Becher, P.F., "Fracture-Strength Anisotropy of Sapphire," *J. Amer. Ceram. Soc.*, Vol. 59, No 1-2, 59-61 (1976).
- Bowman, R. R., Misra, A. K., and Arnold, S. M., "Processing and Mechanical Properties of Al₂O₃ Fiber-Reinforced NiAl Composites," *Met. Mat. Trans. A*, Vol. 26A, 615-628 (1995).
- Bowman, R. R., Misra, A. K., and Locci, I. E., "Unresolved Technical Barriers to The Development of A Structurally Viable Al₂O₃/NiAl Composite," *HITEMP Review 1992: Advanced High Temperature Engine Materials Technology Program*, NASA, HITEMP, 57-1 to 57-12 (1993).
- Brisset, F., and Vassel, A., "Compatibility of SiC and Al₂O₃ Continuous Fibers with Titanium Aluminum Matrices," Structural Intermetallics, edited by R. Doralia, J. J. Lewandowski, C. T. Liu, P. L. Martin, D. B. Miracle and M. V. Nathal, The minerals, Metals & Materials Society, 739-747 (1993).
- Bull, S.J., and Page, T.F., "Thermal Effects on the Microstructure and Mechanical Properties of Ion Implanted Ceramics," *J. Mater. Sci.*, Vol. 26, 3086-3106 (1991).
- Bull, S. J. and page, T. F., "The Effects of Ion Implantation on the Friction Behavior of Sapphire," *J. Mater. Sci.*, Vol. 30, 5356-70 (1995).
- Burnett, P. J., and Page, T. F. , "Changing the Surface Mechanical Properties of Silicon and α -Al₂O₃ by Ion Implantation," *J. Mater. Sci.*, Vol. 19 3524-45 (1984).
- Burnett, P. J., and Page, T. F. , "Changing The Surface Plasticity and Hardness of Sapphire by Ion Implantation," Deformation of Ceramic Materials, edited by R. E. Tressler and R. C. Bradt, 669-680 (1984).

- Burnett, P.J. and Page, T.F., "An Investigation of Ion Implantation-Induced near-Surface Stresses and Their Effects in Sapphire and Glass," *J. Mater. Sci.*, Vol. 20, 4624-4646 (1985).
- Burnett, P.J., and Page, T.F., "The Friction and Hardness of Ion-Implanted Sapphire," *Wear*, Vol.114, 85-96 (1987).
- Callister, W.D., "Materials Science and Engineering," Wiley, New York, 1985.
- Carter, G., and Colligon, J.S., Ion Bombardment of Solids, American Elsevier Publishing Company, Inc., New York (1968).
- Chason, E., Mayer, T.M. and Howard, A.J., "Kinetics of Surface Roughening and Smoothing During Ion Sputtering," Mechanism of Thin Film Evolution, eds. S. M. Yalisove, C.V.Thompson and D.J. Eaglesham, Materials Research Society, Pittsburgh, PA 1994.
- Darolia, R., "NiAl Alloys for High-Temperature Structural Applications," *JOM*, March, 44-49 (1991).
- Darolia, R., "NiAl for Turbine Airfoil Applications," Structural Intermetallics, edited by R. Darolia, J. J. Lewandowski, C. T. Liu, P. L. Martin, D. B. Miracle and M. V. Nathal, The minerals, Metals & Materials Society, 495-504 (1993).
- Davis, J. B., Yang, J., and Evans, A. G., "Effects of Composite Processing on the Strength of Sapphire Fiber-Reinforced Composites," *Acta Metall. Mater.*, Vol. 43, No. 1, 259 - 269 (1995).
- Dearnaley, G., Freeman, J.H., Nelson, R.S., and Stephan, J., "Ion Implantation," Defects in Crystalline Solids, eds. S. Amelinckx and R. Gevers, Vol. 8, North-Holland Publishing Company, 1973.
- Dienes, C.J, and Vineyard, G.H., Radiation Effects in Solids, Wiley, New York, 1957.
- Dörre, E., and Hübner, H. Alumina, Springer-Verlag Berlin, Herdelberg, 1984.
- Draper, S.L., Eldridge, J.I., and Locci, I.E., "Al₂O₃ Fiber Strength Degradation in MMC's and IMC's," *HITEMP Review 1992: Advanced High Temperature Engine Materials Technology Program*, NASA, HITEMP, 17-1 to 1713 (1992).
- Draper, S. L., and Locci, I. E., "Al₂O₃ Fiber Strength Degradation in Metal and Intermetallic Matrix Composites," *J. Mater. Res.*, Vol. 9, No. 6, 1397 - 1441 (1994).
- Duwell, E.J., "Friction and Wear of Single-Crystal Sapphire Sliding on Steel," *J. Appl. Phys.*, Vol.35, No.9, 2691-2697 (1962).
- Dutt, B. V., and Kroger, F. A., "High Temperature Defect Structure of Cobalt-doped α -Alumina," *J Amer. Ceram. Soc.*, Vol. 58, 420-427 (1975).
- EerNisse, E.P., "Sensitive Technique for Studying Ion-Implantation Damage," *Appl. Phys. Let.*, Vol. 18, 581-583 (1971).

- Green, D.J., "Compressive Surface Strengthening of Brittle Materials," J. Mater. Sci., Vol. 19, 2165-2171 (1984).
- Heuer, A. H., "Deformation Twinning in Corundum," Phil. Mag., Vol. 13, 379-393 (1966).
- Hioki, T., Itoh, A., Noda, S., Doi, H., Kawamoto, J., and Kamigaito, O., "Effect of Ion Implantation on Fracture Stress of Al_2O_3 ," Nucl. Inst. Meth. Phys. Res., B7/8, 521-525 (1985).
- Hioki, T., Itoh, A., Noda, S., Doi, H., Kawamoto, J., and Kamigaito, O., "Strengthening of Al_2O_3 by Ion Implantation," J. Mater. Sci. Lett., Vol. 3, 1099 - 1101 (1984).
- Hioki, T., Itoh, A., Noda, S., Doi, H., Kawamoto, J., and Kamigaito, O., "Modification of the Mechanical Properties of Ceramics by Ion Implantation," Nucl. Inst. Meth. Phys. Res., B39, 657-664 (1989).
- Hioki, T., Itoh, A., Ohkubo, M., Noda, S., Doi, H., Kawamoto, J., and Kamigaito, O., "Mechanical Property Changes in Sapphire by Nickel Ion Implantation and Their Dependence on Implantation Temperature," J. Mater. Sci., Vol. 21, 1321-1328 (1986).
- Hockey, B.J., "Plastic Deformation of Aluminum Oxide by Indentation and Abrasion," J. Amer. Ceram. Soc., Vol. 54, No. 5, 223-231 (1971).
- Holland, F.A., and Zaretaky, E.V., "Investigation of Weibull Statistics in Fracture Analysis of Cast Aluminum," NASA TM-102000, 1989.
- Jardine, A. P., Mukhopadhyay, S. M., and Blakely, J. M., "Mg Implantation and Characterization of Sapphire Surface," Mat. Res. Soc. Symp., Vol. 74, Materials Research Society, 365 - 373 (1987).
- Jaskowiak, M.H., and Setlock, J.A., "Mechanical Behavior of Sapphire Reinforced Alumina Matrix Composites," HITEMP Review 1993: Advanced High Temperature Engine Materials Technology Program, NASA, HITEMP, 70-1 to 70-11 (1993).
- Jaskowiak, M.H., Eldridge, J.I., Hurst, J.B., and Setlock, J.A., "Interfacial Coating for Sapphire/ Al_2O_3 ," HITEMP Review 1991: Advanced High Temperature Engine Materials Technology Program, NASA, HITEMP, 84-1 to 84-11 (1991).
- Jayne, D. T., and Matthiesen, M. M., "Removing Hydroxypropyl Methylcellulose Sizing from Sapphire Fibers by Ultraviolet/Ozone Cleaning," J. Am. Ceram. Soc., Vol. 78, 2861-64 (1995).
- Johnson, L. G., "The Median Ranks of Samples Values in Their Population with an Application to Certain Fatigue Studies," Indust. Math., 1951.
- Johnson, L.G., "The Statistical Treatment of Fatigue Experiments," Elsevier Publication Co., New York, 1964.

- Jones, L.E., Newcomb, S.A., and Tressler, R.E., "Creep and Rupture Behavior of Single Crystal Sapphire Filaments," HITEMP Review 1990: Advanced High Temperature Engine Materials Technology Program, NASA, HITEMP, 47-1 to 47-16 (1990).
- Kern, D.Q, "Process Heat Transfer," McGraw-Hill Book Company, Inc., 1950.
- Kinchin, G.H, and Pease, R.S., Rep. Progr. Phys., Vol. 18, 1 (1955).
- Kingery, W.D., Bowen, H. K., and Uhlmann, D. R., Introduction to Ceramics, 2nd ed., New York; John Wiley and Sons, 1976.
- Kirchner, H. P., Gruver, R. M. and Walker, R. E., "Strengthening Sapphire by Compressive Surface Layers," J. Appl. Phys., Vol. 40, NO. 9, 3445 - 3452 (1969).
- Kowalski, Z.W., "Ion-Bombardment Modification of the Surface Morphology of Solids," J. Mater. Sci., Vol. 25, 2875-2879 (1990)
- Krefft, G.B., and EerNisse, E.P., "Volume Expansion and Annealing Compaction of Ion-Bombarded Single-crystal and Polycrystalline α -Al₂O₃," J. Appl. Phys., Vol.45, No.5, 2725-2730 (1978).
- Kronberg, M.L., "Plastic Deformation of Single Crystals of Sapphire: Basal Slip and Twinning," Acta Metall., Vol.5, No.9, 507-524 (1957).
- Kumar, K. S., Mannan, S. K., and Viswanadham, R. K., "Fracture Toughness of NiAl and NiAl-Based Composites," Acta. Metall. Mater., Vol. 40, 1201-22 (1992).
- Lagerlöf, K.P.D., Mitchell, T.E, and Heuer, A.H., "Deformation and Diffusion in Sapphire (α -Al₂O₃)," Deformation of Ceramic Materials II, eds. R.E. Tressler and R.C. Bradt, Plenum Press, New York, 199-212 (1984).
- Lagerlöf, K.P.D., Pletka, B. J., Mitchell, T. E., and Heuer, A. H., "Deformation and Diffusion in Sapphire (α -Al₂O₃)," Radiation Effects, Vol. 74, 87 - 107 (1983).
- Lawn, B.R., and Fuller, E.R., "Measurement of Thin-Layer Surface Stress by Indentation Fracture," J. Mater. Sci., Vol.19, 4061-4067 (1984).
- Lawn, B.R., and Swain, M.V., "Microfracture Beneath Point Indentation in Brittle Solids," J. Mater. Sci., Vol.10, 113-123 (1975).
- Lawn, B.R., Evans, A.G., and Marshall, D.B., "Elastic/Plastic Indentation Damage in Ceramics: The Median/Radial Crack System," J. Amer. Ceram. Soc., Vol.63, No. 9-10, 574-581 (1980).
- MacKay, R. A., Brindley, P. K., and Froes, F. H., "Continuous Fiber-Reinforced Titanium Aluminide Composites," JOM, May, 23-29 (1991).
- Marshall, D.B., Lawn, B.R., and Evans, A.G., "Elastic/Plastic Indentation Damage in Ceramics: The Lateral Crack System," J. Amer. Ceram. Soc., Vol. 65, 561-566 (1982).

- Marshall, D. B., and Lawn, B. R., "Residual Stress Effects in Sharp Contact Cracking: Part 1 *Indentation Fracture Mechanics*," J. Mater. Sci., Vol. 14, 2001 - 2012 (1979).
- Marshall, D. B., and Lawn, B. R., "Residual Stress Effects in Sharp Contact Cracking: Part 2 *Strength Degradation*," J. Mater. Sci., Vol. 14, 2001-2012 (1979).
- Martz, S. W., and Tressler, R. E., "The Threshold Stress Intensity for Slow Crack Growth in C-Axis Sapphire Fibers," HITEMP Review 1992: Advanced High Temperature Engine Materials Technology Program, NASA, HITEMP, 81-1 to 81-11 (1992).
- McCallum, J. C., White, C. W., Sklad, P. S., and McHargue, C. J., "Annealing Environment effects in Solid-Phase Epitaxial Regrowth of Fe-Implantation Al_2O_3 ," Nucl. Inst. Meth. Phys. Res., B46, 137 - 143 (1990).
- McHargue, C. J., "The effects of Ion Implantation on the Structure of Ceramics," JOM No. 7, 40 - 44 (1991).
- McHargue, C. J., Farlow, G. C., Begun, G. M., Williams, J. M., White, C. W., Appleton, B. R., Sklad, P. S., and Angelini, P., "Damage Accumulation in Ceramics During Ion Implantation," Nucl. Inst. meth. Phys. Res., B16, 212 - 220 (1986).
- McHargue, C. J., Farlow, G. C., Lewis, M. B., and Williams, J. M., "Implantation of Gases into Sapphire," Nucl. Inst. Meth. Phys., B19/20, 809 - 812 (1987).
- McHargue, C. J., Farlow, G. C., Sklad, P. S., and White, C. W., "Iron Ion Implantation Effects in Sapphire," Nucl. Inst. Meth. Phys. Res., B19/20, 813 - 821 (1987).
- McHargue, C.J., Naramoto, H., Appleton, B.R., White, C.W., and Williams, J.M., "Structure and Properties of Single Crystal Al_2O_3 Implanted with Chromium and Zirconium," Metastable Materials Formation by Ion Implantation, eds. S.T. Picraux and W.J. Choyke, Elsevier Science Publishing Company, Inc., New York, 147-153 (1982).
- McHargue, C.J., Yust, C.S., Angelini, P., Sklad, P.S., and Lewis, M.B., Science of Hard Material II, eds. C. Brooks and F. Almond, Adam Hilger, Bristol, 803-812(1986).
- McHargue, C.J., and Yust, C.S., "Lattice Modification in Ion-Implanted Ceramics," J. Amer. Ceram. Soc., Vol. 67, No. 2, 117-123 (1984).
- Misra, A. K., Bowman, R.R., Locci, I.E., and Matthiesen, M. M., "Interface Mo Coatings For $\text{Al}_2\text{O}_3/\text{NiAl}$ Composite," HITEMP Review 1992: Advanced High Temperature Engine Materials Technology Program, NASA, HITEMP, 58-1 to 58-13, (1993).
- Morscher, G.N., Sayir, H., and Unal, O., "The Bend Properties of Sapphire Fibers at Room and High Temperatures," HITEMP Review 1992: Advanced High Temperature Engine Materials Technology Program, NASA, HITEMP, 18-1 to 18-14, (1992).

- Mukhopadhyay, S.M., Jardine, A.P., Blakely, J.M. and Baik, S., "Segregation of Magnesium and Calcium to the (1010) Prismatic Surface of Magnesium-Implanted Sapphire", *J Amer. Ceram.*, Vol. 71, 358-62 (1988).
- Naguib, H. M., and Kelly, R., *Radiation Effects*, Vol. 25, 1 (1975).
- Norgett, M. J., Robinson, M. T., and Torrens, I. M., "A Proposed Method of Calculating Displacement Dose Rates," *Nucl. Eng. Desi.*, Vol. 33, 50 - 54 (1975).
- Nutt, S.R., and Wawner, F.E., "Silicon Carbide Filaments: Microstructure," *J. Mater. Sci.*, Vol. 20, 1953-1960(1985).
- Ochiai, S., and Murakami, Y, "Theoretical Prediction of Tensile Strength of Fibers as a Function of Thickness of Brittle Zones on Fiber Surfaces," *Met. Trans. A*, Vol. 12A, No. 7, 1155 - 1161 (1981).
- Ochiai, S., and Osamura, K., "A Computer Simulation on Tensile Strength of Surface-Damages Fibers," *Met. Trans. A*, Vol. 19A, No.6, 1499 -1506 (1988).
- O'Hern, M.E., McHargue, C.J., White, C.W., and Farlow, G.C., "The Effect of Chromium Implantation on the Hardness, Elastic Modulus and Residual Stress of Al_2O_3 ," *Nucl. Inst. Meth. Phys. Res.*, B46, 171-175 (1990).
- O'Hern, M. E., Romana, L. J., McHargue, C. J., McCallum, J. C., and White, C. W., "The Effect of Crystl Orientation on Damage Accumulation in Chromium-Implanted Al_2O_3 ," *ASTM STP 1125*, 740 - 748 (1992).
- Ohkubo, M., Hioki, T., Suzuki, N., Ishiguro, T., and Kawamoto, J., "Structure and Magnetic Properties of Fe-Implanted Sapphire," *Nucl. Inst. Meth. Phys. Res.*, B39, 675 - 679 (1989).
- Ohkubo, M., Hioki, T., and Kawamoto, J., "Recrystalline-Driven Migration and Resultant-Oriented Precipitation", *J. Appl. Phys.*, Vol.60, No15, 1325-1335 (1986).
- Pedraza, D. F., and Mansur, L. K., "The Effect of Point Defects on the Amorphization of Metallic Alloys During Ion Implantation," *Nucl. Inst. Meth. Phys.*, B16, 203 - 211 (1986).
- Pollack, J. T., and Hurley, G. F., "Dependence of Room Temperature Fracture Strength on Strain-rate in Sapphire," *J. Mater. Sci.*, Vol. 18, 1595-1602 (1973).
- Ramos, S.M.M., Canut, B., Geam L., Thevenard, P., Bauer, M., Maheo, Y., Kapsa, Ph., and Loubet, J.L., "Structure, Mechanical and Tribological Properties of Titanium Implanted Alumina," *J. Mater. Res.*, Vol. 7, No. 1, 173-184 (1992).
- Sayir, H., DeGuire, M.R., Sayir, A., and Lagerlöf, K.P.D., "Bend Strength of Undoped and Impurity Doped Laser Heated Float Zone Sapphire Fibers," *HITEMP Review 1992: Advanced High Temperature Engine Materials Technology Program*, NASA, HITEMP, 20-1 to 20-17 (1992).
- Schalek, R., Ph.D. dissertation, Michigan State University, 1995.

- Shah, D. M., and Anton, D. L., "Alumina Fiber Reinforced Intermetallic Matrix Composites," Structural Intermetallics, edited by R. Doralia, J. J. Lewandowski, C. T. Liu, P. L. Martin, D. B. Miracle and M. V. Nathal, The Minerals, Metals & Materials Society, 755-764 (1993).
- Sorensen, J., "Continuous Fiber Reinforced Intermetallic Composites: An Overview," Structural Intermetallics, edited by R. Doralia, J. J. Lewandowski, C. T. Liu, P. L. Martin, D. B. Miracle and M. V. Nathal, The Minerals, Metals & Materials Society, 717-726 (1993).
- Specht, E. D., Walko, D. A., and Zinkle, S. J., "Amorphization of Al_2O_3 by Ion Induced Density Reduction," Nucl. Inst. Meth Phys. Res., B84, 323-330 (1994).
- Steijn, R.P., "On the Wear of Sapphire," J. Appl. Phys., Vol. 32, No. 10, 1951-1958 (1961).
- Stotel, F., and Conrad, H., "Fracture and Twinning in Sapphire (α - Al_2O_3 Crystals)," Trans. AIME, Vol. 227, 1053-1060 (1963).
- Stough, M.A., Hellmann, J.R., and Angelone, M.S., "Zirconia Coated Sapphire Fiber Surface Degradation," HITEMP Review 1993: Advanced High Temperature Engine Materials Technology Program, NASA, HITEMP, 80-1 to 80-10 (1993).
- Tada, H., Paris, P.C., and Irwin, G. R., The Stress Analysis of Cracks Handbook, Del Research Corporation, Hellertown, Pennsylvania, 1973.
- Tewari, S. N., Asthana, R., and Noebe, R. D., "Interfacial Shear Strength of Cast and Directionally Solidified NiAl-Sapphire Fiber Composites," Met. Trans. A, Vol. 24A, 2119-25 (1993).
- Tewari, S. N., Asthana, R., Tiwari, R., and Bowman, R. R., "Zone Directional Solidification of Sapphire NiAl Composite," HITEMP Review 1992: Advanced High Temperature Engine Materials Technology Program, NASA, HITEMP, 60-1 to 60-11 (1993).
- Tewari, S. N., Asthana, R., Tiwari, R., Bowman, R. R., and Smith, J., "Influence of Interfacial Reactions on the Fiber-Matrix Interfacial Shear Strength in Sapphire-Reinforced NiAl(Yb) Composites," Met. Mat. Trans. A, Vol. 26A, 477-491 (1995).
- Tewari, S. N., Asthana, R., Tiwari, R., Bowman, R. R., and Smith, J., "Influence of Interfacial Reactions on the Fiber-Matrix Interfacial Shear Strength in Sapphire Fiber-Reinforced NiAl(Yb) Composites," Met. Trans. A, Vol. 26A, 477-491 (1995).
- Timoshenko, S., and Goodie, J. N., Theory of Elasticity, McGraw-Hill Book Company, Inc., 1951.
- Traubauer, E.R., Hellman, I.R., Shelleman, D.C., and Koss, D.A., "Effect of Cleaning and Abrasion-induced Damage on the Weibull Strength Distribution of Sapphire Fiber," J. Am. Ceram. Soc., Vol. 77, 2017-2 (1994).

- Traubauer, E.R., Hellman, I.R., Shelleman, D.C., and Koss, D.A., "Effect of Fiber Surface Cleaning Procedures on Tensile Strength of Sapphire Fibers," HITEMP Review 1992: Advanced High Temperature Engine Materials Technology Program, NASA, HITEMP, 16-1 to 16-15 (1992).
- Tressler, R.E., and Newcomb, S.A., "Factors Influencing the High Temperature Strength of Sapphire Fibers," HITEMP Review 1992: Advanced High Temperature Engine Materials Technology Program, NASA, HITEMP, 19-1 to 19-16 (1992).
- Tressler, R.E., Langesiepen, R.A., and Bradt, R.C., "Surface-Finish Effects on Strength-vs-Grain-Size Relations in Polycrystalline Al_2O_3 ," J. Amer. Ceram. Soc., Vol. 57, 227-228 (1974).
- Tsuchimoto, T., and Tokuyama, T., Radiation Effects, Vol. 6, 121 (1970).
- Watchman Jr., J.B., Tefft, W.E., Lam Jr., D.G., "Elastic constants of synthetic single crystal corundum at room temperature," J. Res. Nat. Bur.Stds., Vol. 64A, 213-228 (1960).
- Wiederhorn, S. M., "Fracture of Sapphire," J. Amer. Ceram. Soc., Vol. 52, 485-491 (1969).
- Wiederhorn, S. M., Hockey, B. J., and Robert, D. E., "Effect of Temperature on the Fracture of Sapphire," Philog. Mag., Vol. 28, 783 - 796 (1978).
- Wiederhorn, S. M., "Brittle Fracture and Toughening Mechanisms in Ceramics," Ann. Rev. Mater. Sci., Vol. 14, 373 - 403 (1984).
- Yee, J., Kroger, F. A., "Measurements of Electromotive Force in Al_2O_3 - Pitfalls and Results," J. Amer. Ceram. Soc., Vol. 56, 189-191 (1973).
- Ziegler, J.F., Biersack, J.P., and Littmark, U., The Stopping and Range of Ions in Solids, Pergamon Press, New York (1985).